# LABORATORY MEASUREMENTS OF THE MILLIMETER WAVELENGTH OPACITY OF PHOSPHINE ($PH_3$) AND AMMONIA ($NH_3$) UNDER SIMULATED CONDITIONS FOR THE CASSINI-SATURN ENCOUNTER

A Dissertation
Presented to
The Academic Faculty

By

Priscilla N. Mohammed

In Partial Fulfillment
of the Requirements for the Degree of
Doctor of Philosophy in Electrical Engineering

Georgia Institute of Technology
April 2005

**LABORATORY MEASUREMENTS OF THE MILLIMETER WAVELENGTH OPACITY OF PHOSPHINE ($PH_3$) AND AMMONIA ($NH_3$) UNDER SIMULATED CONDITIONS FOR THE CASSINI-SATURN ENCOUNTER**

Approved by:

Dr. Paul G. Steffes, Advisor
School of Electrical & Computer Engineering
*Georgia Institute of Technology*

Dr. Andrew F. Peterson
School of Electrical & Computer Engineering
*Georgia Institute of Technology*

Dr. Waymond R. Scott
School of Electrical & Computer Engineering
*Georgia Institute of Technology*

Dr. Aaron D. Lanterman
School of Electrical & Computer Engineering
*Georgia Institute of Technology*

Dr. Judith A. Curry
School of Earth & Atmospheric Sciences
*Georgia Institute of Technology*

Date Approved: April 11, 2005

To Mom

## ACKNOWLEDGMENTS

I thank my advisor, Dr. Paul G. Steffes for his guidance and support throughout my time at Georgia Tech. His knowledge, enthusiasm and understanding have made this an invaluable experience professionally as well as personally. I also thank the committee members for their careful assessment of my thesis: Dr. A. F. Peterson and Dr. W. R. Scott.

I thank the following people for their contributions to this work: Dr. James P. Hoffman (JPL) for his informative discussions about laboratory measurements and formalism development, Dr. Jon M. Jenkins (SETI Institute) for his insight into the radio occultation of oblate planets, Dr. Dave R. DeBoer (SETI Institute) for use of his thermochemical model, Dr. Essam Marouf (San Jose State University & Cassini Radio Science team member) for access to the orbital information necessary to simulate the radio occultation experiment at Saturn, Dr. Daniel P. Campbell (GTRI) for his discussions about phosphine and ammonia adsorption and Dr. T. K. Gaylord (Georgia Tech) for multiple use of his helium-neon laser.

Without the encouragement of family and friends this process would not have been possible. I praise my parents, Ralph and Korisha Mohammed, whose sacrifices have allowed me to pursue and achieve my highest aspirations and also my elder brothers, Ronnie and Rafer, and sister-in-law, Lorraine, whose academic and professional successes have inspired my ambitions. My young nephews, Aiden and Jaron are joyous. My friends Swathi Nakkana and Denise Yiyi Chen have sustained my sanity and sensibility. I thank my fifth floor colleagues for their help and friendship: Sharon J. Fennell, Allen J. Petrin, Bryan M. Karpowicz, William C. Barrott and Thomas R. Hanley.

Finally, I thank Akio Tano for being loyal to me throughout graduate school, for still supporting me and enriching my life.

This work has been supported by the Planetary Atmospheres Program of the National Aeronautics and Space Administration under grant NAG 5-12122.

## CONTENTS

## LIST OF TABLES

## LIST OF FIGURES

## SUMMARY

The molecular compositions of the atmospheres of the giant[1] planets are fundamental to understanding the processes which formed these planets and the solar system as a whole. Microwave observations of these planets probe regions in their atmospheres from approximately 0.1 to several bars, a process otherwise unachievable by visible and infrared means. Many gases and various cloud layers influence the millimeter wave spectra of the outer planets; however phosphine and ammonia are the main microwave absorbers at Saturn at pressures less than two bars. Understanding the pressure induced absorption of both constituents at observational frequencies is therefore vital to the analysis of any observational data.

Laboratory measurements have been conducted to measure the microwave absorptivity and refractivity of phosphine and ammonia at Ka-band (32-40 GHz) and W-band (94 GHz), under conditions characteristic of the atmosphere of Saturn. The results were used to verify the accuracy of the phosphine formalism created by Hoffman *et. al* (2001) for use at millimeter wavelengths. Based on the laboratory measurements conducted, new formalisms were also created to express the opacity of ammonia at the measured frequencies.

An important method for the study of planetary atmospheres is the radio occultation experiment – a method that uses radio links between Earth, and the spacecraft which passes behind the planet. The Cassini mission to Saturn, which will be conducting such experiments at Ka-band as well as S (2.3 GHz) and X (8.4 GHz) bands, has prompted the development of a radio occultation simulator used to calculate excess

[1] Jupiter, Saturn, Uranus and Neptune also known as the Jovian or outer planets

Doppler shifts and attenuation profiles for Saturn, utilizing the newest formalisms for phosphine and ammonia. The results indicate that there will be unambiguous detection and profiling of phosphine and ammonia, and predictions are made for the pressures at which loss of signal is anticipated.

# CHAPTER 1

## INTRODUCTION

Solar system exploration is a grand enterprise performed in an attempt to explain the origins of our system of planets and to learn whether life exists beyond Earth. Differences in composition and atmospheric structure of the planets can reveal clues to their formation and evolutionary paths and even possibly provide deep insight into the evolution of Earth and the multitude of planets being discovered around other stars. The outer planets pique our interest since they have maintained a significant portion of their original atmosphere due to their large mass.

The interest in Saturn was heightened after three unmanned spacecraft, Pioneer 11, Voyager 1 and Voyager 2 flew rapidly through the Saturnian system, resulting in more questions than answers. In order to provide a comprehensive study, the Cassini/Huygens mission to Saturn was first conceptualized in the 1980s and launched in 1997. The Huygens probe was released into the atmosphere of Titan, one of Saturn's moons, in January of 2005 and the Cassini orbiter is currently on a four year mission to explore the Saturnian system. One of the many objectives of the Cassini mission involves the study of atmospheric structure of Saturn using radio occultation measurements conducted at Ka-band (32 GHz), which much of this thesis work supports, and also at S (2.3 GHz) and X (8.4 GHz) bands.

Both the charged atmosphere (ionosphere) and the neutral atmosphere (excluding the ionosphere) of Saturn will be studied by Cassini using the three frequency radio occultation experiment. Radio occultation occurs when the earth is occulted by the planet's atmosphere as viewed from the spacecraft. As the signal penetrates the neutral

atmosphere, the excess Doppler shift induced by the atmosphere as well as the changes in phase and amplitude of the spacecraft's radio signal can yield estimates of refractivity, which are related to the temperature-pressure profile of the atmosphere, as well as absorption profiles. Absorption profiles can yield atmospheric abundances of microwave absorbing constituents provided we know their attenuation properties.

Ammonia has been considered to be the dominant source of opacity in the outer planets at wavelengths in the millimeter-centimeter range. For example, all inferred opacity from the Voyager radio occultation experiments at Saturn was attributed to ammonia (Lindal *et. al*, 1985) and a contradiction occurred because the inferred ammonia abundance exceeded the saturation vapor pressure of ammonia in the upper troposphere. Detections of phosphine on Saturn (Orton *et. al*, 2000, Noll and Larson 1990, Weisstein and Serabyn, 1994) and centimeter wavelength laboratory measurements of the opacity of phosphine (Hoffman *et. al*, 2001), led to the conclusion that phosphine contributed to the absorption in the atmosphere. Phosphine and ammonia are the only microwave absorbers considered at the depths probed by the radio occultation at Saturn ($p < 2$ bars).

The objective of this work was to conduct laboratory measurements of phosphine and ammonia in a simulated Saturn atmosphere to individually characterize their properties at millimeter-wavelengths. The results can be used in the interpretation of observational data from radio astronomical observations at W-band and also to interpret radio occultation data at Ka-band.

## 1.1 Research Objectives and Organization

This thesis describes the laboratory measurements of the millimeter wavelength opacity and refractivity of phosphine in a hydrogen/helium atmosphere. They were conducted at pressures from one to two bars and at temperatures from 188 to 295 Kelvin. A model based on previous centimeter wave measurements was developed by Hoffman *et. al* (2001) which accurately predicts opacity in the 1-30 GHz range under conditions characteristic of the outer planets. This model was verified by laboratory measurements presented here in the Ka-band (32-40 GHz) range and then used to create phosphine absorptivity profiles of the upper atmosphere ($p < 2$ bars) of Saturn. Laboratory measurements of phosphine were also conducted at W-band (94 GHz) and the Hoffman *et. al* (2001) model was verified at this frequency for use in interpreting emission spectra from radio astronomical observations. Similar measurements of ammonia were conducted in a hydrogen/helium atmosphere under conditions for the outer planets to measure its opacity and refractivity at Ka-band and W-band. A new formalism was developed to describe the opacity of ammonia in a hydrogen/helium atmosphere for use only at Ka-band and a separate formalism was also developed for use at W-band.

Chapter 2 presents a theoretical background for microwave absorption, a description of the experimental apparatus used to conduct the measurements of phosphine and ammonia at Ka-band along with the results of the experiments, and a new Ka-band formalism for ammonia opacity. Chapter 3 includes the results of the measurements of phosphine and ammonia at W-band and the new formalism for ammonia at this frequency. Chapter 4 describes a radio occultation simulator which was used to simulate the radio occultation experiment by Cassini. The results were used to predict excess

Doppler shifts due to the atmosphere and also attenuation profiles of phosphine and ammonia at the three transmitter frequencies. Chapter 5 is a summary of the conclusions and contributions of this work, as well as suggestions for future work.

# CHAPTER 2

# LABORATORY MEASUREMENTS OF PHOSPHINE ($PH_3$) AND AMMONIA ($NH_3$) AT KA-BAND UNDER OUTER PLANET CONDITIONS

Although theories can reasonably explain behaviors of gaseous absorbing molecules at microwave frequencies, it is important to test these theories by conducting measurements in the laboratory. Subtle differences between the theories can result in significant errors in predictions for microwave opacity of absorbing constituents in the planetary atmospheres. Hence, the lineshape and linewidths of a collisionally broadened gas which are sensitive to the mixture of gases, as well as the pressure and temperature of the environment, are best determined empirically.

## 2.1 Motivation for New Laboratory Measurements

Laboratory results presented in Hoffman *et al.* (2001) indicate that the accuracy of previously-used centimeter-wave formalisms for the opacity of phosphine ($PH_3$) in a hydrogen/helium ($H_2$/He) atmosphere degrade considerably at wavelengths longer than 1.3 cm. Laboratory measurements conducted at centimeter wavelengths were used to develop a new formalism for the opacity of phosphine, which provided an order of magnitude improvement over previous models. A laboratory measurement program was completed to study the opacity of phosphine, under conditions characteristic of the outer planets at wavelengths shorter than 1 cm. The most compelling incentive to verify the millimeter wavelength opacity of phosphine under conditions of the outer planets is to better constrain the abundance profile of phosphine in the atmosphere of Saturn (see de Pater and Mitchell 1993). The Cassini mission to Saturn, through its CIRS (composite

infrared spectrometer) and radio science instruments, will provide data on phosphine abundance in the upper troposphere. The new 32 GHz (9.3 mm) transmitter included in the Cassini radio science subsystem can potentially be used to obtain vertical abundance profiles of phosphine in the upper troposphere of Saturn (Steffes and Mohammed, 2002). The accuracy of such phosphine profiles depends heavily on the accuracy of the expressions for 9.3 mm phosphine opacity. We have conducted experiments in the millimeter wavelength (7.5 mm to 9.2 mm) region to measure refraction and absorption of an 8 % phosphine mixture in a hydrogen/helium atmosphere using a Fabry-Perot resonator.

The Ka-band (7.5 mm to 9.2 mm) system used to measure the refractivity and opacity of phosphine is similar to that used by Joiner *et al.* (1989) to measure the opacity and refractivity of ammonia under Jovian conditions, but it is more sensitive than that system by nearly a factor of 8. The accuracy of the results was improved with the use of a computer-based acquisition and analysis system, and the use of microwave instruments which are of higher precision than those used by Joiner *et al.* (1989). The use of analyzed, custom made gas mixtures also reduced uncertainty in the mixing ratios as compared to Joiner e*t al.* (1989). As a result, new measurements of the opacity of a 2% mixture of ammonia in a hydrogen/helium atmosphere were also conducted so as to better constrain the opacity model for ammonia, which can be used in interpreting 32 GHz radio occultation experiments and 43 GHz radio emission measurements. These measurements were conducted under the same conditions as those for phosphine.

## 2.2 Theory of Microwave Absorption from Gases

The absorption of electromagnetic radiation by atmospheric gases becomes significant at centimeter and millimeter wavelengths. Incident electromagnetic radiation on gaseous molecules can produce absorption or emission of energy in the microwave or millimeter wave region. The frequency associated with this energy change is defined as $f = \Delta E/h$, where $\Delta E$ is the change between the upper and lower state energies, $h = 6.624 \times 10^{-34}$ J sec (Planck's constant) and $f$ represents the absorption or emission frequency.

There are significant differences between the energies studied in the various regions of the electromagnetic spectrum. These internal molecular energies can be separated into electronic, vibrational and rotational, typically associated with absorption or emission in the visible, infrared and microwave regions, respectively. A molecule consisting of two or more nuclei is held together by valence binding forces of electrons and balanced by internal repulsion forces. Since the inter-nuclear spacing is large compared to the diameters of the nuclei, which act as point masses, the molecule possesses moments of inertia about certain axes and can therefore rotate about them. Small changes in energy levels can produce changes in kinetic energy of rotation and thus angular velocity of rotation. The valence bond holding the nuclei together is not rigid, thus it can be stretched and compressed slightly, creating changes in intermolecular distance. This elastic bond allows the nuclei to vibrate about their equilibrium positions; however transitions between vibrational energy levels require much more energy than those of rotation. Even more energy is needed for the energy change associated with electronic arrangement. The molecule is in ground state when the outer electronic configuration is in equilibrium. The molecule has potential energy in electronic form

when the configuration is unstable due to acquisition of energy either via absorption or collision.

The energy studied in the microwave region deals mostly with lower energy rotational motion with the exception of molecular inversion, which is a form of vibrational motion, exhibited in both phosphine and ammonia molecules. Both molecules are in the form of a pyramidal structure with the phosphorus or nitrogen atom above the plane formed by the three hydrogen atoms. The configuration is shown in Figure 2.1. These molecules are known as symmetric tops since they possess axes of

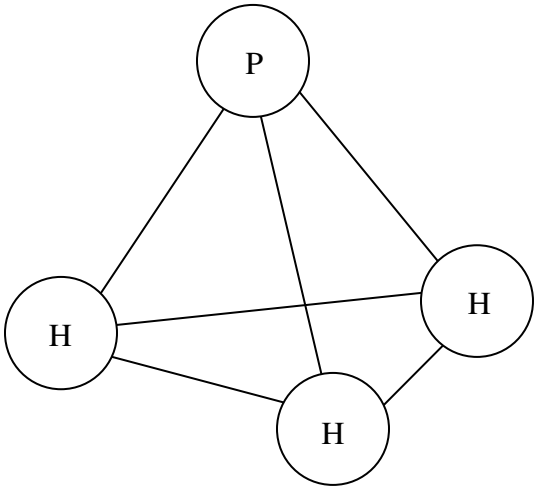


Figure 2.1: Sketch of the phosphine ($PH_3$) molecule

three fold symmetry. Molecular inversion is characterized by the tunneling of the phosphorus or nitrogen atom through the plane of hydrogen atoms and its rapid vibration to the other side. In principle, molecular inversion is a vibrational motion, which normally gives frequencies in the infrared region. However, the inversion is slowed

down by the hindering potential that the frequencies exist in the microwave region (Townes and Schawlow, 1955). The absorption of microwave radiation forms the basis for the study of the properties of the gaseous constituents.

### 2.2.1 Polar and Non-Polar Molecules

Microwave absorption of gases is also influenced by the chemical bond and the geometric configuration of the molecule. Molecules like phosphine and ammonia, also known as polar molecules, have a structure that naturally possesses a permanent dipole moment that creates an asymmetry in the charge distribution that occurs as a result of the covalent bonding. Polar molecules interact with electromagnetic radiation and are active absorbers in the microwave region; thus the greater the change in bond (dipole) moment, the greater the absorption of energy (Debye, 1929). Non-polar molecules, such as hydrogen ($H_2$) and helium (He), are not active absorbers in the microwave region, since they do not possess permanent dipole moments, but they exhibit pressure-induced absorption lines in planetary atmospheres. This absorption occurs due to transient collisionally induced dipoles. Since the bulk of the atmospheres of the Jovian planets consist of hydrogen and the remainder being mostly helium, it is important to consider the collision induced dipoles of $H_2$-$H_2$ and $H_2$-He (Trafton, 1966, Trafton, 1973). An expression to calculate the opacity utilizing the hydrogen and helium collisions is given by (Joiner and Steffes, 1991)

$$\alpha_{H_2} = \frac{1.545\times10^{-5}}{\lambda^2} P_{H_2}\left[ P_{H_2}\left(\frac{273}{T}\right)^{3.12} + 1.382 P_{He}\left(\frac{273}{T}\right)^{2.24} + 9.322 P_{CH_4}\left(\frac{273}{T}\right)^{3.34} \right] \text{ dB/km.} \tag{2.1}$$

In this formalism, (which also includes collisionally-induced opacity from methane, $CH_4$), pressure has units in bars, temperature is in Kelvin and the wavelength is in centimeters.

### 2.2.2 Lineshapes

Among the factors which determine the strength of absorption in a spectral region are the lineshape and linewidth. The main sources of spectral broadening are natural line broadening, Doppler broadening and pressure or collision broadening. From the view point of quantum mechanics, natural broadening arises from the uncertainty principle which states that the energy levels, on the time scales of transitions, are not infinitely sharp. Doppler broadening occurs when a molecule is moving parallel to the direction of propagation of the radiation being absorbed and this gives a frequency shift of $\pm \nu(\upsilon/\upsilon_p)$. The resonant frequency is $\nu$, the molecular velocity is $\upsilon$ and the velocity of phase propagation of the radiation is $\upsilon_p$ (Townes and Schawlow, 1955). Pressure broadening, which occurs due to the collisions between molecules, is the main source of broadening at the pressures considered in this work. Linewidths are also affected by the distribution of total molecular population among the various gases, both absorbing and non-absorbing, the dependence of which is found empirically.

In order to use measurements of atmospheric opacity to derive constituent abundances, both the lineshape and the line strength of the absorbing gas must be known precisely under the conditions of the atmosphere being investigated. General line shape models for predicting the absorption of gaseous mixtures in the planetary atmospheres have been developed based on classical and quantum theory of radiation. The models

used in absorption spectra are typically the Voigt (Townes and Schawlow, 1955), Lorentzian (Van Vleck and Weisskopf, 1945), Ben-Reuven (Ben-Reuven, 1966), Van Vleck-Weisskopf (Van Vleck and Weisskopf, 1945) and the Kinetic (also known as the Gross or Zhevakin-Naumov) (Gross, 1955) lineshapes. However, for modeling the opacity of phosphine and ammonia, the Van Vleck-Weisskopf and the Ben-Reuven lineshapes are used respectively, based on consistency with laboratory measurements.

### 2.2.3 Ammonia and Phosphine Spectra

Line strengths of the absorbing gases must also be known in order to determine their opacity in the Jovian atmospheres. The spectrum of ammonia has been studied extensively both theoretically and in the laboratory. As mentioned, the ammonia molecule has a pyramidal shape with the nitrogen atom at the apex. Theory states that the energy levels are split into pairs because there are two equivalent positions of equilibrium for the nitrogen atom on either side of the hydrogen plane; thus inversion lines occur at certain frequencies, corresponding to those energy levels.

The absorption spectrum of ammonia consists of a number of rotational lines at submillimeter wavelengths and a large number of inversion lines in the 16.8 GHz to 39.9 GHz region (Poynter and Kakar, 1975). The characteristics of absorption with frequency are dependent on pressure. At low pressures (<0.15 atmosphere in pure ammonia gas) the absorption lines are distinct having lineshapes of a Van Vleck-Weisskopf nature (Wrixon *et. al*, 1971). However at higher pressures, the individual lines are broadened to form a continuous absorption feature which takes on a Ben-Reuven lineshape. The

results of new ammonia measurements will be discussed later and a modified lineshape will be presented based on these results.

Although the ammonia and phosphine molecules have similar geometries, the spectrum of the phosphine molecule is somewhat different. Unlike ammonia, the inversion spectrum of phosphine is ignored since the calculated intensities are extremely low (Kroto, 1992). Thus their values are thus not included in the Pickett *et al*. (1998) catalog. Phosphine's spectrum includes weak, collisionally-induced lines at microwave frequencies and stronger rotational lines at millimeter and submillimeter wavelengths (Pickett *et al*., 1998). Hoffman *et. al* (2001) showed that any model that neglects the weak collisionally induced lines is grossly inaccurate. In order to fit centimeter-wavelength laboratory data, Hoffman *et. al* (2001) empirically derived intensity weightings for the lines lower in frequency than the first rotational line ($J = 1 \rightarrow 0$) which are collisionally induced rotational lines that have never been measured directly. This opacity model for phosphine uses a Van Vleck-Weisskopf lineshape.

### 2.2.4 Microwave Absorption of Gaseous Phosphine and Ammonia

The electric and magnetic fields of a uniform wave propagating in the $+\hat{z}$ - direction in a lossy gas are given by

$$E(z) = E_o e^{-jkz} = E_o e^{-\alpha z} e^{-j\beta z} \tag{2.2}$$

$$H(z) = H_o e^{-jkz} = H_o e^{-\alpha z} e^{-j\beta z} \tag{2.3}$$

where $E_o$ and $H_o$ are the amplitudes of the electric and magnetic fields respectively, $\alpha$ is the attenuation constant and $\beta$ is the phase constant. The propagation constants are related to the complex permittivity, $\varepsilon$, and the real permeability, $\mu$, of the lossy gas as well

as the frequency of propagation, $\omega$. The complex permittivity of the lossy gas is characterized as $\varepsilon = \varepsilon' - j\varepsilon''$. The propagation constants for the gases are (Ramo *et al.*, 1994)

$$\alpha = \omega \sqrt{\left(\frac{\mu\varepsilon'}{2}\right)\left[\sqrt{1+\left(\frac{\varepsilon''}{\varepsilon'}\right)^2} - 1\right]} \tag{2.4}$$

$$\beta = \omega \sqrt{\left(\frac{\mu\varepsilon'}{2}\right)\left[\sqrt{1+\left(\frac{\varepsilon''}{\varepsilon'}\right)^2} + 1\right]} \tag{2.5}$$

and the ratio of $\alpha$ to $\beta$ gives

$$\frac{\alpha}{\beta} = \sqrt{\frac{\sqrt{1+\left(\frac{\varepsilon''}{\varepsilon'}\right)^2} - 1}{\sqrt{1+\left(\frac{\varepsilon''}{\varepsilon'}\right)^2} + 1}}. \tag{2.6}$$

For a low loss gas, the loss tangent defined as $\varepsilon''/\varepsilon'$, is much less than unity, thus the ratio of $\alpha$ to $\beta$ reduces to

$$\frac{\alpha}{\beta} \cong \frac{\varepsilon''}{2\varepsilon'}. \tag{2.7}$$

The phase constant is $\beta = 2\pi/\lambda$, where $\lambda$ is the wavelength of the propagating wave; thus the absorption coefficient becomes

$$\alpha \cong \beta \frac{\varepsilon''}{2\varepsilon'} = \frac{\pi}{\lambda}\frac{1}{Q_{gas}} \tag{2.8}$$

where $Q_{gas} = \varepsilon'/\varepsilon''$ is the quality factor of the low loss gas. One method for determining the absorption of a gas is to use a system capable of determining its quality factor at a specific wavelength. The Fabry-Perot resonator system described in section 2.3 operates in that fashion.

## 2.3 Measurement System

As mentioned, the measurement system used for measurements of the opacity of phosphine under simulated conditions for the outer planets in the Ka-band range (7.5 – 9.2 mm) is similar to that described in Joiner *et al.* (1989). The atmospheric simulator used to conduct measurements is shown in Figure 2.2. It consists of a gas-handling subsystem, an electrical subsystem and a temperature chamber. The gaseous pressure subsystem consists of a phosphine-gas-mixture bottle, a nitrogen bottle, a vacuum gauge, a pressure gauge, and a phosphine-scrubbing canister all connected by 3/8 inch stainless-steel tubing. The pressure system is capable of handling 2 bars of pressure without detectable leakage. Due to the toxic nature of phosphine, gas masks and a sensitive gas leak detector were used during experiments or anytime the phosphine gas mixture was handled as demonstrated in Figure 2.3. When the same system was used to conduct measurements of ammonia, an ammonia-gas-mixture bottle replaced the phosphine gas-mixture bottle. The temperature chamber, capable of reaching temperatures as low as 173 K, was monitored using a J-type thermocouple while the ambient temperature was monitored with an alcohol thermometer. The electrical system includes a computer controlled HP-8564E spectrum analyzer, an HP-83560B microwave sweep generator and a Fabry-Perot resonator. A picture of the system is shown in Figure 2.4 and a picture of the Fabry-Perot resonator in the temperature chamber is shown in Figure 2.5.

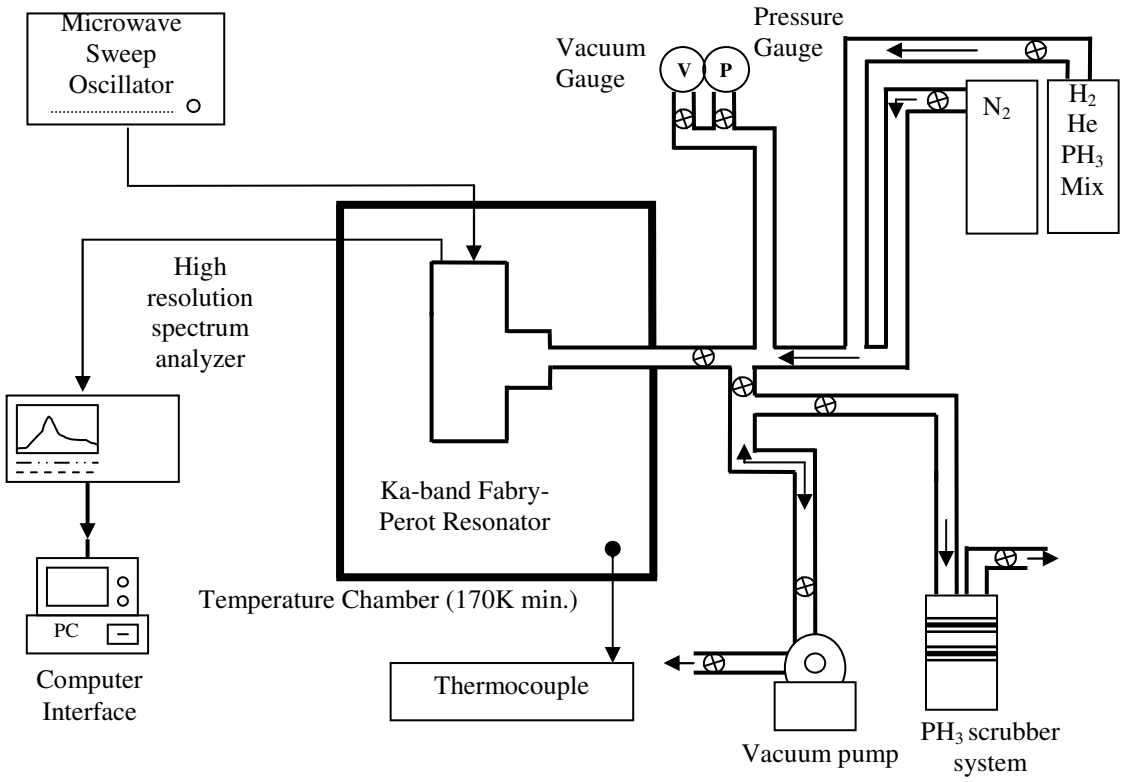


Figure 2.2: Block diagram of atmospheric simulator

Figure 2.3: Picture showing the temperature chamber with Ka-band resonator and use of gas mask and leak detector

Figure 2.4:  Picture of system

Figure 2.5: Picture of Ka-band resonator in temperature chamber

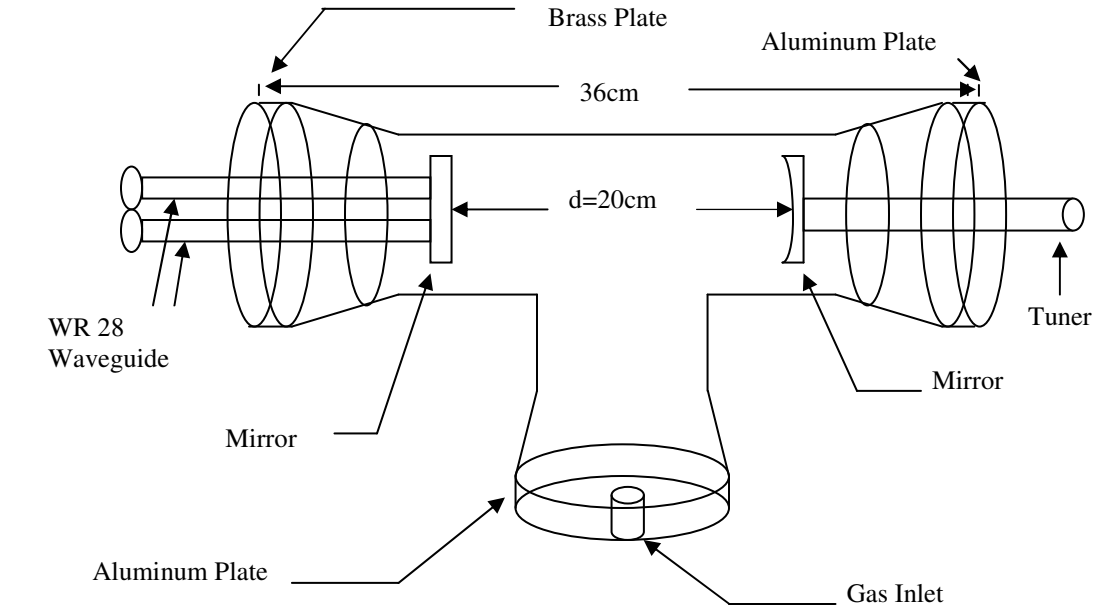


Radius of Curvature of Spherical Mirror = 2d = 40cm

Effective Path Length = $\frac{Q\lambda}{2\pi}$

Figure 2.6: Fabry-Perot resonator

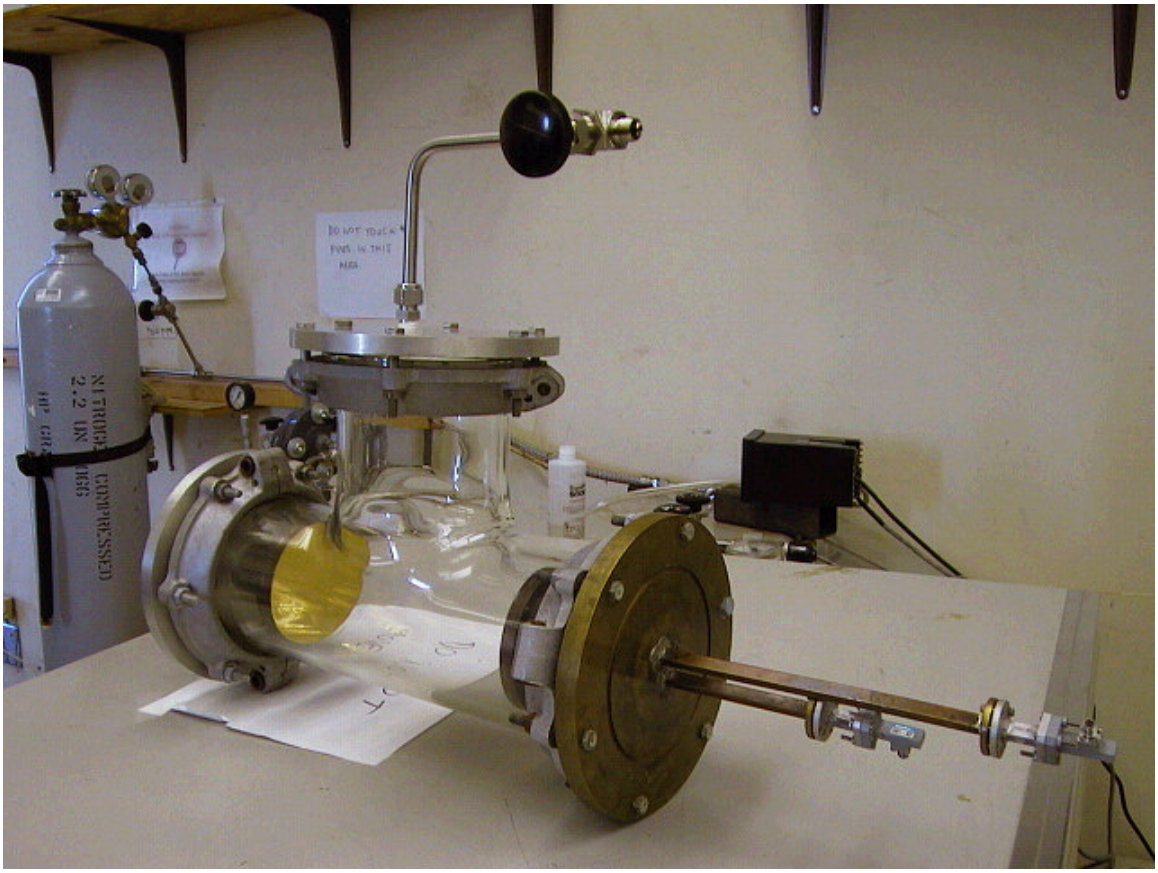


Figure 2.7: Picture of the Fabry-Perot resonator

The Fabry-Perot resonator shown in Figures 2.6 and 2.7 consists of two gold plated mirrors, one flat and one concave, set 20 cm apart. The effective path length of this resonator can be as much as 10 meters depending on the quality factor (Valkenburg and Derr, 1966). The mirrors were aligned using a beam from a helium-neon laser, which was directed to the input waveguide of the resonator. The adjustable spherical mirror was fine-tuned so that the reflected beam focuses precisely on the output iris. The Fabry-Perot resonator operates like a band pass filter at each of its resonances. The microwave sweep generator is adjusted to sweep through the range of the resonance, and

the resonance is then measured on the high-resolution spectrum analyzer. Electromagnetic energy is coupled to and from the resonator via twin irises located symmetrically on the flat mirror, and the irises are attached to two sections of WR-28 waveguide (Joiner 1991). The waveguides are sealed by O-rings and a piece of mica, which are held in place using vacuum grease. Flexible cables are used to connect the waveguide of the resonator to the spectrum analyzer and sweeper.

The advantages of a Fabry-Perot resonator over other cavity resonators are significant at millimeter wavelengths (over 30 GHz). Rectangular and circular waveguide cavities can be used at arbitrarily high frequencies; however, the inherent conductor losses can make the overall $Q$ too small to be useful in millimeter-wave measurements. Another limitation of conventional resonators is that their physical size operating in low order mode may be too small to be practical; if higher order modes are used, the resonances of the nearby modes will be too close in frequency. The finite bandwidth coupled with attenuation-induced broadening of the resonances would make the use of such cavities unfeasible. To avoid these difficulties, the sidewalls can be removed which reduces conductor losses as well as the number of possible resonant modes (Pozar 1998). The open resonator with one spherical mirror and a flat mirror placed at a distance of half of the radius of curvature apart is called a semi-confocal Fabry-Perot resonator and it confines the energy to a stable mode pattern. While the confocal type (two spherical mirrors of the same radius of curvature, separated by a distance equal to that radius) has the lowest diffraction loss (Culshaw, 1962), the semi-confocal set up proves to be more stable than the parallel plane or confocal resonators (Pozar 1998).

As mentioned earlier, the effective path length of the Fabry-Perot resonator is defined as (Valkenburg and Derr, 1966)

$$EPL = \frac{Q\lambda}{2\pi} \tag{2.9}$$

where $Q$ is the quality factor of the loaded resonator. The high $Q$ that can be maintained by this resonator (Culshaw, 1960) thus allows a large effective path length suitable for investigating absorptive properties of gases.

The achievable $Q$ of this Ka-band Fabry-Perot resonator can be 10 000, however due to the mechanical degradation of the gold plating, the $Q$ decreased to about 8000 or less, depending on the resonance. While a rectangular waveguide can also be used to achieve an equivalent path length at Ka-band, the required size would have been too large to fit in our temperature chamber. Thus, due to its physical size and effective path length, the Fabry-Perot resonator was more suitable for these experiments which were conducted over a wide range of temperatures.

The Fabry-Perot resonator was used for measurements at 32.8 GHz (9.1 mm), 35.7 GHz (8.4 mm), 37.9 GHz (7.9 mm) and 40 GHz (7.5 mm). The data was acquired by a personal computer from the spectrum analyzer via a GPIB interface. A complete description of the computer system is given in DeBoer and Steffes (1996).

## 2.4 Procedure

The opacity of a low loss gas may be calculated using the change its presence induces on the quality factor, $Q$, of a microwave cavity resonator. The $Q$ of a resonator can be described as (Matthaei *et al.* 1980)

$$Q = \frac{2\pi f_o * (EnergyStored)}{AveragePowerLoss} \tag{2.10}$$

The $Q$ can be directly measured as $f_o/BW$, where $f_o$ is the center frequency and $BW$ is the half-power bandwidth of a resonance. The $Q$ of a gas is defined as the ratio of the real part of its permittivity to its imaginary part. The opacity is related to the $Q$ of the gas by

$$\alpha = \frac{\varepsilon'' \pi}{\varepsilon' \lambda} = \frac{1}{Q_{gas}} \frac{\pi}{\lambda} \tag{2.11}$$

where $\varepsilon'$ and $\varepsilon''$ are the real and imaginary permittivity of the gas and $\alpha$ is the absorptivity of the gas in Nepers/km (Np/km) and $\lambda$ is the wavelength in km. The attenuation of 1 Np/km = 2 optical depths/km = 8.686 dB/km. To determine $Q_{gas}$, the total quality factor of the resonator must be examined. The total or measured quality factor of a gas-filled resonator is given by

$$\frac{1}{Q^m_{loaded}} = \frac{1}{Q_{gas}} + \frac{1}{Q_c} + \frac{1}{Q_{ext1}} + \frac{1}{Q_{ext2}} \tag{2.12}$$

where $Q^m_{loaded}$ is the measured quality factor of the loaded resonator, $Q_{gas}$ is the quality factor of the gas under test, $Q_c$ is the quality factor of the evacuated cavity resonator, and $Q_{ext1,2}$ represent external coupling losses (Matthaei *et al*. 1980).

When a lossy gas is introduced into the resonator, the resonance is broadened due to the opacity of the gas and the center frequency shifts due to the refractivity of the gas mixture. (The refractivity is defined as $(n\text{-}1)\times 10^6$, where $n$ is the refractive index). Since

the refractivity of the gas under test affects both $Q_{ext1}$ and $Q_{ext2}$, it is best to retrieve the value of $Q_{gas}$ by comparing the quality factor measured with the test gas present with the quality factor measured in the presence of a lossless gas with the same refractivity. In order to match the refractivity of the gas under test, the resonant center frequency is measured at vacuum; then it is measured with the test gas present after which a vacuum is drawn again and a nearly lossless reference gas is introduced to cause the same frequency shift. Gaseous nitrogen ($N_2$) was used as the reference gas, and this measurement is referred to as the matched measurement. This method is used to remove the effects of dielectric loading as described in Joiner (1991). $Q_{gas}$ can be directly calculated with the following equation:

$$\frac{1}{Q_{gas}} = \frac{1-\sqrt{t_{loaded}}}{Q^m_{loaded}} - \frac{1-\sqrt{t_{matched}}}{Q^m_{matched}} \tag{2.13}$$

where $Q^m_{loaded}$ and $t_{loaded}$ respectively are the quality factor and transmissivity of the resonator loaded with the opaque gas mixture, while $Q^m_{matched}$ and $t_{matched}$ respectively are the quality factor and transmissivity of the resonator with the lossless reference gas. This differential measurement can remove the losses, which cannot be directly measured or calculated. Substituting equation 2.13 into equation 2.11, the absorption or opacity of the lossy gas can be calculated using (Fahd and Steffes, 1992)

$$\alpha \approx \frac{\pi}{\lambda}\left(\frac{1-\sqrt{t_{loaded}}}{Q_{loaded}} - \frac{1-\sqrt{t_{matched}}}{Q_{matched}}\right). \tag{2.14}$$

The transmissivity is related to insertion loss by $t = 10^{(-S/10)}$ where S is the insertion loss in decibels. The insertion loss of the resonator was calculated by subtracting the peak power of the resonance being measured from the power through the system without the

resonator. This effectively removes losses due to the cables and gives only the loss due to the resonator. In order to measure the power through the system without the resonator, the cables were disconnected from the resonator and connected to each other using an SMA female to female connector.

## 2.5 Measurement Uncertainty

The uncertainties in the opacity measurements are calculated in a fashion similar to that described in Hoffman *et al.* (2001), but with the addition of the effects of uncertainties in mixing ratio, pressure and temperature. For our experiments, the uncertainty in mixing ratio was given by the gas vendor to be within 2 % of the stated mixing ratio. Thus for the phosphine mixture, the mixing ratio is 8.2 ± 0.164 % and for ammonia it is 2.032 ± 0.04064 %. Pressure measurements at 0.5 and 1 bar were taken using the Hastings Model 760 vacuum gauge, which has an estimated error of ± 1 mbar, while the 2 bar measurements were taken using an Omega Digital Pressure Gauge with an uncertainty in pressure of approximately ± 7 mbar. The uncertainties in the mixing ratios, as well as the uncertainties of the measurements from the pressure and vacuum gauges were given by their respective manufacturers. Uncertainty in the mixing ratio due to adsorption of the radio-absorbing constituent in the gas mixture by the surfaces within the pressure vessel has been found to be very small. In a system similar to ours, the adsorption of ammonia to the surfaces is on the order of 1 ppm (Hartman *et al.* 1995); thus for an ammonia mixing ratio of 2.032 % this is negligible. Since phosphine is less adsorbing, the adsorption of this gas to the surfaces would be even less (D. P. Campbell private communication).

The system temperature was evaluated with the use of a J type thermocouple. The uncertainty in system temperature is based on the resolution of the digital voltmeter used to monitor the thermocouple, as well as the resolution of the alcohol thermometer used to measure the reference room temperature and the variation of the temperature chamber due to the control system. The resolution of the digital voltmeter is 0.1 mV which yields a temperature uncertainty of ± 1.4 K. The error attributed to the alcohol thermometer is ± 0.5 K and that due to the regulation of temperature chamber is ± 2 K. The total uncertainty in system temperature is therefore ± 3.9 K. Since the temperature error is considered to be random, its effect on opacity is included in the quadrature sum of the variances of errors due to transmissivity, dielectric matching and electrical noise and instrumentation. Errors due to mixing ratio and pressure variation are fixed and are thus added as constants to the total uncertainty due to other errors. At room temperature the uncertainty in temperature is only ± 2.5 K since the thermocouple is not used for these experiments.

Bandwidth, center frequency and transmissivity are the measurable quantities used to calculate opacity. Electrical noise and instrumental uncertainties are responsible for measurement errors in center frequency and bandwidth. The best estimation of the bandwidth is the mean of many measurements since electrical noise is uncorrelated. The corresponding error estimate is the sample standard deviation weighted by the confidence coefficient (B),

$$\sigma_N^2 = B\frac{S_N^2}{N} \tag{2.15}$$

where $S_N$ is the sample standard deviation. For each set of ten independent measurement taken, the confidence interval used is 90 % giving a confidence coefficient of B = 1.88

(Papoulis, 1991). Errors due to the instrument are estimated and the standard deviations for center frequency and bandwidth measurements, respectively, are estimated by (Hewlett-Packard, 1997),

$$\sigma_o \approx (1\times10^{-7}\times years\_since\_calibrated + 3.2\times10^{-8})f_o + 0.15RBW + 0.01SPAN + 10 \text{ Hz} \tag{2.16}$$

$$\sigma_\Delta \approx BW\,(1\times10^{-7}\times years\_since\_calibrated + 3.2\times10^{-8}) + 4N + 2LSD \text{ Hz} \tag{2.17}$$

where $f_o$, $RBW$, $SPAN$, $N$ and $LSD$ are the center frequency, resolution bandwidth, frequency span, mixer integer and least significant digit of the spectrum analyzer frequency display, respectively. All quantities are in Hertz except $N$. The error due to electrical noise and instrumentation is calculated using

$$\sigma_\psi^2 = \left\langle \Gamma_u^2 \right\rangle + \left\langle \Gamma_l^2 \right\rangle - 2\left\langle \Gamma_u \Gamma_l \right\rangle \tag{2.18}$$

where

$$\left\langle \Gamma_i^2 \right\rangle = \frac{\gamma_i^2}{f_{oi}^2}\left[\frac{\sigma_o^2}{Q_i^2} + \sigma_\Delta^2 + \sigma_{Ni}^2 + \frac{2\sigma_o\sigma_\Delta}{Q_i}\right] \quad i = u,l \tag{2.19}$$

and where

$$\left\langle \Gamma_u \Gamma_l \right\rangle = -\frac{\gamma_u\gamma_l}{f_{ol}f_{ou}}\left[\frac{\sigma_o^2}{Q_lQ_u} + \sigma_\Delta^2 + \frac{\sigma_o\sigma_\Delta}{Q_l} + \frac{\sigma_o\sigma_\Delta}{Q_u}\right] \tag{2.20}$$

and

$$Q_i = \frac{f_{oi}}{\Delta f_i}, \quad i = u,l \tag{2.21}$$

(DeBoer and Steffes 1994). The subscript $i$, is for $u$ and $l$ denoting equations for the unloaded and loaded resonator, respectively. $\gamma_{u,l}$, $f_{o(u,l)}$, and $\Delta f_{u,l}$ represent the $1-\sqrt{\text{t}}$ terms

from the numerator in equation 2.13, center frequency and bandwidth of the unloaded and loaded resonator, respectively. The one sigma uncertainty of the measured gas opacity due to instrumentation errors and electrical noise is thus

$$\sigma_n = \pm \frac{8.686\pi}{\lambda} \sigma_\psi \quad \text{dB/km} \tag{2.22}$$

The total one sigma uncertainty of the opacity of the measured gas is the quadrature sum of the standard deviations

$$\sigma_{combined} = \sqrt{\sigma_n^2 + \sigma_{diel}^2 + \sigma_{trans}^2 + \sigma_{Temp}^2} \quad \text{dB/km} \tag{2.23}$$

Errors in transmissivity ($\sigma_{trans}$) and dielectric matching ($\sigma_{diel}$) were calculated as in Hoffman *et al.* (2001). The equivalent error in opacity due to temperature variations was calculated by first subtracting 3.9 Kelvin from the measured system temperature and using it in the appropriate model for absorption described in sections 2.5 and 2.6. This modeled result was considered to be the maximum positive change in opacity due to temperature variation. The corresponding reduction in opacity due to temperature variation was calculated by adding 3.9 Kelvin to the measured system temperature and using this as the temperature in the model. The error due to temperature variation was then set to half the difference between these values. The errors in opacity due to mixing ratio uncertainty and pressure variation were calculated in the same fashion. Note that this is especially important for mixing ratios, since the relationship between mixing ratio and opacity is non-linear for the relatively high abundances of $NH_3$ (2 %) and $PH_3$ (8 %) used in our experiments, due to self-broadening from the absorbing constituents. The total error is then

$$\sigma_{Total} = \sigma_{Combined} + Error_{MixingRatio} + Error_{\mathrm{Pressure}} \quad \text{dB/km} \tag{2.24}$$

## 2.6 Results

Laboratory measurements of opacity and refractivity were made of a phosphine mixture under simulated Saturn conditions at frequencies (wavelengths) of 32.7 GHz (9.2 mm), 35.6 GHz (8.4 mm), 37.7 GHz (8.0 mm) and 39.9 GHz (7.5 mm). The gaseous mixture consisted of 82.6 % hydrogen ($H_2$), 9.2 % helium (He) and 8.2 % phosphine ($PH_3$). Measurements were conducted at pressures of 0.5 bar, 1 bar and 2 bars and at temperatures of 293 K, 209 K and 188 K. Additionally, new high-precision laboratory measurements of the opacity and refractivity of $NH_3$ in an $H_2$/He atmosphere were completed under the same temperature and pressure conditions described for $PH_3$. The gaseous ammonia mixture consisted of 92.338 % hydrogen ($H_2$), 5.630 % helium (He) and 2.032 % ammonia ($NH_3$). The system was not sensitive enough to detect any measurable opacity (i.e., greater than 3.5 dB/km) from the phosphine mixture at a pressure of 0.5 bar at temperatures of either 295 K or 210 K. However, laboratory results for all other measurements of mixtures containing both phosphine and ammonia are shown in Tables 2.1 – 2.7.

As shown in Figure 2.8, the results of the measurements of the phosphine mixtures indicate that the formalism developed by Hoffman *et al.* (2001) is valid at longer millimeter wavelengths (7.5 – 9.2 mm). This formalism utilizes a Van Vleck-Weisskopf lineshape and line intensities from the JPL catalog (Pickett *et al.* 1998), which have been selectively weighted to match the laboratory data. The collisionally induced rotational lines which are lower in frequency than the first rotational line of $J = 1 \rightarrow 0$ (267 GHz) have not been measured directly, thus in order to fit the data, weightings were given to those lines below 40 GHz.

The results of the millimeter wavelength measurements of the opacity of the ammonia mixture shown in Figures 2.9 and 2.10 indicate that current absorption models for ammonia have limited accuracy in this region of the spectrum under Saturn conditions. It appears that the Joiner-Steffes model (Joiner and Steffes, 1991) understates the opacity at 9.2 mm, while the Berge and Gulkis model (1976) appears to overstate the opacity at wavelengths less than 8.6 mm.

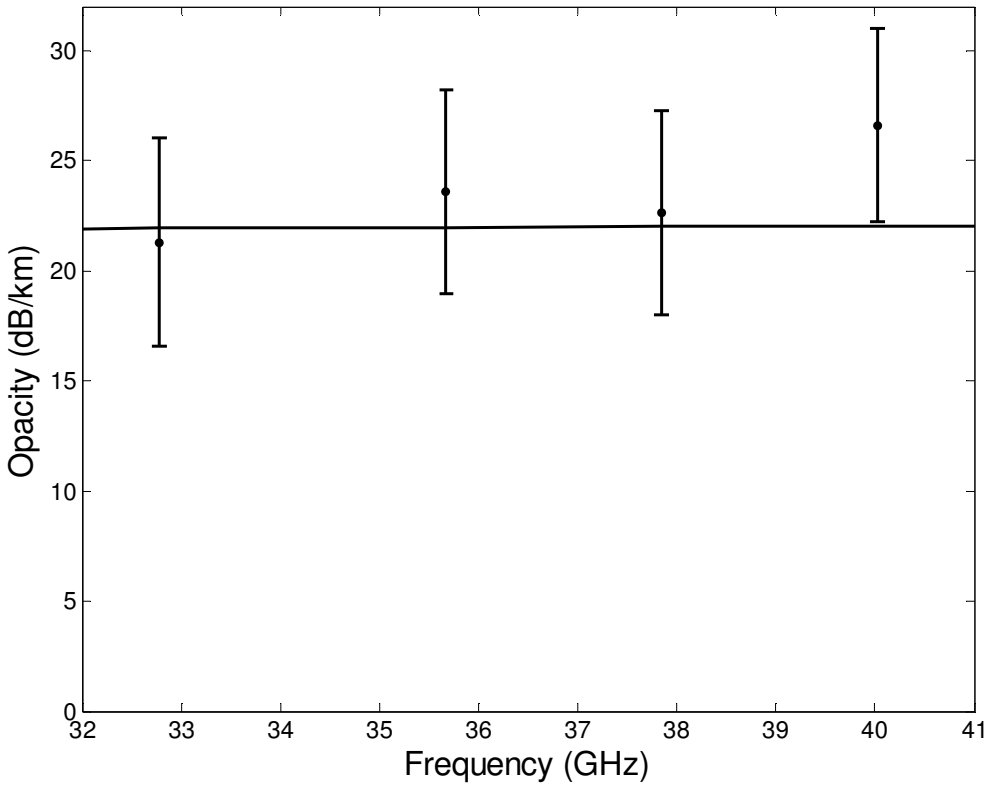


Figure 2.8: May 16, 2002 laboratory measurements compared to the Hoffman formalism for phosphine absorption. Measurements were taken at a temperature of 210 K and a pressure of 1.916 bars with a mixing ratio of 82.6 % $H_2$, 9.2 % He, 8.2 % $PH_3$.

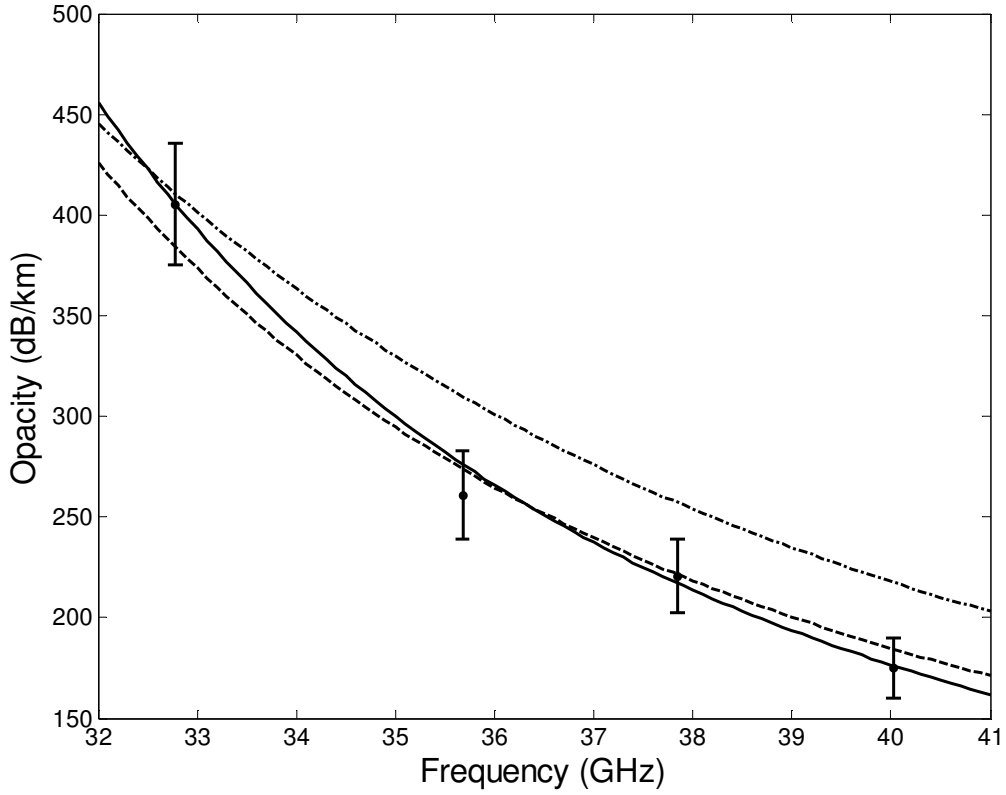


Figure 2.9: July 29, 2002 laboratory measurements compared to various formalisms for $NH_3$ absorption. Measurements were taken at a temperature of 186 K and a pressure of 1.964 bars with a mixing ratio of 92.338 % $H_2$, 5.63 % He, 2.032 % $NH_3$. The solid line is the new formalism for ammonia absorption for use at Ka-band (7.5 – 9.2 mm); the dashed line is the Joiner/Steffes (1991) model for ammonia opacity and the dotted-dashed line is the Berge and Gulkis (1976) model for ammonia opacity.

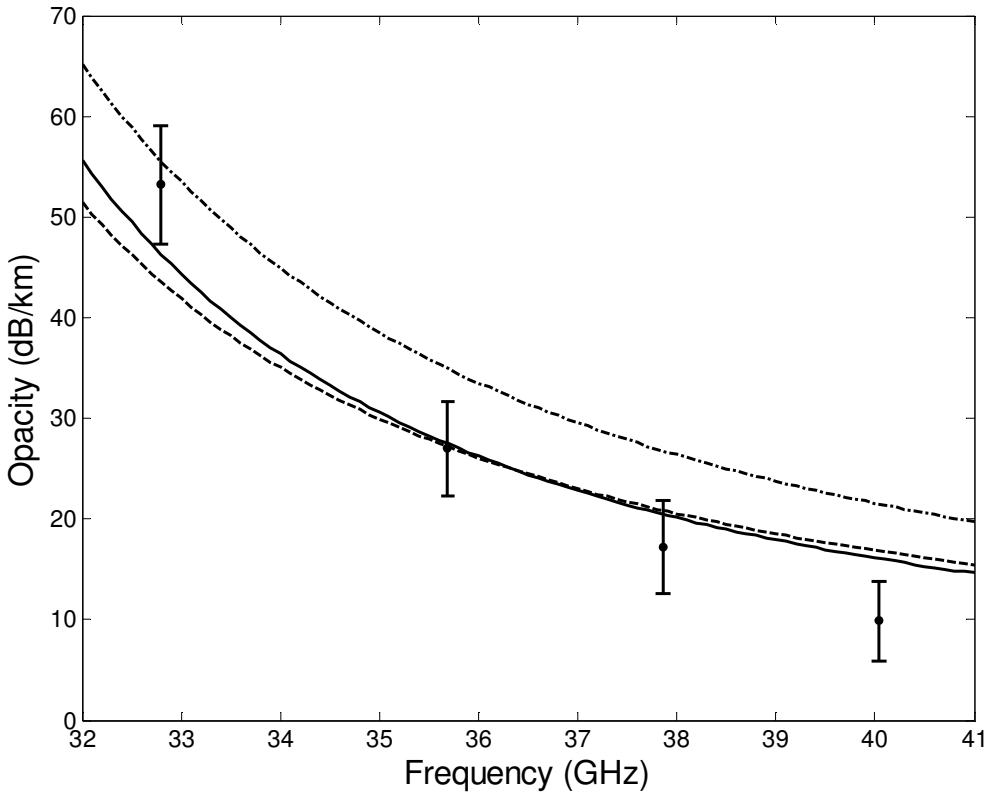


Figure 2.10: July 29, 2002 Laboratory measurements compared to various formalisms for $NH_3$ absorption. Measurements were taken at a temperature of 186 K and a pressure of 0.564 bars with a mixing ratio of 92.338 % $H_2$, 5.63 % He, 2.032 % $NH_3$. The solid line is the new formalism for ammonia absorption for use at Ka-band (7.5 – 9.2 mm); the dashed line is the Joiner/Steffes (1991) model for ammonia opacity and the dotted-dashed line is the Berge and Gulkis (1976) model for ammonia opacity.

Table 2.1: Results of phosphine opacity measurements at 188 K. Gas mixture composition: 82.6 % $H_2$, 9.2 % He, 8.2 % $PH_3$

| Date | Pressure (bars) | Frequency (GHz) | Hoffman Model (dB/km) | Opacity: Measured (dB/km) | Measurement $\sigma\pm$ (dB/km) | Normalized Refractivity (N-units $cm^3$ $mol^{-1}$)$\times 10^{17}$ |
|---|---|---|---|---|---|---|
| 06/21/2002 | 0.507 | 32.79 | 2.1257 | 7.7081 | 4.0566 | 4.28202 ± 0.44720 |
| T = 188 K | | 35.69 | 2.1281 | -5.6124 | 3.7096 | 4.03403 ± 0.44174 |
| | | 37.86 | 2.1300 | 5.2132 | 3.7417 | 3.99636 ± 0.39803 |
| | | 40.04 | 2.1322 | 1.8709 | 3.5799 | 4.11873 ± 0.33452 |
| | 0.989 | 32.79 | 8.0750 | 11.5550 | 4.2848 | 4.71300 ± 0.39129 |
| | | 35.68 | 8.0860 | -0.4635 | 3.9117 | 4.35328 ± 0.31526 |
| | | 37.86 | 8.0946 | 8.7636 | 4.0237 | 4.47863 ± 0.36126 |
| | | 40.03 | 8.1036 | 7.1554 | 3.7404 | 4.43034 ± 0.32356 |
| 06/24/2002 | 0.508 | 32.79 | 2.1341 | -0.4589 | 4.0760 | 4.45315 ± 0.45417 |
| T = 188 K | | 35.69 | 2.1365 | 2.3476 | 3.7113 | 4.36489 ± 0.36810 |
| | | 37.86 | 2.1384 | 4.5132 | 3.7333 | 4.63657 ± 0.40866 |
| | | 40.04 | 2.1406 | 2.3705 | 3.6577 | 4.56722 ± 0.35357 |
| | 0.993 | 32.79 | 8.1403 | 11.6179 | 4.3853 | 4.57512 ± 0.41433 |
| | | 35.68 | 8.1515 | 8.6554 | 4.9530 | 4.49275 ± 0.32988 |
| | | 37.86 | 8.1601 | 8.0579 | 4.0992 | 4.69152 ± 0.36141 |
| | | 40.03 | 8.1692 | 9.7316 | 3.8196 | 4.62974 ± 0.31578 |

Table 2.2: Results of phosphine opacity measurements at 210 K. Gas mixture composition: 82.6 % $H_2$, 9.2 % He, 8.2 % $PH_3$

| Date | Pressure (bars) | Frequency (GHz) | Hoffman Model (dB/km) | Opacity: Measured (dB/km) | Measurement $\sigma\pm$ (dB/km) | Normalized Refractivity (N-units $cm^3$ $mol^{-1}$)$\times 10^{17}$ |
|---|---|---|---|---|---|---|
| 05/16/2002 | 0.993 | 32.79 | 5.9205 | 2.4196 | 4.1438 | 4.63784 ± 0.40911 |
| T = 210 K | | 35.69 | 5.9278 | 1.9959 | 3.8980 | 4.33461 ± 0.28666 |
| | | 37.86 | 5.9335 | 0.7629 | 3.9479 | 4.72519 ± 0.31980 |
| | | 40.03 | 5.9396 | 6.7647 | 3.7539 | 4.71745 ± 0.29965 |
| | 1.916 | 32.78 | 21.9259 | 21.3093 | 4.7459 | 4.74898 ± 0.28670 |
| | | 35.68 | 21.9706 | 23.5872 | 4.6096 | 4.55291 ± 0.23111 |
| | | 37.85 | 22.0020 | 22.6388 | 4.6148 | 4.75687 ± 0.25933 |
| | | 40.02 | 22.0324 | 26.6142 | 4.4154 | 4.66975 ± 0.23722 |
| 05/21/2002 | 0.997 | 32.79 | 6.0508 | 6.1057 | 4.0856 | 4.87372 ± 0.40739 |
| T = 209 K | | 35.68 | 6.0583 | 4.2653 | 3.8148 | 4.64586 ± 0.31944 |
| | | 37.86 | 6.0642 | 8.2187 | 3.9494 | 4.82381 ± 0.36155 |
| | | 40.03 | 6.0705 | 5.7150 | 3.6799 | 4.80602 ± 0.31268 |
| | 1.943 | 32.78 | 22.8547 | 18.7515 | 4.7915 | 5.02990 ± 0.38301 |
| | | 35.67 | 22.9023 | 27.7102 | 4.6450 | 4.85572 ± 0.33513 |
| | | 37.85 | 22.9356 | 24.9129 | 4.6730 | 5.04133 ± 0.36097 |
| | | 40.02 | 22.9679 | 26.8433 | 4.3052 | 4.93514 ± 0.33175 |

Table 2.3: Results of phosphine opacity and refractivity measurements at room temperature, 295 K. Gas mixture composition: 82.6 % $H_2$, 9.2 % He, 8.2 % $PH_3$

| Date | Pressure (bars) | Frequency (GHz) | Hoffman Model (dB/km) | Opacity: Measured (dB/km) | Measurement $\sigma\pm$ (dB/km) | Normalized Refractivity (N-units $cm^3$ $mol^{-1}$)$\times 10^{17}$ |
|---|---|---|---|---|---|---|
| 08/22/2001 | 0.995 | 32.67 | 2.2151 | 0.3927 | 3.8274 | 9.88242 ± 0.46658 |
| T = 295 K | | 35.55 | 2.2171 | -1.5134 | 3.7367 | 10.0589 ± 0.45362 |
| | | 37.72 | 2.2188 | 1.0397 | 3.8778 | 10.3715 ± 0.48840 |
| | | 39.88 | 2.2209 | 1.6424 | 3.8288 | 10.3996 ± 0.45466 |
| | 1.778 | 32.66 | 7.0560 | 5.8760 | 4.2205 | 10.6621 ± 0.53077 |
| | | 35.54 | 7.0649 | 6.3722 | 3.9629 | 10.8643 ± 0.51054 |
| | | 37.71 | 7.0716 | 8.6373 | 3.9536 | 10.9767 ± 0.51336 |
| | | 39.87 | 7.0786 | 8.0925 | 3.9340 | 11.0064 ± 0.51690 |
| 08/29/2001 | 0.997 | 32.67 | 2.2463 | 1.7947 | 3.7093 | 9.80056 ± 0.46409 |
| T = 294 K | | 35.55 | 2.2484 | 0.5278 | 3.7662 | 10.2553 ± 0.47476 |
| | | 37.72 | 2.2501 | -1.1317 | 3.8165 | 10.1554 ± 0.46812 |
| | | 39.88 | 2.2522 | 0.7750 | 3.7083 | 10.3149 ± 0.45827 |
| | 1.916 | 32.66 | 8.2711 | 9.0242 | 3.9529 | 10.7344 ± 0.50991 |
| | | 35.54 | 8.2822 | 7.1015 | 3.8889 | 11.0369 ± 0.51852 |
| | | 37.71 | 8.2905 | 9.3281 | 4.0630 | 10.9930 ± 0.52209 |
| | | 39.87 | 8.2990 | 7.4883 | 3.9701 | 9.72183 ± 0.51467 |

Table 2.4: Results of ammonia opacity and refractivity measurements at 186 K. Gas mixture composition: 92.338 % $H_2$, 5.63 % He, 2.032 % $NH_3$

| Date | Pressure (bars) | Frequency (GHz) | New Model (dB/km) | Opacity: Measured (dB/km) | Measurement $\sigma\pm$ (dB/km) | Normalized Refractivity (N-units $cm^3$ $mol^{-1}$)$\times 10^{17}$ |
|---|---|---|---|---|---|---|
| 07/25/2002 | 0.509 | 32.79 | 38.1211 | 40.8858 | 5.6085 | 3.15873 ± 1.50364 |
| T = 186 K | | 35.69 | 22.4589 | 16.3554 | 4.6132 | 4.48694 ± 1.00534 |
| | | 37.86 | 16.7150 | 26.6079 | 4.6174 | 6.82503 ± 1.15550 |
| | | 40.04 | 13.1028 | 16.0303 | 3.9246 | 8.28841 ± 1.07636 |
| | 1.007 | 32.79 | 135.6194 | 145.7977 | 11.2021 | 5.72446 ± 1.17244 |
| | | 35.69 | 83.8601 | 86.8542 | 7.8508 | 6.17671 ± 0.94610 |
| | | 37.86 | 63.3200 | 76.5261 | 6.8277 | 7.79525 ± 1.07031 |
| | | 40.03 | 50.1103 | 52.5224 | 5.6285 | 8.29736 ± 0.95331 |
| | 1.985 | 32.78 | 411.9045 | 409.1392 | 30.0895 | 8.29882 ± 1.29060 |
| | | 35.68 | 281.0388 | 272.1779 | 22.1121 | 7.51346 ± 1.06640 |
| | | 37.85 | 220.9625 | 229.7013 | 18.2146 | 8.60075 ± 1.12246 |
| | | 40.02 | 179.5090 | 178.5650 | 15.1057 | 8.45575 ± 0.97944 |
| 07/29/2002 | 0.564 | 32.79 | 46.3493 | 53.2187 | 5.8876 | 4.63744 ± 1.47855 |
| T = 186 K | | 35.69 | 27.4584 | 27.0029 | 4.7058 | 5.50201 ± 1.14056 |
| | | 37.86 | 20.4623 | 17.1491 | 4.6006 | 6.80188 ± 1.23373 |
| | | 40.04 | 16.0567 | 9.8543 | 3.9024 | 7.96028 ± 1.03690 |
| | 0.999 | 32.79 | 133.6993 | 133.7503 | 10.9646 | 5.96030 ± 1.30185 |
| | | 35.69 | 82.6076 | 75.9594 | 7.6732 | 6.06174 ± 0.97841 |
| | | 37.86 | 62.3574 | 63.5056 | 6.7889 | 7.39970 ± 1.08842 |
| | | 40.03 | 49.3407 | 48.8298 | 5.5804 | 7.92224 ± 0.97019 |
| | 1.964 | 32.78 | 405.6193 | 405.3069 | 30.1019 | 8.44531 ± 1.32182 |
| | | 35.68 | 276.1673 | 260.8589 | 21.8506 | 7.66741 ± 1.05813 |
| | | 37.85 | 216.9245 | 220.6590 | 17.9607 | 8.60683 ± 1.14281 |
| | | 40.02 | 176.1142 | 175.0842 | 14.9543 | 8.31797 ± 1.00707 |

Table 2.5: Results of ammonia opacity measurements at 189 K. Gas mixture composition: 92.338 % $H_2$, 5.63 % He, 2.032 % $NH_3$

| Date | Pressure (bars) | Frequency (GHz) | New Model (dB/km) | Opacity: Measured (dB/km) | Measurement $\sigma\pm$ (dB/km) | Normalized Refractivity (N-units $cm^3$ $mol^{-1}$)$\times 10^{17}$ |
|---|---|---|---|---|---|---|
| 07/15/2002 | 0.504 | 32.79 | 36.0981 | 28.7352 | 5.3816 | 3.07992 ± 1.35831 |
| T = 189 K | | 35.69 | 21.1772 | 23.2852 | 4.4900 | 4.50616 ± 1.21930 |
| | | 37.86 | 15.7420 | 17.6012 | 4.3052 | 6.27352 ± 1.26598 |
| | | 40.04 | 12.3269 | 9.1885 | 3.8644 | 6.57495 ± 0.99826 |
| | 0.993 | 32.79 | 127.4767 | 121.1515 | 10.6522 | 5.03797 ± 1.26591 |
| | | 35.69 | 78.5190 | 76.3259 | 7.4101 | 5.63205 ± 1.02818 |
| | | 37.86 | 59.1961 | 60.1903 | 6.3765 | 7.04186 ± 1.13867 |
| | | 40.03 | 46.7986 | 45.6975 | 5.3953 | 7.65217 ± 0.91922 |

Table 2.6: Results of ammonia opacity and refractivity measurements at 207 K. Gas mixture composition: 92.338 % $H_2$, 5.63 % He, 2.032 % $NH_3$

| Date | Pressure (bars) | Frequency (GHz) | New Model (dB/km) | Opacity: Measured (dB/km) | Measurement $\sigma\pm$ (dB/km) | Normalized Refractivity (N-units $cm^3$ $mol^{-1}$)$\times 10^{17}$ |
|---|---|---|---|---|---|---|
| 07/19/2002 | 0.501 | 32.79 | 29.3920 | 27.0621 | 5.2536 | 3.20312 ± 1.38755 |
| T = 207 K | | 35.69 | 16.8140 | 18.0662 | 4.2668 | 4.98328 ± 1.00375 |
| | | 37.86 | 12.4107 | 15.6728 | 4.4115 | 7.80832 ± 1.32394 |
| | | 40.04 | 9.6450 | 10.3777 | 3.8388 | 6.81764 ± 0.90406 |
| | 0.985 | 32.79 | 102.3182 | 104.8155 | 8.5158 | 5.38489 ± 1.28659 |
| | | 35.69 | 61.9775 | 63.8827 | 6.1984 | 6.25298 ± 0.91125 |
| | | 37.86 | 46.4004 | 45.3389 | 5.5631 | 7.57037 ± 1.02779 |
| | | 40.03 | 36.4943 | 38.3517 | 4.8533 | 7.67430 ± 0.87481 |
| | 2.005 | 32.78 | 331.0471 | 356.0231 | 23.7574 | 8.52043 ± 1.18135 |
| | | 35.68 | 222.4045 | 222.9518 | 16.7104 | 7.89840 ± 0.97319 |
| | | 37.85 | 173.4576 | 191.5570 | 13.7636 | 9.06892 ± 1.16445 |
| | | 40.02 | 140.0816 | 150.2806 | 11.5370 | 8.53447 ± 0.93471 |
| 07/22/2002 | 0.555 | 32.79 | 35.6259 | 38.2973 | 5.4131 | 4.44791 ± 1.58875 |
| T = 207 K | | 35.69 | 20.5318 | 21.7436 | 4.3462 | 5.73923 ± 1.06882 |
| | | 37.86 | 15.1742 | 18.3445 | 4.3330 | 7.41329 ± 1.18348 |
| | | 40.04 | 11.8127 | 12.5591 | 4.0524 | 7.00759 ± 0.95524 |
| | 0.985 | 32.79 | 102.3203 | 100.3090 | 8.5132 | 5.82041 ± 1.12961 |
| | | 35.69 | 61.9775 | 64.9166 | 6.1875 | 6.25298 ± 0.91125 |
| | | 37.86 | 46.4010 | 53.0752 | 5.5519 | 7.94758 ± 1.08059 |
| | | 40.03 | 36.4947 | 37.9105 | 5.0101 | 7.67438 ± 8.39108 |
| | 1.992 | 32.78 | 327.9123 | 362.1731 | 22.9979 | 9.16207 ± 1.42694 |
| | | 35.68 | 220.0105 | 230.7847 | 16.5562 | 8.10505 ± 1.04290 |
| | | 37.85 | 171.4925 | 195.5789 | 13.7210 | 9.28331 ± 1.17602 |
| | | 40.02 | 138.4416 | 155.1310 | 11.5669 | 8.56895 ± 0.93727 |

Table 2.7: Results of ammonia opacity and refractivity measurements at 297 K. Gas mixture composition: 92.338 % $H_2$, 5.63 % He, 2.032 % $NH_3$

| Date | Pressure (bars) | Frequency (GHz) | New Model (dB/km) | Opacity: Measured (dB/km) | Measurement $\sigma\pm$ (dB/km) | Normalized Refractivity (N-units $cm^3$ $mol^{-1}$)$\times 10^{17}$ |
|---|---|---|---|---|---|---|
| 08/05/2002 | 0.503 | 32.79 | 16.7398 | 22.0650 | 5.2418 | 13.3756 ± 3.0271 |
| T = 297 K | | 35.68 | 8.3935 | 6.3385 | 4.1504 | 14.8939 ± 1.6631 |
| | | 37.86 | 6.1645 | 5.2384 | 4.0761 | 14.8188 ± 1.7113 |
| | | 40.04 | 4.3061 | 3.1453 | 3.8492 | 15.7542 ± 1.3067 |
| | 0.996 | 32.79 | 51.6652 | 57.2298 | 7.5628 | 13.7153 ± 2.4042 |
| | | 35.68 | 28.8251 | 28.2725 | 4.8261 | 15.2478 ± 1.2465 |
| | | 37.86 | 20.9509 | 21.9850 | 4.4233 | 14.6368 ± 1.3099 |
| | | 40.03 | 15.7003 | 15.5775 | 4.1734 | 15.6100 ± 1.0132 |
| | 1.999 | 32.78 | 155.6697 | 149.8020 | 9.4374 | 14.8224 ± 1.4857 |
| | | 35.68 | 98.5701 | 103.1104 | 6.7308 | 15.4011 ± 1.1788 |
| | | 37.85 | 74.3636 | 82.1772 | 6.0610 | 15.0426 ± 1.1526 |
| | | 40.02 | 58.3314 | 54.7253 | 5.3777 | 15.7315 ± 1.0653 |
| 08/07/2002 | 0.512 | 32.79 | 17.2339 | 18.8247 | 5.5040 | 12.7207 ± 2.2414 |
| T = 297 K | | 35.69 | 8.6453 | 6.7343 | 4.1792 | 15.3168 ± 1.7731 |
| | | 37.86 | 6.3564 | 6.8454 | 4.0124 | 15.1795 ± 1.5090 |
| | | 40.04 | 4.4495 | 4.3201 | 4.2144 | 15.0569 ± 1.1750 |
| | 0.992 | 32.79 | 51.3206 | 63.2558 | 7.8941 | 13.2459 ± 2.0223 |
| | | 35.68 | 28.6136 | 30.6515 | 4.6390 | 14.8350 ± 1.2342 |
| | | 37.86 | 20.7956 | 20.9081 | 4.4286 | 14.7915 ± 1.1560 |
| | | 40.03 | 15.5793 | 16.0520 | 4.5788 | 15.2606 ± 1.0529 |
| | 2.026 | 32.78 | 158.7883 | 160.0005 | 9.7569 | 14.6106 ± 1.3775 |
| | | 35.68 | 100.8186 | 107.5558 | 7.3069 | 15.4359 ± 1.1751 |
| | | 37.85 | 76.1456 | 82.9036 | 6.3818 | 15.0500 ± 1.2272 |
| | | 40.02 | 59.7822 | 60.4634 | 6.3301 | 15.4523 ± 1.0270 |

## 2.7 Formalism for Ammonia Millimeter-Wavelength Opacity

In order to better match the laboratory results, a new formalism was developed using the Ben-Reuven lineshape (Ben-Reuven 1966) with a correction factor for use at Ka-band (7.5 mm to 9.2 mm). The equation for the absorption of a gas that has been pressure broadened by foreign gases is defined as

$$\alpha = \left(\sum A_j \pi \Delta\nu_j F_j(\nu, \nu_{oj}, ...) D_j\right) \text{ cm}^{-1}. \tag{2.25}$$

The individual line number is $j$; $A_j$, is the absorption at the line center, $\Delta\nu_j$ is the linewidth, $F_j$ is the lineshape function and $D_j$ is the correction factor which is a function of the line center and the frequency. The additional correction factor used in the new formalism defined for each line is

$$D_j = \frac{1.7197\nu^{0.0619}}{(5.4015 + |\nu - \nu_{oj}|)^{0.266}} \tag{2.26}$$

where the value $\nu_{oj}$ is the line center and $\nu$ is the frequency at which the absorption is being calculated. The absorption at the line center is calculated using the equation

$$A_j = \frac{nS_j(T)}{\pi\Delta\nu_j} \text{ cm}^{-1} \tag{2.27}$$

where $n$ is the number density, $S_j(T)$ is the intensity of the line $j$, which is the scaled intensity calculated at the reference temperature $T_o$ (Pickett *et al.* 1998). The resulting expression for the line center absorption is

$$A_j = \frac{10^6 P(bar)}{\pi k_B T \Delta\nu_j (cm^{-1})} \left(\frac{T_o}{T}\right)^{\eta+1} S_j(T_o) e^{-(hc/k)E_{lj}(1/T - 1/T_o)} \text{ cm}^{-1}. \tag{2.28}$$

The $E_{lj}$ term is the lower state energy at each line which is obtained from the the Poynter/Pickett catalog (Pickett *et al.* 1998) and $\eta$, the temperature dependence term, is

1.5 for symmetric-top molecules such as phosphine and ammonia. The linewidth for the gaseous mixture is found using (Joiner and Steffes, 1991)

$$\Delta\nu_j = 1.69P_{H_2}\left(\frac{300}{T}\right)^{2/3} + 0.75P_{He}\left(\frac{300}{T}\right)^{2/3} + 0.6P_{NH_3}\left(\frac{300}{T}\right)\Delta\nu_{oj} \tag{2.29}$$

where the line self broadening parameters $\Delta\nu_{oj}$ are from Poynter and Kakar (1975). The Ben-Reuven lineshape also uses a coupling element term given by (Joiner and Steffes, 1991)

$$\zeta_j = 1.35P_{H_2}\left(\frac{300}{T}\right)^{2/3} + 0.3P_{He}\left(\frac{300}{T}\right)^{2/3} + 0.2P_{NH_3}\left(\frac{300}{T}\right)\Delta\nu_{oj}. \tag{2.30}$$

The Ben-Reuven lineshape is defined as (Ben Reuven, 1966)

$$F(\nu,\nu_o,\Delta\nu,\zeta,\delta) = \frac{2}{\pi}\left(\frac{\nu}{\nu_o}\right)^2 \frac{(\Delta\nu-\zeta)\nu^2 + (\Delta\nu+\zeta)[(\nu_o+\delta)^2 + \Delta\nu^2 - \zeta^2]}{[\nu^2 - (\nu_o+\delta)^2 - \Delta\nu^2 + \zeta^2]^2 + 4\nu^2\Delta\nu^2}. \tag{2.31}$$

The pressure shift term $\delta$= -0.45 $P_{NH_3}$ where $P_{NH_3}$ is the partial pressure of ammonia in bars (Berge and Gulkis, 1976). The new formalism is therefore a modified version of the expression for ammonia absorption in a hydrogen/helium atmosphere developed by Joiner and Steffes (1991). The new model involves multiplying the contribution to absorptivity from each line by the empirically derived correction factor and then summing these absorptivities to determine the absorption of the gas at a particular frequency. The parameters of the correction factor were made free parameters for fitting the model to laboratory measurements. A simplex fitting function was used to generate the unresolved parameters with the weighted objective function (Hoffman *et al.* 2001),

$$\chi^2 = \sum_n \frac{(\alpha_n^{meas} - \alpha_n^{calc})^2}{(\sigma_n^{meas})^2}. \tag{2.32}$$

The values $\alpha_n^{meas}$, $\alpha_n^{calc}$ and $\sigma_n^{meas}$ are the laboratory measurements, the modeled result and the laboratory measurement error respectively. Note that this model has been tailored to provide the best possible prediction of the opacity from ammonia in the hydrogen/helium atmosphere in the 7.5 to 9.2 mm wavelength range at pressures less than 2 bars, characteristic of the upper troposphere range of the outer planets. Other models (see, eg. Berge and Gulkis, 1976 or Spilker, 1990) are more accurate at longer wavelengths and higher pressures.

## 2.8 Refractivity

During a radio occultation experiment, as the signal enters the planetary atmosphere, it may be discernibly altered by refraction and absorption. The change in amplitude and frequency of the occulted signal during the experiment can be used to derive profiles of absorption of the propagation path and refractivity of the atmosphere under investigation. Temperature and pressure profiles can be inferred from the refractivity profiles, provided that the number density normalized refractivities of the individual constituents are known (Fjeldbo 1973). The refractivity is defined as (Tyler and Howard 1969)

$$N = 10^6 (n-1). \tag{2.33}$$

The refractivity is calculated from measured data using

$$N = \frac{10^6 (f_{vac} - f_{gas})}{f_{gas}}. \tag{2.34}$$

The above equation describes the measured refractivity *N*, which includes the refractivity due to ammonia, hydrogen and helium in the case of the ammonia mixture or in the case of the phosphine mixture, the measured *N* includes the refractivity of phosphine as well

as that of hydrogen and helium. In order to calculate the refractivity of the lossy gas under test, the refractivities of the hydrogen and helium have to be subtracted from the measured $N$ which we will refer to as $N_{meas}$. The refractivity for a specific constituent, $N' = N\text{RT(K)/P(atm)}$ where $N'$ is the normalized refractivity for that constituent in $N$-units/molecule/cm$^3$, T is the temperature in Kelvin, P is the partial pressure in atmospheres and R = 1.362344x10$^{-22}$ (atm*cm$^3$)/(molecule*K).

$$N_{meas} = \frac{N'_{PH_3,NH_3} P_{PH_3,NH_3}(atm)}{RT(K)} + \frac{N'_{H_2} P_{H_2}(atm)}{RT(K)} + \frac{N'_{He} P_{He}(atm)}{RT(K)} \qquad (2.35)$$

(Kolodner and Steffes 1998). In this equation, each molecular species contributes independently to the refraction of the mixture being measured.

The normalized refractivities $N'$ of $H_2$ and He used in the calculations are (Essen 1953)

$N'_{H_2} = 5.06\times10^{-18} \pm 1.49\times10^{-21}$ N-units cm$^3$ molecule$^{-1}$ and

$N'_{He} = 1.30\times10^{-18} \pm 1.12\times10^{-21}$ N-units cm$^3$ molecule$^{-1}$.

These are substituted into equation 2.35 and the normalized refractivity for the lossy gas under test is computed.

To calculate the uncertainty in refractivity, maximum and minimum values of refractivity were evaluated. Uncertainties in $f_{vac}$ and $f_{gas}$ were obtained from the data acquired by the personal computer from the spectrum analyzer via a GPIB interface (DeBoer and Steffes 1996) as well as from systematic errors calculated by equation 2.16. Maximum and minimum values of temperature, pressure and mixing ratio were computed as described in section 2.5. Maximum values of $f_{vac}$ and temperature, as well as minimum values of $f_{gas}$, mixing ratio, pressure and refractivities of hydrogen and helium were inserted into equation 2.35 to estimate the maximum change in refractivity due to

all the contributing uncertainties. The minimum change in refractivity due to all uncertainties was determined by substituting into equation 2.35, minimum values of $f_{vac}$ and temperature as well as maximum values of $f_{gas}$, mixing ratio, pressure and refractivities of hydrogen and helium. The uncertainty in refractivity is half the difference between the maximum and minimum changes in refractivity. The results of these calculations are shown in Tables 2.1 to 2.7.

## 2.9 Profiling Phosphine at Saturn

Figure 6 shows the predicted 9.3 mm (32 GHz) vertical opacity profile of a Saturn atmosphere dominated by the saturation abundance of ammonia and by phosphine. At high altitude, the absorption is dominated by phosphine. In order to compute the profile, a deep atmosphere abundance of 468 ppm (2.5x solar) of ammonia and 30.8 ppm (1x solar) of hydrogen sulfide is assumed. The deep abundance of ammonia is first depleted by the formation of an ammonium hydrogen sulfide cloud, and then the remaining ammonia above the cloud (437.2 ppm) condenses to further deplete in the upper atmosphere. For our calculation, the solar abundances of ammonia, methane and phosphine are $1.873\times10^{-4}$, $6.043\times10^{-4}$ and $0.622\times10^{-6}$ respectively. These were derived by Hoffman (2001) from data in Anders and Grevesse (1989). The temperature and pressure profile used to calculate the saturation vapor pressure and absorption due to ammonia was taken from Lindal *et al.* (1985). For pressures of 1.3 bars and above, the temperature pressure profile was calculated using the thermochemical model described in Briggs and Sackett (1989). A drop in the mixing ratio of phosphine at pressures less than 0.7 bars following that of the Orton *et al.* (2000) detections is also assumed. As reported

in Orton *et al.* (2001) the phosphine mixing ratio at 645 mbar of $7.4\times10^{-6}$ drops linearly in log (pressure) versus log (mixing ratio) to a value at 150 mbar of $4.3\times10^{-7}$, thus deep mixing ratios of 10x and 20x solar $PH_3$ were used to plot Figure 2.11. Thus the Cassini Ka-band (32 GHz or 9.3 mm) downlink will likely encounter measurable absorption from phosphine at the 0.5 bar pressure level and will be capable of profiling phosphine down to altitudes with pressures up to 0.8 bars, where the opacity of ammonia would then dominate followed by loss of signal (LOS) at about 0.9 bars. Thus it will be possible to profile the abundance of phosphine in the 0.5-0.8 bar pressure range of the Saturn atmosphere using the Cassini radio occultation experiment at Ka-band. See Chapter 4 (sections 4.2 – 4.7) for a more complete discussion of the effects of phosphine and ammonia on the Cassini radio occultation experiment.

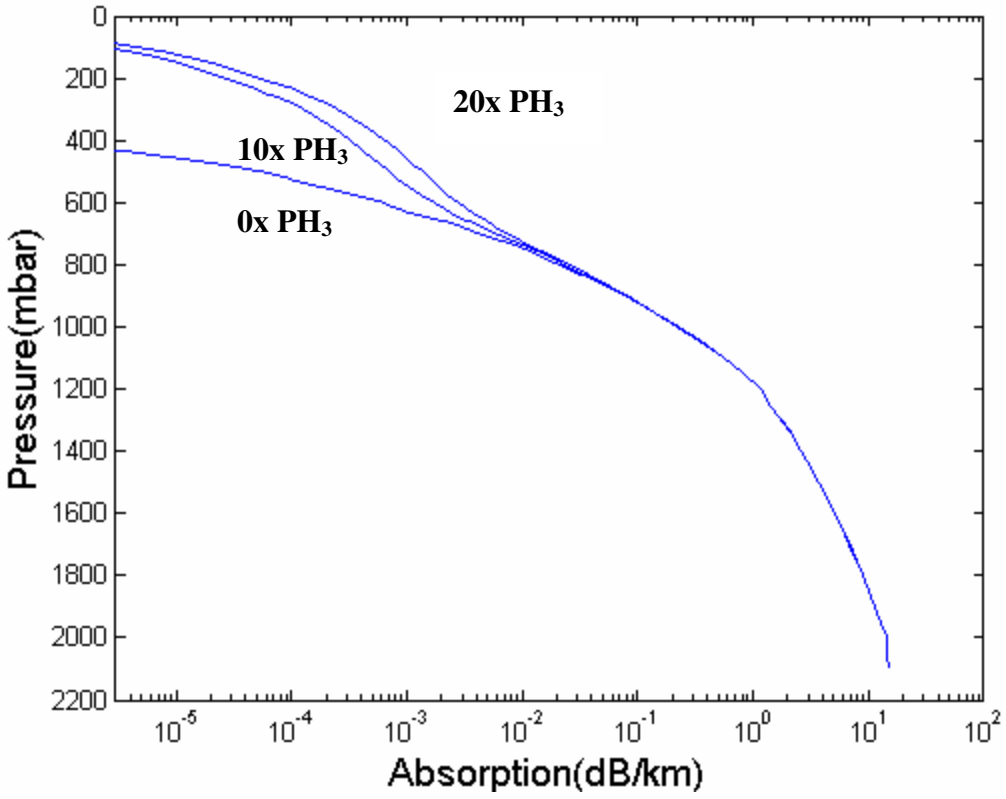


Figure 2.11: Predicted 9.3 mm (32 GHz) vertical opacity profile of the Saturn atmosphere dominated by a saturation abundance of ammonia and phosphine. The vertical mixing ratio profile of phosphine follows that of the Orton *et al.* (2000) detections with deep mixing ratios of 0, 10 and 20x solar.

# CHAPTER 3

# LABORATORY MEASUREMENTS OF PHOSPHINE AND AMMONIA AT W-BAND UNDER OUTER PLANET CONDITIONS

While *in situ* measurements of atmospheric structure and composition (such as would be measured using an entry probe) have the distinct advantage of providing high temporal and spatial resolution, radio observations at earth facilities can be used to provide a more global coverage of the planet. Radio emission from a planet's atmosphere is sensitive to microwave absorbing constituents present; thus in order to accurately interpret radio emission spectra precise knowledge about the absorbing constituents is necessary.

## 3.1 Motivation for W-band Laboratory Measurements

The centimeter-wave laboratory results for the opacity of phosphine presented in Hoffman *et al.* (2001) included the development of a new formalism to predict the opacity of phosphine ($PH_3$) in a hydrogen/helium ($H_2$/He) atmosphere. Laboratory results in the 7.5 – 9.2 mm wavelength range (Mohammed and Steffes, 2003) described in Chapter 2 indicate that the formalism is also accurate in that wavelength range. Use of the new phosphine formalism in radiative transfer models for Saturn provided a better match to measured centimeter-wavelength emission spectra than previous models (Hoffman *et al.* 2001). Since phosphine also affects the emission spectra of the outer planets at shorter millimeter wavelengths, new laboratory measurements of the refraction and absorption of phosphine in a hydrogen/helium atmosphere were conducted at 3.2 mm (94 GHz) to verify the accuracy of the Hoffman *et al.* formalism.

The 3-mm wavelength has been used extensively for disk-averaged emission measurements of the outer planets (see eg. Griffin and Orton 1993, Muhleman and Berge 1991, Griffin *et al.* 1986). Also, this wavelength has been recently used for interferometric mapping of Saturn using the Berkeley-Illinois-Maryland Association (BIMA) array (van de Tak *et. al* 1999). Laboratory measurements of phosphine at this wavelength will also influence interpretation of possible future emission spectra of the outer planets taken with the new NRAO 100-meter antenna known as the Green Bank Telescope. Future high resolution maps derived from arrays such as CARMA (Combined ARay for Millimeter-Wavelength Astronomy) or the NRAO/ALMA (Altacama Large Millimeter Array) could be interpreted using the laboratory measurements of phosphine's opacity at this wavelength.

The W-band (3.2 mm) system used to measure the refractivity and opacity of phosphine is similar to that used by Joiner and Steffes (1991) to measure the opacity and refractivity of ammonia under Jovian conditions, but it is more sensitive than that system by nearly a factor of 8. The accuracy of the results was improved with the use of a computer-based acquisition and analysis system, and the use of microwave instruments which are of higher precision than those used by Joiner and Steffes (1991).

Mohammed and Steffes (2003, and Chapter 2 of this document) measured the opacity and refractivity of ammonia in a hydrogen/helium atmosphere in the 7.5 to 9.2 mm range. These results gave rise to a revised opacity model using a corrected Ben-Reuven lineshape, but the new model is only valid in the 32 to 43 GHz range. Thus additional laboratory absorption and refractivity measurements at 94 GHz (3.2 mm) of gaseous ammonia in a hydrogen/helium atmosphere have been conducted in order to

better evaluate the models for ammonia absorption at millimeter wavelengths. Results of measurements of both phosphine and ammonia can be used to better interpret maps of Saturn's emission at this wavelength which could potentially deduce spatial variations in the abundances of both gases in the atmosphere of Saturn.

## 3.2 Laboratory Configuration

A block diagram of the W-band atmospheric simulator is shown in Figure 3.1. The laboratory measurements at 94 GHz (3.2 mm) were conducted in a similar fashion to the measurements taken in the Ka-band region of 32 to 40 GHz (7.5 to 9.2 mm) using the same gas-handling and temperature subsystems (see Chapter 2, section 2.3). The electrical subsystem consists of the W-band millimeter-wave sweep oscillator which is a Gunn diode oscillator with a modulated input. By adjusting the bias voltage, the Gunn diode oscillator was made to sweep using a noisy power source. The Gunn diode oscillator was made to generate a broadband output by reducing the bias voltage to 2.2 volts, where the maximum bias voltage is 3.5 volts. The output of the swept source is shown in Figure 3.2. The millimeter-wave oscillator sweeps over the entire frequency range of the 94 GHz resonance of the W-band Fabry-Perot resonator, even when shifted by the refractive gases being measured.

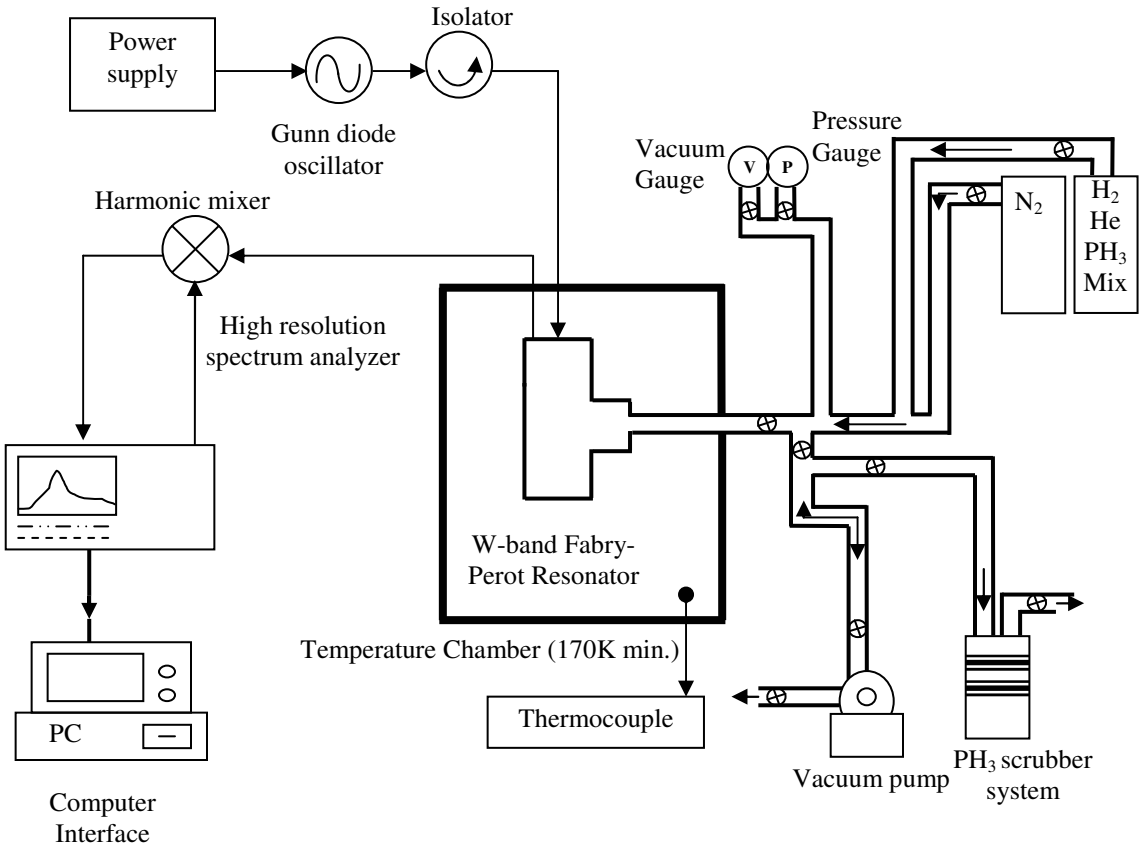


Figure 3.1: Block diagram of W-band atmospheric simulator

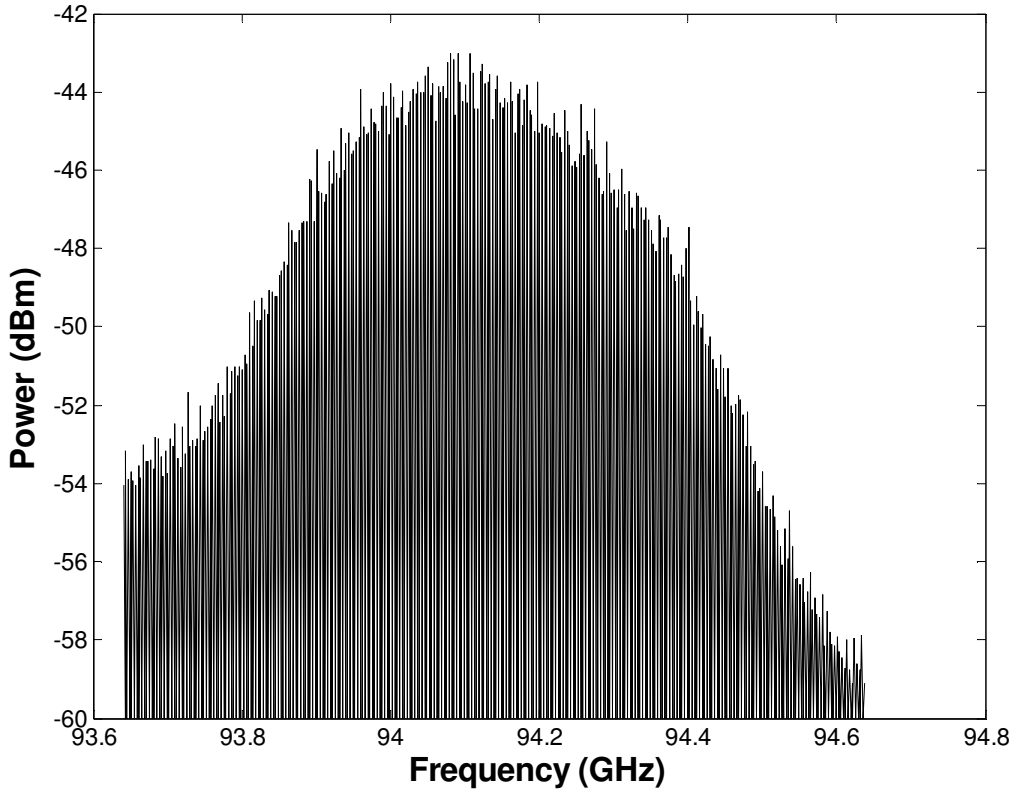


Figure 3.2: Output of the Gunn diode oscillator with a bias voltage of 2.2 V measured with a spectrum analyzer resolution bandwidth of 1 MHz.

The resonator, enclosed in a T-shaped Pyrex glass envelope of side wall thickness 7.9 mm, is then placed in an ultra-low temperature freezer capable of cooling to a temperature of 173 K. Rigid pieces of WR-10 waveguide connect the resonator to the millimeter wave source outside the temperature chamber and to a harmonic mixer which is attached to the computer controlled HP-8564E spectrum analyzer. The same computer system and software is used as that described in DeBoer and Steffes (1996). The J-type thermocouple monitors the inside of the temperature chamber and an alcohol thermometer measures the ambient temperature. Precautions taken when handling the phosphine mixture include the use of gas masks and a phosphine leak detector sensitive

to abundances as low as 5 parts per billion. When handling ammonia, a hydrogen leak detector is used in addition to gas masks. The scrubber shown in Figure 3.1 effectively removes the phosphine or ammonia from the mixture allowing only hydrogen and helium to be vented into the local environment.

The W-band Fabry-Perot resonator shown in Figures 3.3 and 3.4 consists of two gold-plated mirrors, one flat and the other spherical, which act as a band-pass filter at the resonant frequency of 94 GHz (3.2 mm). Electromagnetic energy is coupled to and from the resonator via the twin irises situated on the flat mirror. The flat mirror of diameter 5 cm and the curved mirror of diameter of 11.5 cm are separated by a distance of about 15 cm. The quality factor of this resonator is on the order of 35, 000.

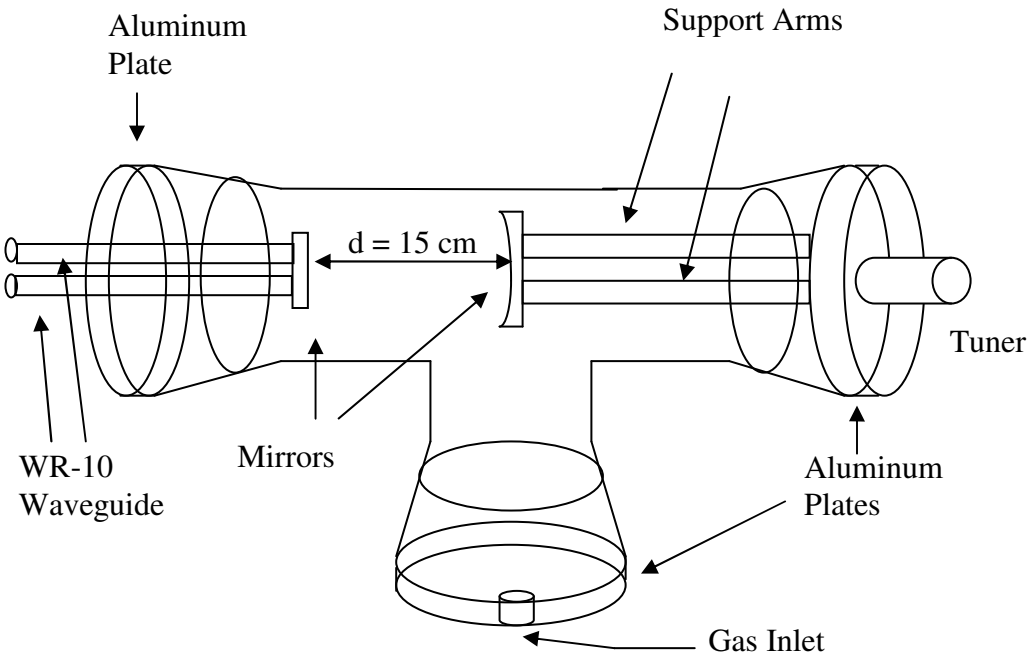


Figure 3.3: W-band Fabry-Perot resonator

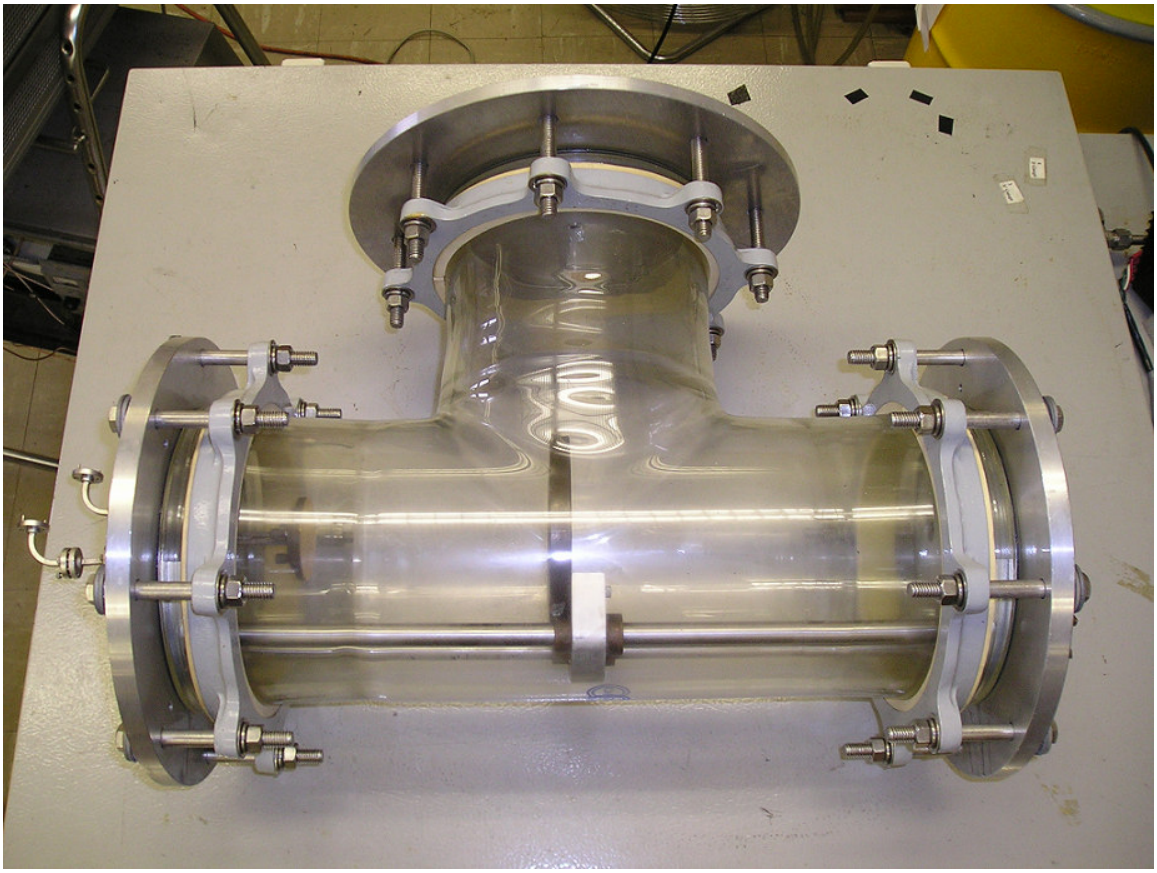

Figure 3.4: Picture of W-band Fabry-Perot resonator

### 3.3 Results

Measurements of the opacity and refractivity of a phosphine mixture were conducted at 3.2 mm (94 GHz) at pressures of 0.5, 1 and 2 bars and at temperatures of 293 K and 213 K. The gas mixture consisted of 82.6 % hydrogen ($H_2$), 9.2 % helium (He) and 8.2 % phosphine. Additionally, new high-precision laboratory measurements of the opacity and refractivity of ammonia in a hydrogen/helium atmosphere were completed at pressures of 0.5, 1 and 2 bars and at temperatures of 204 K, 211 K and 290 K. The gaseous ammonia mixture consisted of 92.338 % hydrogen ($H_2$), 5.630 % helium (He) and 2.032 %

ammonia ($NH_3$). All laboratory results are shown in Tables 3.1 and 3.2. The error bars were computed as per the process described in the previous Chapter (section 2.5).

Figures 3.5 and 3.6 display the results of the measurements of the phosphine mixture compared with the opacity predicted by the Hoffman *et al.* model (2001). The two data points at each pressure represent independent experiments. The phosphine model which is based on the Van Vleck-Weisskopf lineshape, was developed for the centimeter-wavelength opacity of $PH_3$, and utilizes line intensities from the JPL (Pickett *et al.* 1998) catalog which have been selectively weighted to fit the centimeter wavelength laboratory data. The laboratory measurements conducted indicate the model is accurate at 94 GHz (3.2 mm) under conditions for the outer planets; thus no changes to the model are necessary.

The results of the measurements of the ammonia mixture are compared to various models and are shown in Figures 3.7, 3.8 and 3.9. The laboratory results are compared to models from Joiner and Steffes (1991), Berge and Gulkis (1976) as well as Spilker (1990) for opacity from ammonia which is pressure broadened by hydrogen and helium. Note that the Spilker model only gave physical results for some of the experimental conditions. At pressures of about 1 bar or lower, the predicted opacity by the Berge and Gulkis and the Joiner/Steffes models are within the error bars of the data, but at higher pressures of about 2 bars, the measured opacity is higher than that predicted by either model. This is likely due to the contribution from the pressure broadened submillimeter lines becoming more significant at 94 GHz (3.2 mm). The absorption computed by the Spilker model is slightly lower than the measured points at 290 K at a pressure of 2 bars, but, at a lower temperature of 204 K and a pressure of 2 bars, it predicts opacity that is

significantly less than any of the others shown, and at a temperature of 211 K and pressures of 0.5 and 1 bar, the model generates negative opacity which is not physical. Both the Spilker (1990) and the Berge and Gulkis (1976) models take into account the effects of only the inversion lines, whereas the Joiner and Steffes (1991) model includes the effects of the inversion lines in addition to a few submillimeter lines. We have attempted to fit the data from this work to generate a new formalism in order to predict the opacity of ammonia in a hydrogen/helium atmosphere at 94 GHz (3.2 mm). Since measurements were conducted at one frequency, but at different temperatures and pressures, this model can only reliably be used to describe the opacity of ammonia under Jovian conditions at that frequency (wavelength).

Table 3.1: Results of phosphine opacity measurements at 293 K and 212 K. Gas mixture composition: 82.6 % $H_2$, 9.2 % He, 8.2 % $PH_3$

| Date | Pressure (bars) | Frequency (GHz) | Hoffman Model (dB/km) | Opacity: Measured (dB/km) | Measurement $\sigma\pm$ (dB/km) | Normalized Refractivity (N-units $cm^3$ $mol^{-1}$)$\times 10^{17}$ |
|---|---|---|---|---|---|---|
| 06/05/2003 | 0.987 | 94.34 | 2.2906 | 3.1789 | 2.5515 | 7.41923±0.47936 |
| T = 293 K | 1.971 | 94.31 | 9.1307 | 10.7345 | 2.6535 | 7.94645±0.42829 |
| 06/06/2003 | 0.499 | 94.35 | 0.5855 | 0.1378 | 4.2789 | 8.28516±0.73169 |
| T = 293 K | 1.004 | 94.33 | 2.3702 | 0.4394 | 4.1915 | 8.50395±0.49705 |
| | 1.971 | 94.31 | 9.1307 | 8.3848 | 4.2574 | 8.26488±0.41994 |
| 08/06/2003 | 0.509 | 94.17 | 1.5536 | -5.3021 | 4.8884 | 5.98600±0.63996 |
| T = 213 K | 0.968 | 94.15 | 5.6180 | 1.9888 | 5.1129 | 5.93413±0.38004 |
| 08/07/2003 | 0.495 | 94.17 | 1.4897 | -1.4343 | 2.8678 | 6.15370±0.70842 |
| T = 212 K | 0.983 | 94.16 | 5.8736 | 5.4330 | 2.9756 | 6.17236±0.51139 |

Table 3.2: Results of ammonia opacity measurements at 290 K, 211 K and 204 K. Gas mixture composition: 92.338 % $H_2$, 5.63 % He, 2.032 % $NH_3$

| Date | Pressure (bars) | Frequency (GHz) | New Model (dB/km) | Opacity: Measured (dB/km) | Measurement $\sigma\pm$ (dB/km) | Normalized Refractivity (N-units $cm^3$ $mol^{-1}$)$\times 10^{17}$ |
|---|---|---|---|---|---|---|
| 08/19/2003 | 1.001 | 94.10 | 4.8119 | 3.8477 | 3.2990 | 26.8368±1.8973 |
| T = 290 K | 1.992 | 94.08 | 18.9386 | 23.8100 | 3.8684 | 24.6859±1.5083 |
| 08/20/2003 | 0.989 | 94.10 | 4.6974 | 4.1046 | 3.7056 | 26.8183±1.8235 |
| T = 290 K | 1.999 | 94.08 | 19.0708 | 23.9563 | 4.3983 | 24.6200±1.4936 |
| 08/12/2003 | 0.517 | 94.17 | 3.3116 | 4.3919 | 3.5326 | 16.1156±2.3365 |
| T = 211 K | 0.984 | 94.16 | 11.9694 | 10.3535 | 3.8955 | 15.9465±1.6415 |
| 08/13/2003 | 0.512 | 94.17 | 3.2480 | 2.1168 | 3.3011 | 15.6136±3.7291 |
| T = 211 K | 0.981 | 94.16 | 11.8967 | 8.9548 | 3.6735 | 16.0680±1.7265 |
| 08/27/2003 T = 204 K | 1.950 | 94.16 | 51.5639 | 47.3783 | 6.0422 | 15.0530±1.4677 |
| 08/28/2003 T = 203 K | 1.978 | 94.16 | 53.8268 | 53.4411 | 6.1605 | 14.7806±1.4401 |

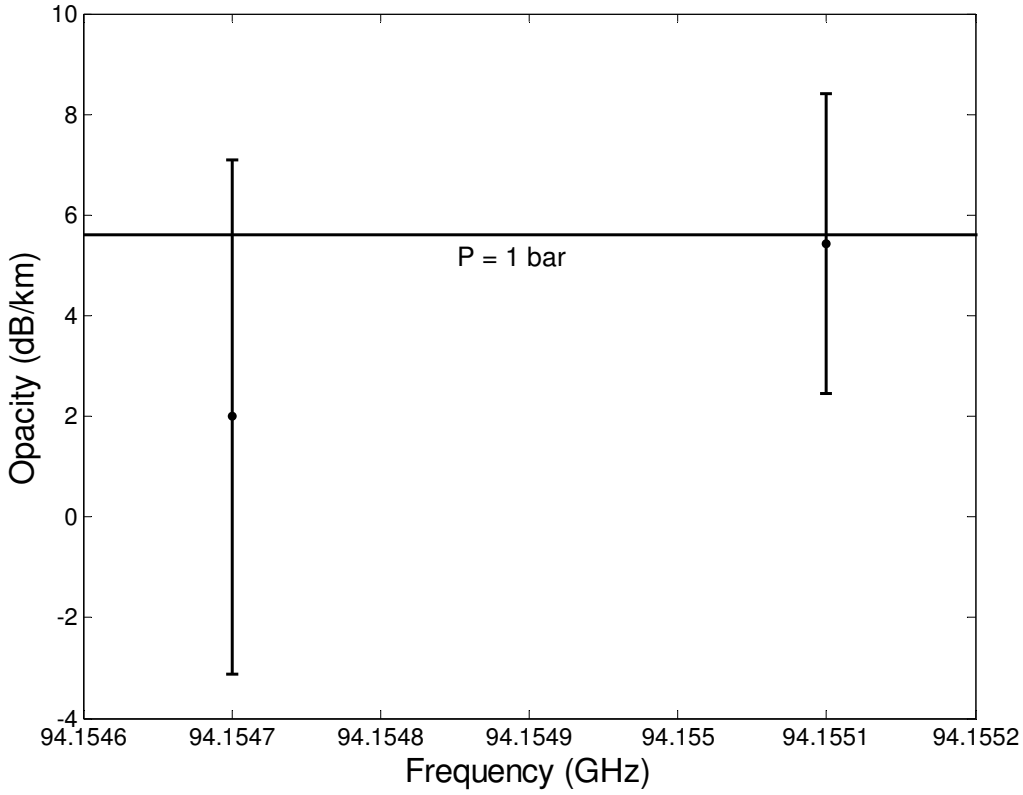


Figure 3.5: August 6, 7, 2003 laboratory measurements compared to the Hoffman *et al.* (2001) formalism for phosphine absorption. Measurements were taken at a temperature of 213 K and a pressure of about 1 bar with a mixing ratio of 82.6 % $H_2$, 9.2 % He, 8.2 % $PH_3$.

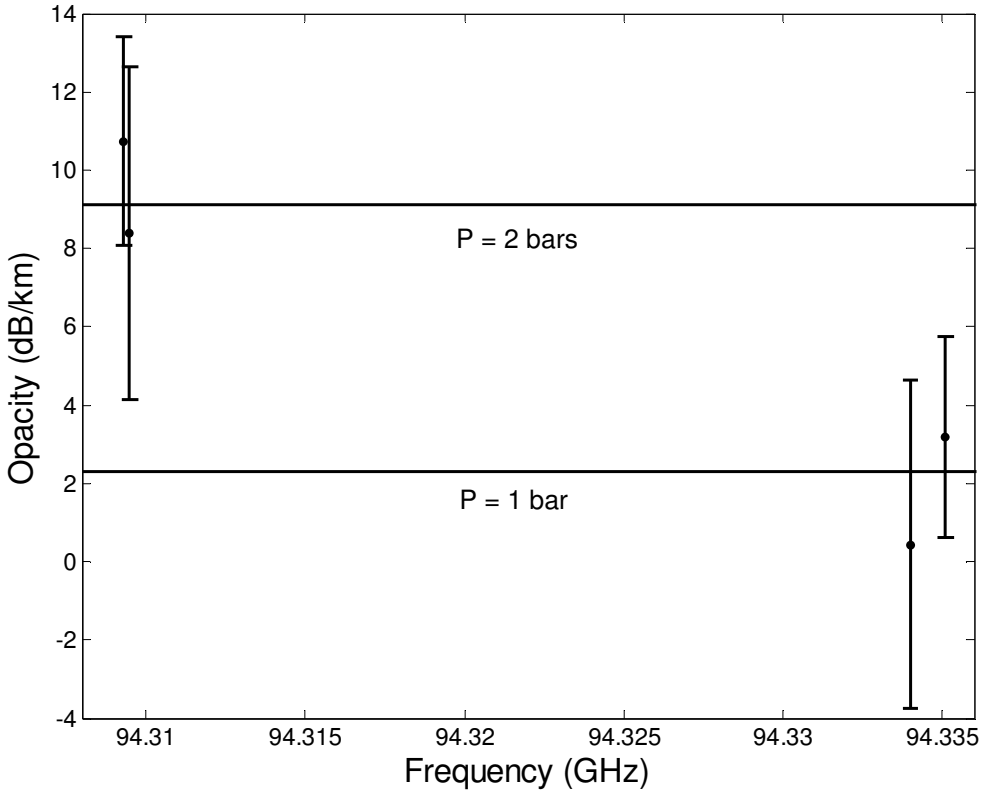


Figure 3.6: June 5, 6, 2003 laboratory measurements compared to the Hoffman *et al.* (2001) formalism for phosphine absorption. Measurements were taken at a temperature of 293 K and pressures of about 1 and 2 bars with a mixing ratio of 82.6 % $H_2$, 9.2 % He, 8.2 % $PH_3$.

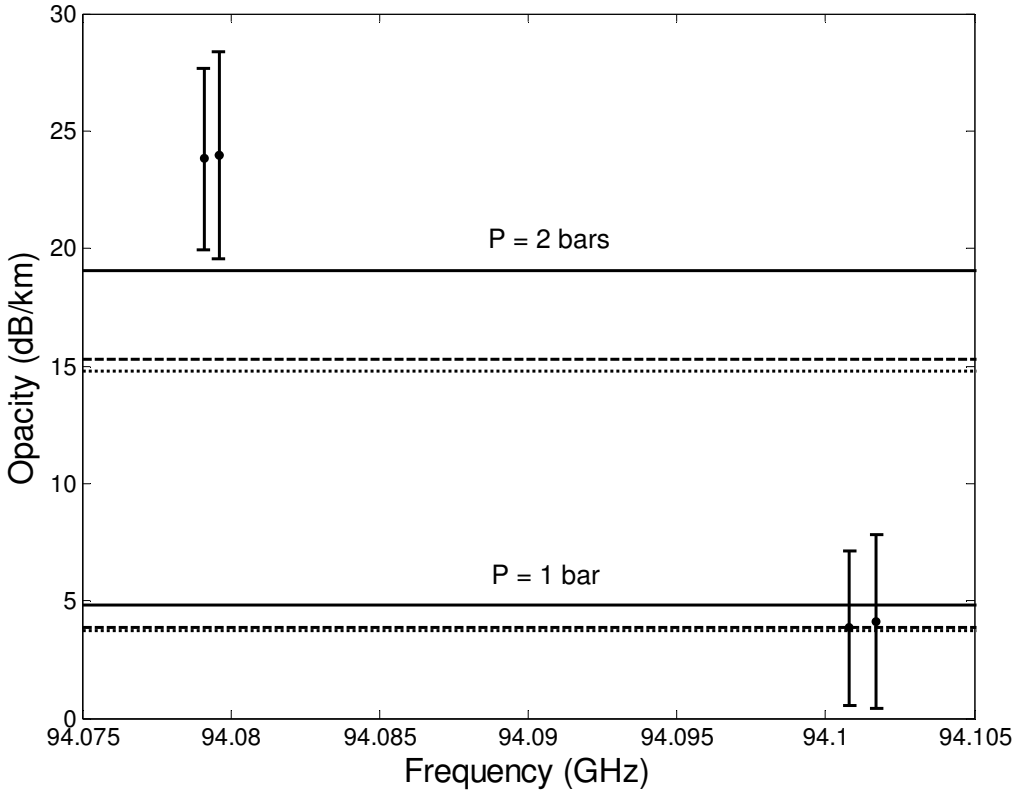


Figure 3.7: August 19, 20, 2003 laboratory measurements compared to various formalisms for ammonia absorption. The solid line is the new model, the dotted-dashed line is the Spilker model (in this figure the Spilker model, computed only at 2 bars, and the new model overlap), the dashed line is the Joiner/Steffes model and the dotted line is the Berge and Gulkis model. At P = 1 bar, the Joiner/Steffes and the Berge and Gulkis models nearly overlap. Measurements were taken at a temperature of 290 K and pressures of about 1 and 2 bars with a mixing ratio of 92.338 % $H_2$, 5.630 % He, 2.032 % $NH_3$.

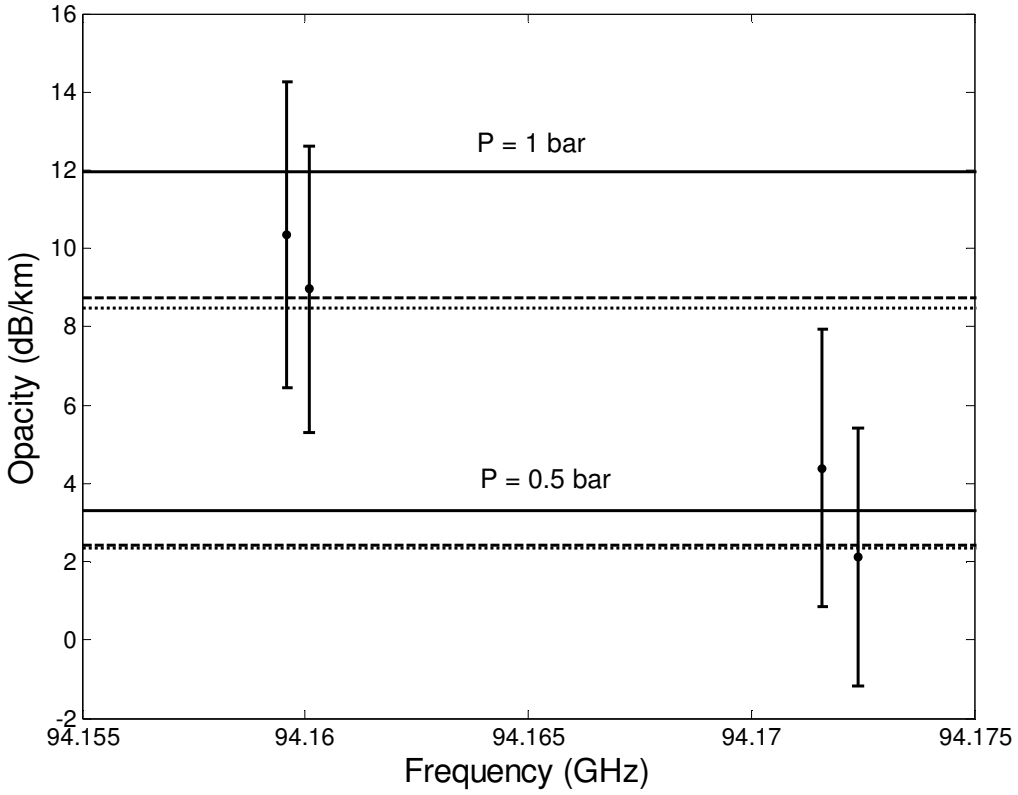


Figure 3.8: August 12, 13, 2003 laboratory measurements compared to various formalisms for ammonia absorption. The solid line is the new model, the dashed line is the Joiner/Steffes model and the dotted line is the Berge and Gulkis model. At P = 0.5 bar, the Joiner/Steffes and the Berge and Gulkis models nearly overlap. Measurements were taken at a temperature of 211 K and pressures of about 0.5 and 1 bar with a mixing ratio of 92.338 % $H_2$, 5.630 % He, 2.032 % $NH_3$.

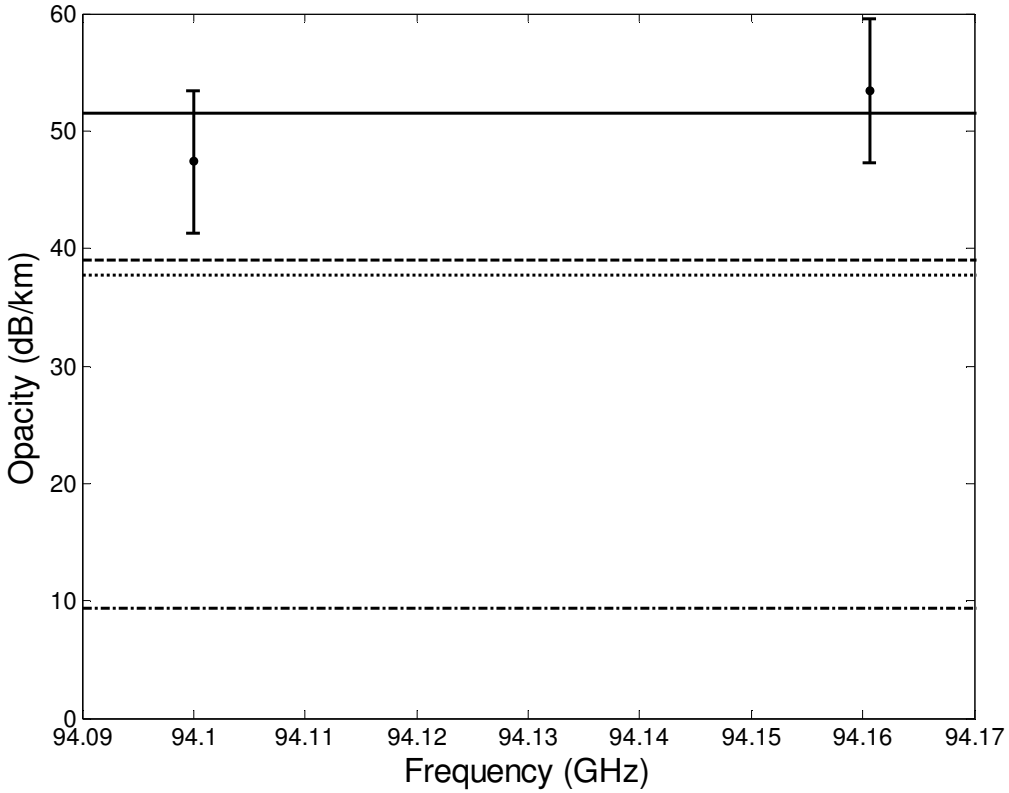


Figure 3.9: August 27, 28, 2003 laboratory measurements compared to various formalisms for ammonia absorption. The solid line is the new model, the dotted-dashed line is the Spilker model, the dashed line is the Joiner/Steffes model and the dotted line is the Berge and Gulkis model. Measurements were taken at a temperature of 204 K and a pressure of about 2 bars with a mixing ratio of 92.338 % $H_2$, 5.630 % He, 2.032 % $NH_3$. The data points have been spread about 94 GHz for clarity.

### 3.4 Formalism for Ammonia Millimeter-Wavelength Opacity

A new formalism for predicting the opacity of ammonia in a hydrogen/helium atmosphere at 94 GHz (3.2 mm) uses the Ben Reuven lineshape for the inversion lines (as per Berge and Gulkis, 1976) and the Kinetic lineshape for the rotational lines. The equation for the absorption of a gas that has been pressure broadened by foreign gases is defined as

$$\alpha = C\left(\sum A_j \pi \Delta\nu_j F_j(\nu, \nu_{oj}, ...)\right) \text{ cm}^{-1} \tag{3.1}$$

where the individual line number is *j*; $A_j$, is the absorption at the line center, $\Delta\nu_j$ is the linewidth, $F_j$ is the lineshape function and C is an empirical correction factor, used in some models. The absorption at the line center is calculated using the equation

$$A_j = \frac{nS_j(T)}{\pi\Delta\nu_j} \text{ cm}^{-1} \tag{3.2}$$

where *n* is the number density, $S_j(T)$ is the intensity of the line *j*, which is scaled from the intensity calculated at the reference temperature $T_o$ (Pickett *et al.* 1998). The resulting expression for the line center absorption is

$$A_j = \frac{10^6 P(bar)}{\pi k_B T \Delta\nu_j (cm^{-1})}\left(\frac{T_o}{T}\right)^{\eta+1} S_j(T_o) e^{-(hc/k)E_{lj}(1/T - 1/T_o)} \text{ cm}^{-1} \tag{3.3}$$

The $E_{lj}$ term is the lower state energy at each line which is obtained from the the Poynter/Pickett catalog (Pickett *et al.* 1998) and $\eta$, the temperature dependence term is 1.5 for symmetric-top molecules such as phosphine and ammonia. For inversion lines (20-27 GHz), the linewidth for the gaseous mixture is found using (Berge and Gulkis, 1976)

$$\Delta\nu_j = 2.318 P_{H_2}\left(\frac{300}{T}\right)^{2/3} + 0.79 P_{He}\left(\frac{300}{T}\right)^{2/3} + 0.75 P_{NH_3}\left(\frac{300}{T}\right)\Delta\nu_{oj} \tag{3.4}$$

where the line self broadening parameters $\Delta\nu_{oj}$ are from Poynter and Kakar (1975) and the partial pressures are in units of bars. The Ben-Reuven lineshape also uses a coupling element term given by (Berge and Gulkis, 1976)

$$\zeta_j = 1.92 P_{H_2}\left(\frac{300}{T}\right)^{2/3} + 0.3 P_{He}\left(\frac{300}{T}\right)^{2/3} + 0.49 P_{NH_3}\left(\frac{300}{T}\right)\Delta\nu_{oj}. \tag{3.5}$$

The Ben-Reuven lineshape is defined as (Ben Reuven, 1966)

$$F(\nu,\nu_o,\Delta\nu,\zeta,\delta) = \frac{2}{\pi}\left(\frac{\nu}{\nu_o}\right)^2 \frac{(\Delta\nu-\zeta)\nu^2 + (\Delta\nu+\zeta)[(\nu_o+\delta)^2 + \Delta\nu^2 - \zeta^2]}{[\nu^2 - (\nu_o+\delta)^2 - \Delta\nu^2 + \zeta^2]^2 + 4\nu^2\Delta\nu^2} \tag{3.6}$$

and a correction factor is used where

$$C = 1.0075 + 0.0304\left(\frac{P_{H_2}}{T}\right) + 0.0537\left(\frac{P_{H_2}}{T}\right)^2. \tag{3.7}$$

The pressure shift term $\delta$ = -0.45 $P_{NH_3}$ where $P_{NH_3}$ is the partial pressure of ammonia in bars (Berge and Gulkis, 1976). The above equations describe the opacity due to the ammonia inversion lines. As per Joiner and Steffes (1991), the absorption from the pressure-broadened submillimeter rotational lines of ammonia is expressed by equation 3.1 with the use of a kinetic lineshape also known as the Gross lineshape which is expressed by (Gross, 1955)

$$F(\nu,\nu_o,\Delta\nu) = \left(\frac{\nu}{\nu_o}\right)\frac{4\nu\nu_o\Delta\nu}{(\nu_o{}^2 - \nu^2)^2 + 4\nu^2\Delta\nu^2}. \tag{3.8}$$

The Ben-Reuven lineshape reduces to the kinetic lineshape when $\Delta\nu = \varsigma$ and $\delta = 0$.

For the submillimeter lines, $C$ = 1, and the linewidth (in GHz) for the first rotational line at 572 GHz which best matches our data is given by

$$\Delta\nu = 123.3551 P_{H_2}\left(\frac{300}{T}\right)^{0.3} + 60.7441 P_{He}\left(\frac{300}{T}\right)^{0.3} + 154.1939 P_{NH_3}\left(\frac{300}{T}\right). \quad (3.9)$$

Since the pressure broadened coefficients have not been measured for this line, these coefficients were empirically derived. The line broadening parameters for the first rotational line in equation 3.9 were set as free parameters for fitting the model to laboratory measurements. As in section 2.6, a simplex fitting function was used to generate the unresolved parameters with the weighted objective function (Hoffman *et al.* 2001),

$$\chi^2 = \sum_n \frac{(\alpha_n^{meas} - \alpha_n^{calc})^2}{(\sigma_n^{meas})^2}. \quad (3.10)$$

The values $\alpha_n^{meas}$, $\alpha_n^{calc}$ and $\sigma_n^{meas}$ are the laboratory measurements, the modeled result (which includes the absorption due to the inversion as well as the rotational lines) and the laboratory measurement error, respectively. Using phosphine as a chemical analog, we fit the data with the ratio of the pressure broadening parameters in equation 3.9 being similar to that of the pressure broadening reported for the first rotational transition of phosphine in Pickett *et al.* (1981). The intensities of the rotational lines, obtained from the Poynter/Pickett catalog (Pickett *et al.* 1998) are assumed to be correct, thus the empirical terms chosen were the line broadening parameters.

For the remaining 255 rotational lines, the linewidth (in GHz) is estimated by

$$\Delta\nu_j = 2.885 P_{H_2}\left(\frac{300}{T}\right)^{0.3} + 1.000 P_{He}\left(\frac{300}{T}\right)^{0.3} + 22.989 P_{NH_3}\left(\frac{300}{T}\right). \quad (3.11)$$

The hydrogen and self broadening parameters used in equation 3.11 approximate the values measured by Brown and Peterson (1994). The helium broadening parameter was set to 1 GHz/bar so that the hydrogen/helium broadening ratio is similar to that of the far-

infrared lines reported in Pine *et al.* (1993). The new formalism is therefore simply the expression for ammonia absorption in a hydrogen/helium atmosphere developed by Berge and Gulkis (1976) with an addition of the effects of the rotational lines. For the new model presented in this paper, the Berge and Gulkis model (1976) was chosen to represent the absorption due to the inversion lines since this model gives the highest opacity for the inversion lines under experimental conditions.

In equations 3.9 and 3.11, the temperature exponent for hydrogen and helium falls below the theoretical limit. As per Townes and Schawlow (1955) the linewidth is related to temperature by

$$\Delta\nu \propto T^{-(m+1)/2(m-1)} = T^{-\xi} \tag{3.12}$$

where $1 < m < \infty$ and $0.5 < \xi < 1$ since $m = 3$ is the lower limit for a neutral gas. For ammonia $m = 3$ yielding $\xi = 1$. While this is an idealization, experimental data from various other constituents have shown that lower values are possible (see e.g. Varanasi *et al.* 1994).

### 3.5 Millimeter-Wave Spectrum of the Outer Planets

Understanding the millimeter wave spectrum of the outer planets is vital since millimeter waves can uniquely probe the middle and deep atmospheres (p ~ 1 bar) of the gaseous giants (Orton *et al.*, 1986). At pressures up to 1 bar, the laboratory data indicate that the 3.2 mm ammonia spectrum is dominated by its inversion lines and is well characterized by the Joiner/Steffes model (1991) or the Berge and Gulkis model (1976). At pressures greater than 1 bar, characteristic of the deep layers of the atmospheres, the rotational lines of ammonia also contribute significantly to the opacity. Since existing models appear to

understate the contribution from rotational lines, use of the new model described above can have considerable impact on the interpretation of radio astronomical data at wavelengths less than of 6 mm for Jupiter, 6.5 mm for Saturn, 10.7 mm for Uranus and 8.8 mm for Neptune. Since measurements of phosphine at 94 GHz (3.2 mm) agreed with the predicted opacity by the Hoffman *et al.* (2001) model for phosphine absorption, this model appears valid at all millimeter and centimeter wavelengths under conditions of the outer planets.

# CHAPTER 4

## THE RADIO OCCULTATION TECHNIQUE FOR STUDYING ATMOSPHERES OF OBLATE PLANETS

As planetary space probes have evolved, the radio occultation experiment has become a principal tool for remote sensing of planetary atmospheric structure and composition. The experiment occurs when the earth is occulted by the planet's atmosphere as viewed from the spacecraft. This means that when the space probe moves behind the planet, the probe's radio signal propagation path connecting the probe with the earth passes through consecutively lower portions of the planetary atmosphere (see Figure 4.1). The changes in frequency, phase and amplitude of the spacecraft's radio signal can yield estimates of refractivity, which are related to the temperature-pressure profile of the atmosphere, as well as absorptivity profiles of the neutral atmosphere. The absorptivity profiles can be used to infer abundances of microwave absorbing molecules in the upper atmosphere ($p <$ 2 bars) given their absorptive properties. This chapter includes a description of a radio occultation simulator which was developed to predict temporal absorption profiles given a nominal model of Saturn's atmosphere and using the Cassini orbital trajectories. It also incorporates the work described in Chapter 2.

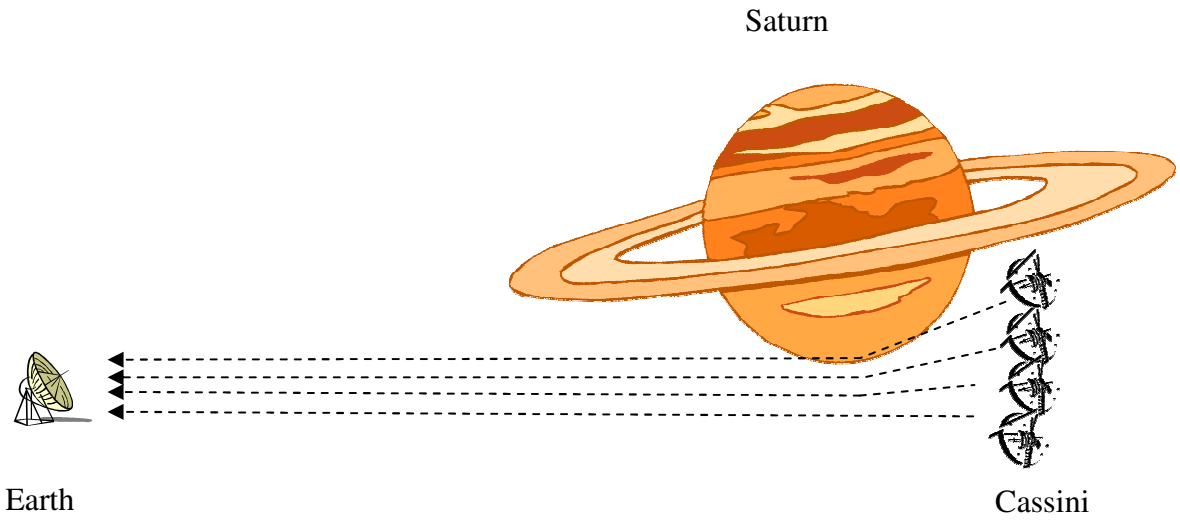


Figure 4.1: Typical profile of the Cassini radio occultation experiment

## 4.1 Retrievals Using Radio Occultation

In a radio occultation experiment, the amplitude and frequency of the spacecraft radiated signals must be stable in order to obtain accurate results from the effects of the atmosphere. To ensure stability, a reference signal can be uplinked to the spacecraft by the receiving deep space network (DSN) station. This is a two-way mode whereby the spacecraft oscillator locks to this signal and then transmits two frequencies that are integer ratios of the received frequency. In a one-way mode, an on-board oscillator is used to generate the downlink carrier from the spacecraft to Earth. One-way mode is more suitable for probing dense atmospheric regions which cause large refraction. The scintillation imposed on the uplink by atmospheric structure affects the spacecraft's radio transponder in such a manner that the coherence of the downlink carrier is degraded. However, two-way measurements are preferable when probing less dense atmospheres

because tracking stations can afford high stability (Fjeldbo, 1973). In the one-way mode, the stability problem can be resolved with the use of an ultra stable oscillator or USO as in the case with the Cassini mission to Saturn. Refraction in the atmosphere increases the Doppler shift due to spacecraft motion, and this also affects the uplinked reference signal from Earth. During a radio occultation experiment, the magnitudes of the Doppler shifts are substantial since the signal received on Earth includes the shifts incurred by both the uplink and downlink in the two-way mode. The Doppler shifts must be anticipated before the experiment is conducted, and they are possible to predict since the spacecraft trajectory is known and the refractivity of the planet can be estimated from models of atmospheric structure and constituents (see, e.g. Steffes *et. al* 1994). A radio occultation simulator to be used for the purpose of predicting signal frequencies and intensities will be the topic of section 4.2.

In a typical experiment, the spacecraft modulation, used for communications, is switched off and continuous wave (CW) signals are transmitted by the spacecraft during the experiment at the designated frequency. The signals are received at a 70-m-diameter or 34-m-diameter antenna at one of the three NASA Deep Space Network (DSN) facilities located at Goldstone, CA, Madrid, Spain and Tidbinbilla, Australia. As the signal enters the planet's atmosphere, the detectable change in frequency and amplitude is caused by refraction and absorption as well as some scattering from the surface of the planet or the planet's atmosphere. The frequency of the received signal experiences a Doppler shift during a radio occultation experiment due to the relative motion between the source and receiver along the actual ray path. Since the index of refraction of the atmosphere is non-unity and the path is deflected by an angle due to atmospheric

refraction, the Doppler shift differs from what would have been observed in the absence of the atmosphere. This measured deviation in frequency and phase can be used to estimate index of refraction of the atmosphere because the geometry of the estimated trajectory is known (Fjeldbo and Eshleman 1965).

As mentioned, the frequency and signal amplitude measured at the earth station can be used to find values of atmospheric refractivity and absorptivity as a function of radius or height. Jenkins *et al.* (1994) give detailed descriptions of techniques for analyzing the frequency and power time series to retrieve the necessary profiles. The geometry for the radio occultation experiment is displayed in Figure 4.2 from Steffes *et. al* (1994). The received frequency, $f_r(t)$ as well as the positions and velocities of the spacecraft and the ground station relative to the planet can be used to find the bending angle, $\delta(t)$ and the ray impact parameter, $a(t)$.

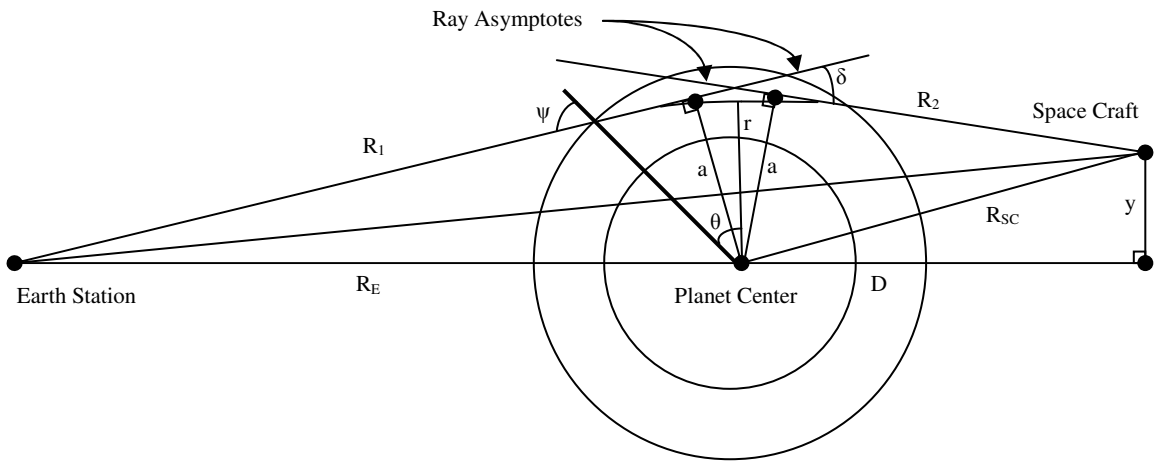


Figure 4.2: Geometry for one leg of the radio occultation experiment (spherical planet)

The index of refraction $n(a)$ can in turn be found by applying the following Abel-type transform to the ray path parameters

$$\log_e(n(r)) = \frac{1}{\pi}\int_a^{\infty} \frac{\delta(x)dx}{\sqrt{x^2 - a^2}} \tag{4.1}$$

where $r$ is the radius of closest approach. The relationship between the index of refraction, $n$, and the impact parameter $a$ is defined as (Fjeldbo *et. al* 1971)

$$nr = a \tag{4.2}$$

where $a$ and $r$ are shown in Figure 4.2.

Density, $\rho(r)$, is related to refractivity, thus assuming an atmosphere in hydrostatic equilibrium, pressure and temperature profiles can be obtained from the following (Jenkins *et. al*, 1994)

$$P(r) = \rho(r_0)RT_0 + \int_r^{r_0} \rho(y)g(y)dy \tag{4.3}$$

$$T(r) = \frac{P(r)}{\rho(r)R} = \frac{\rho(r_0)}{\rho(r)}T_0 + \frac{\int_r^{r_0} \rho(y)g(y)dy}{\rho(r)R}. \tag{4.4}$$

where $R$ is the ideal gas constant, $r_0$ is the top of the sensible atmosphere where the refractive index is unity at a temperature $T_0$, $\rho$ is the density in kg/m$^3$, $g$ is the acceleration of gravity in m/s$^2$, $P$ is the pressure in Pascals and $T$ is the temperature in Kelvin.

Abundance profiles of absorbing constituents can be derived from the variation in signal amplitude. The factors which affect signal amplitude during radio occultation experiments include refractive defocusing, antenna pointing and absorption and scattering in the atmosphere. The power profile in dB, consists of three terms

$$p(r) = -\tau(r) + p_{ant}(r) + p_n(r) \tag{4.5}$$

where $\tau$ is the excess attenuation due to absorption (dB), $p_{ant}$ is the power drop due to antenna mispointing (dB) and $p_n$ is the power drop due to refraction (dB). The refractive defocusing can be calculated and removed from the power profile using the following equation (Eshleman, *et. al*, 1980)

$$p_n = 10\log_{10}\left[\frac{y}{a}\left(1 - R_2\frac{d\delta}{da}\right)\right] \tag{4.6}$$

where $y$ and $R_2$ are shown in Figure 4.2, $p_n$ is in dB and $\delta$ is in radians. The antenna mispointing attenuation can be corrected by calculating the gain of the particular antenna in use along the true ray path to Earth and the rest of the attenuation is attributed to absorption given by (Jenkins *et. al*, 1994)

$$\tau(a) = 2\int_a^\infty \frac{\alpha(x)dr/da(x)xdx}{\sqrt{x^2 - a^2}}. \tag{4.7}$$

The absorptivity (dB/km) can be recovered by

$$\alpha(a) = -\frac{da}{dr}(a)\frac{1}{\pi a}\frac{d}{da}\left[\int_a^\infty \frac{\tau(x)xdx}{\sqrt{x^2 - a^2}}\right]. \tag{4.8}$$

In order to use the above equations for the retrieval of temperature-pressure profiles from radio occultation data, it is assumed that the center of the planet is the center of refraction (see Figure 4.2). For spherical atmospheres such as Venus this assumption is suitable; however for an oblate planet such as Saturn, this assumption can yield incorrect profiles. To make accurate retrievals of the structure of an oblate planet, the new center of refraction must be calculated and then the above Abelian transforms can be used for calculations. Note that the center of refraction changes at each point in time and it can move away from the planet center and back again towards it as the signal penetrates the neutral atmosphere. The new center of refraction must then be estimated

to be between these two extreme points and used as the center of refraction for calculations. Kliore and Woichesyn (1976) used a method to calculate the new center of refraction for occultations of Jupiter, also an oblate planet, by considering the shape of the planet. The next section describes a radio occultation simulator specific to Saturn which predicts attenuation and Doppler profiles.

## 4.2 Radio Occultation Simulator

Steffes *et. al* (1994) describe a radio occultation simulator for a spherical planet like that of Venus. This section describes a radio occultation simulator specific to Saturn and can be used for any oblate planet given a reasonably accurate model atmosphere. The results of the simulations can be used to study the sensitivity of the Cassini three-frequency radio link to the atmospheric constituents encountered during radio occultation. The Cassini radio occultation experiments will use three transmitters, one at 2.3 GHz (S-band), one at 8.4 GHz (X-band) and the third at 32 GHz (Ka-band). The results of laboratory measurements of the 9 mm opacity of phosphine and ammonia (given in Chapter 2) and the centimeter wavelength opacity of these constituents measured under simulated conditions for Saturn (see, e.g., Hoffman et. al. 2001) were incorporated into the model which was used to calculate attenuation profiles of these microwave absorbers. The model was created given the composition and structure of the atmosphere, the spacecraft trajectory data file and Earth and Saturn's ephermerides, which are the coordinates of the Earth and Saturn at a number of specific times during a given period. The radio occultation simulator is an important tool since predicted Doppler shifts can be used to reduce the bandwidth of the receiving system. The excess Doppler shift and refractive

defocusing were determined using the simulated ray paths and trajectory files provided by the Cassini mission.

### 4.2.1 Model Atmosphere

The spacecraft's signal is modeled as a ray and traced through the model atmosphere of Saturn in order to determine the radio occultation geometry at each point in time (see Figure 4.2). This section describes how the model atmosphere of Saturn was determined. A thermochemical model (TCM) was used to profile the abundances of atmospheric constituents and temperature as functions of altitude from the center of the planet and total pressure. The thermochemical model (TCM) developed by DeBoer and Steffes (1996) computes the temperature-pressure profile (T-P profile) starting at 70 bars and ending at 0.0631 bar assuming an adiabatic atmosphere in hydrostatic equilibrium. The TCM starts with an assumption of temperature at 70 bars and the deep abundances of atmospheric constituents where all are gaseous. It then steps up in discrete layers of pressure (altitude) calculating the new temperature at each successive layer. At each pressure increment each constituent's partial pressure is compared to its saturation vapor pressure. If the partial pressure exceeds its saturation vapor pressure for that layer's temperature, condensation occurs and the new temperature and mixing ratios are determined. A previously measured T-P profile from the Voyager radio occultation experiment (Lindal *et. al*, 1985) is used to force an agreement at 1.29848 bars. For a more complete discussion of thermochemical models of the outer planets see de Pater and Massie (1985). Although the T-P profile of the neutral atmosphere of Saturn was

modeled from 0.0631 bars down to 70 bars, the signal cannot be detected at depths below the 2 bar pressure level during the radio occultation experiments at any frequency.

The TCM also provides temperature and pressure profiles as a function of altitude. Lindal *et. al* (1985) determined the size and shape of Saturn's isobaric surfaces using data from the occultations of Voyager 1 and 2. The 1 bar isobaric surface has a polar radius of 54 364 ± 10 km and an equatorial radius of 60 268 ± 4 km resulting in an oblateness, $(R_{eq} - R_p)/R_{eq}$, of 0.09796 ± 0.000 18. The corresponding values at 100-mbar are 54 438 ± 10 km, 60 367 ± 4 km and 0.098 22 ± 0.000 18. The polar and equatorial radii (relative to the planet center) of each layer in the model atmosphere were derived using this data. See Appendix A for the complete results of the model atmosphere.

The assumed deep atmospheric relative abundances by volume of the atmospheric constituents were $154 \times 10^{-6}$ hydrogen sulfide, $412.5 \times 10^{-6}$ ammonia, $1 \times 10^{-6}$ water vapor, $4.2 \times 10^{-3}$ methane, $9.3 \times 10^{-6}$ phosphine and 0.07 helium with the remaining being hydrogen. The deep abundance of phosphine corresponds to the preliminary results from the vertical profiles of phosphine on Saturn derived from the Cassini/CIRS far-infrared observations as reported by Irwin *et. al* (2004). At 35 South the estimated abundance of phosphine is $8 \times 10^{-6}$ at 0.595 bar decreasing to $5 \times 10^{-7}$ at 0.16 bar. In the radio occultation model, the phosphine mixing ratio at pressures greater than or equal to 0.66 bar is $9.3 \times 10^{-6}$ and this decreases linearly in log (pressure) versus log (mixing ratio) to a value of $4.1 \times 10^{-7}$ at 0.15 bar which is in accordance with Orton *et al.* (2000). Unlike ammonia, phosphine does not condense in the atmosphere of Saturn however it is thought to be depleted by photolysis in the upper troposphere (Prinn and Lewis, 1975). The ammonia, hydrogen sulfide and water vapor mixing ratios were chosen judiciously,

resulting in a close match of modeled to measured emission spectra (Hoffman 2001). The methane mixing ratio was taken from Courtin *et al.* (1984) and the hydrogen to helium mixing ratio is that reported in Atreya *et. al* (1999). See Figure 4.3 for the projected profiles of ammonia and phosphine mixing ratios in Saturn's atmosphere.

For the pressures probed during the radio occultation experiments, only hydrogen, helium and methane cause significant bending of the spacecraft's signal. The normalized refractivities, $N'$ of hydrogen and helium used in the calculations are (Essen 1953)

$N'_{H_2} = 5.06 \times 10^{-18}$ N-units cm$^3$ molecule$^{-1}$

$N'_{He} = 1.30 \times 10^{-18}$ N-units cm$^3$ molecule$^{-1}$ and

$N'_{CH_4} = 1.67 \times 10^{-17}$ N-units cm$^3$ molecule$^{-1}$ (Watson and Ramaswamy, 1936). These values are converted to refractive index (see section on refractivity in Chapter 2) and used in the ray tracing technique.

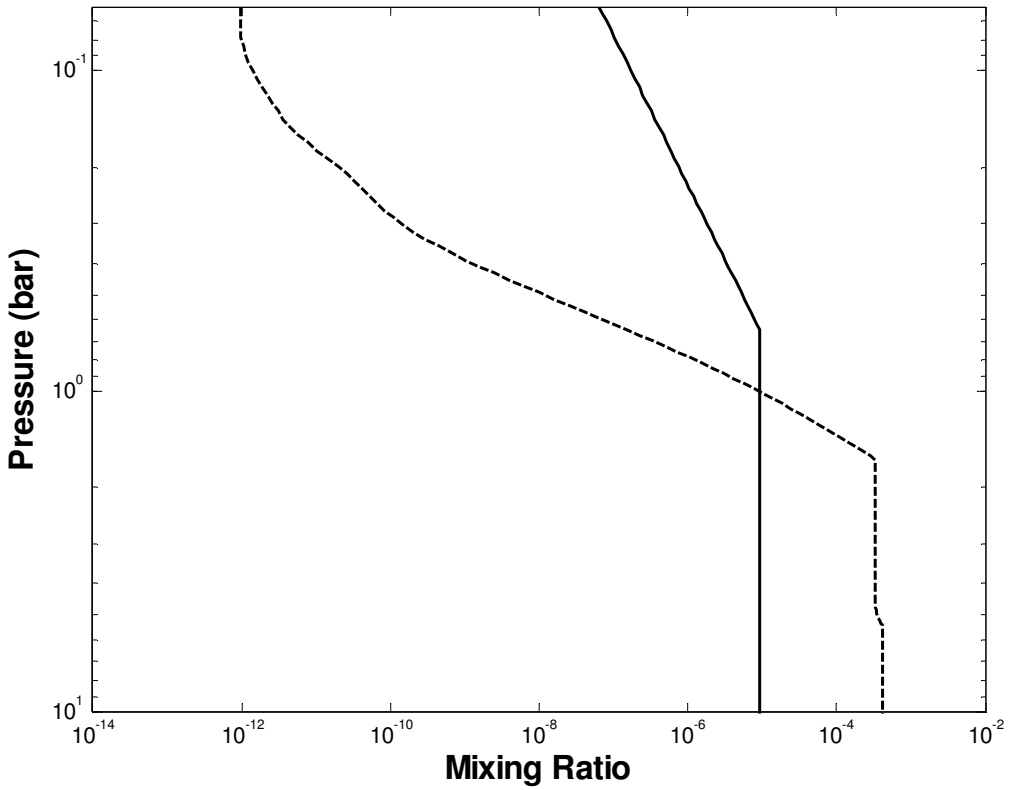


Figure 4.3: Mixing ratio profile of phosphine (solid line) and ammonia (dashed line) in the atmosphere of Saturn. At pressures less than 2 bars these are the only significant microwave absorbers.

### 4.2.2 Ray Tracing

Figure 4.2 shows the occultation geometry for a spherical planet where the Earth station, planet center and the spacecraft are all in the same plane of propagation. For an oblate planet, the plane of propagation contains the Earth station, the spacecraft and a center of refraction that is displaced from the planet center (see Figure 4.4). The true center of refraction, also called the center of symmetry, is different at each point in time. For this reason, the equations which govern a spherical atmosphere which use the center of the

planet as the center symmetry can yield inaccurate information if used to describe an oblate planet such as Saturn (see Ahmad and Tyler (1999) for a complete description of errors induced by using Abelian inversions on oblate atmospheres assuming spherical symmetry). For this research, a ray-tracing program is used to find the actual ray paths of the signal through the atmosphere of Saturn. During occultation, as the probe flies behinds the planet as viewed from Earth, an un-modulated signal, modeled as a ray, traverses the atmosphere and is received on Earth. For modeling purposes it was easier to model the ray as originating from Earth. The ray paths are equivalent whether the ray originates on Earth or the spacecraft. The spacecraft trajectory data (provided by the Cassini Radio Science team) and Earth and Saturn ephermerides were transformed to a Saturn co-ordinate system where the center of Saturn is the origin, the z axis is in the polar direction and the x axis is on the equator towards the direction of earth. The shape of Saturn can be described as an oblate spheroid where the radius along the x and y axes (equatorial radius) is greater than the radius along the z axis (polar radius). The planet is modeled as ellipsoidal shells which are 2 km apart along the x axis, with each shell (layer) having a discrete temperature, pressure and thus refractive index. As discussed below, tracing a ray through a planetary atmosphere can result in three types of solutions depending on the direction of the ray from the transmitter. (In this case we're modeling the Earth as the transmitter.) The ray tracing solutions, as well as the ray-tracing algorithm are described in detail in Hoffman (Hoffman 2001).

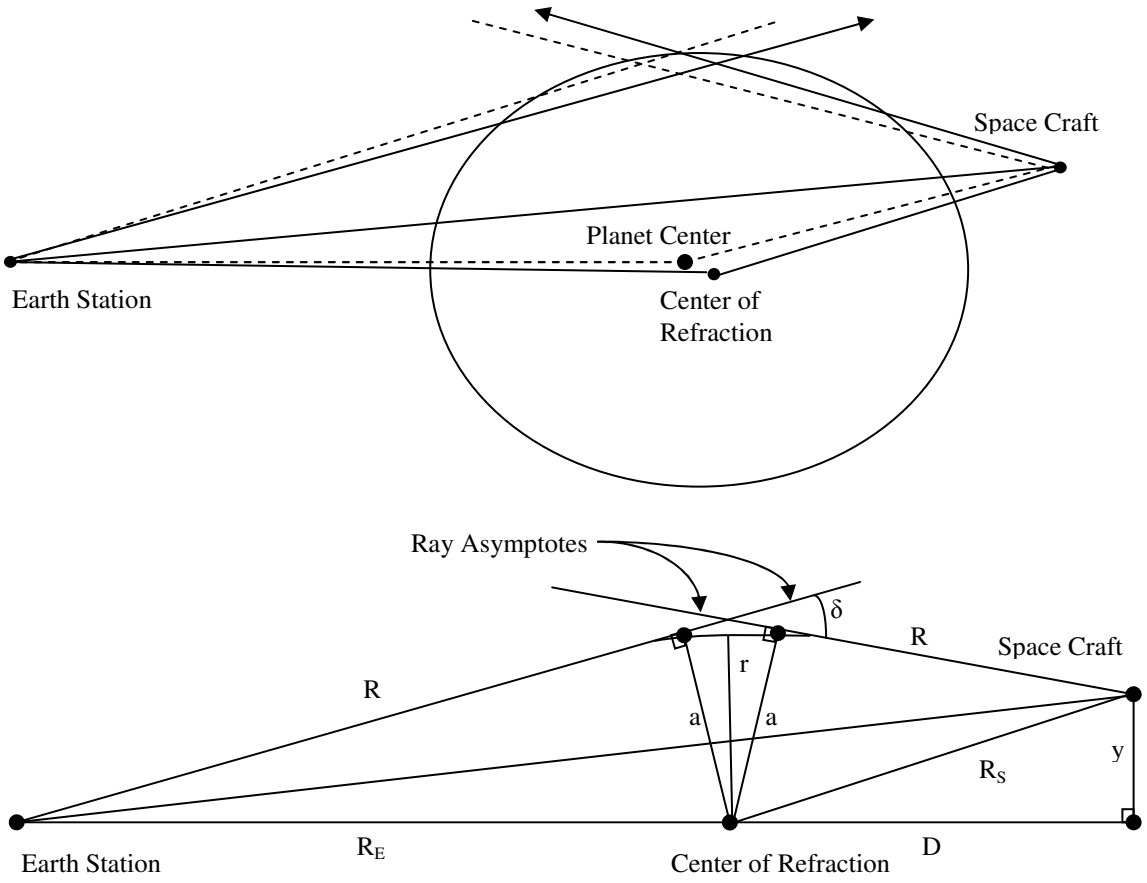


Figure 4.4: The dashed line shows the occultation geometry assuming the center of refraction is the planet center. The solid line indicates the actual occultation geometry for an oblate atmosphere with the center of refraction being displaced from the center of the planet. The true center of refraction is different at each point in time.

During the period of a typical occultation (less than 10 minutes) the Earth's motion is negligible and can be considered stationary. The dynamical properties of Saturn's atmosphere are also ignored. The ray-tracing algorithm begins with the ray direction pointed towards the moving spacecraft until the ray intersects the planet's first ellipsoidal shell defined by the polar and equatorial radii at that isobaric surface. The distance to the planet, $d_1$, is calculated; the angle of incidence is determined and Snell's law is applied at the interface to find the vector direction of the transmitted ray through the first layer (see Figures 4.5 and 4.6). The point of intersection of the ray and the first ellipsoid then becomes the ray origin and the transmitted ray defines the new ray direction. The algorithm continues by finding the point of intersection of the transmitted ray and the second ellipsoid and the distance it travels, $d_2$. Snell's law is again applied at the second interface and the process continues for the subsequent layers until the atmosphere becomes so opaque to the signal that there is no transmission (also known as solution 1). Alternatively, the ray could pass through to the other side of the planet, a geometry known as limb sounding (solution 2). Solution 3 occurs during limb sounding when the exiting ray encounters a decreasing refractive index and critical refraction or total internal reflection occurs. Solution 2 yields the correct answer required to create functional radio occultation geometry at each point in time.

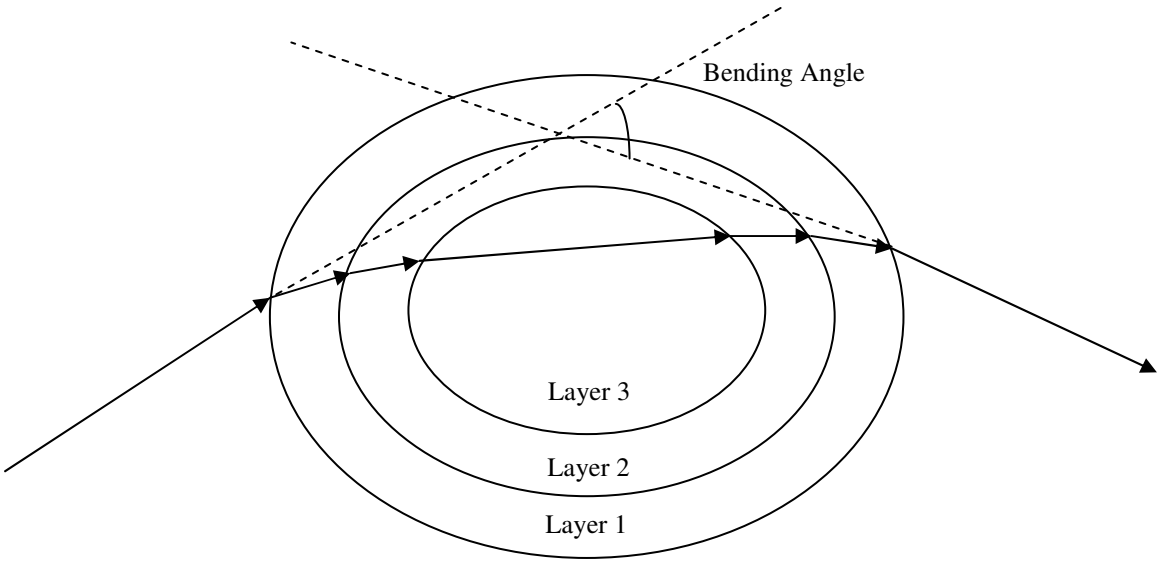


Figure 4.5: Limb sounding geometry

### 4.2.3 Ray Tracing Algorithm

The equations used in the ray-tracing part of the occultation simulator are described in Haines (1989). The equations for a sphere were replaced by the equation for an ellipsoid to create a ray-ellipse intersection algorithm (Hoffman 2001).

Definition of a ray:

$$R_{origin} \equiv R_0 \equiv \begin{bmatrix} X_0 & Y_0 & Z_0 \end{bmatrix} \tag{4.1}$$

$$R_{direction} \equiv R_d \equiv \begin{bmatrix} X_d & Y_d & Z_d \end{bmatrix} \tag{4.2}$$

where $R_d$ is a unit vector thus,

$$X_d^2 + Y_d^2 + Z_d^2 = 1. \tag{4.3}$$

The above equations describe the ray as a set of points on a line:

$$R(t) = R_0 + R_d * t \text{, where } t > 0. \tag{4.4}$$

The variable $t$ is the distance in km from the ray's origin.

The equation for an ellipsoid is

$$\left(\frac{X_s}{a}\right)^2 + \left(\frac{Y_s}{b}\right)^2 + \left(\frac{Z_s}{c}\right)^2 = 1 \tag{4.5}$$

where $a$, $b$ and $c$ are the vertices of the $x$, $y$ and $z$ axes on the ellipse. For Saturn, $a = b$ and $a > c$, where $a$ is the equatorial radius and $c$ is the polar radius of the ellipsoid.

$$S_{center} \equiv S_c = \begin{bmatrix} 0 & 0 & 0 \end{bmatrix} \tag{4.6}$$

$$S_{surface} = \begin{bmatrix} X_s & Y_s & Z_s \end{bmatrix} \tag{4.7}$$

The ray equation expressed as a set of equations for the points $\begin{bmatrix} X & Y & Z \end{bmatrix}$:

$$\begin{aligned} X &= X_0 + X_d t \\ Y &= Y_0 + Y_d t \\ Z &= Z_0 + Z_d t \text{ .} \end{aligned} \tag{4.8}$$

Equations 5.8 are substituted into 5.5 and the result is solved for $t$ to find the intersection point of the ray and ellipsoid. The resulting equation that needs to be solved is

$$\left(\frac{X_0 + X_d t}{a}\right)^2 + \left(\frac{Y_0 + Y_d t}{b}\right)^2 + \left(\frac{Z_0 + Z_d t}{c}\right)^2 = 1 \tag{4.9}$$

This equation simplifies to a quadratic equation:

$$At^2 + Bt + C = 0 \tag{4.10}$$

where,

$$\begin{aligned} A &= \Lambda X_d^2 + \mathrm{Y} Y_d^2 + \mathrm{K} Z_d^2 \\ B &= 2\left(\Lambda X_0 X_d + \mathrm{Y} Y_0 Y_d + \mathrm{K} Z_0 Z_d\right) \end{aligned} \tag{4.11}$$

$$C = \Lambda X_0^2 + \mathrm{Y} Y_0^2 + \mathrm{K} Z_0^2 - 1$$

and

$$\Lambda = \frac{1}{a^2},\ \mathrm{Y} = \frac{1}{b^2},\ \mathrm{K} = \frac{1}{c^2} \tag{4.12}$$

The solutions to the quadratic equation are

$$t_0 = \frac{-B - \sqrt{B^2 - 4AC}}{2A}$$

$$t_1 = \frac{-B + \sqrt{B^2 - 4AC}}{2A}. \tag{4.13}$$

If $t$ is complex, then the ray misses the ellipsoid. The correct solution is the smallest positive $t$, which is the distance the ray travels through any given layer. With a correct solution for $t$, the intersection point is,

$$r_{\text{int}} = r_i = \begin{bmatrix} x_i & y_i & z_i \end{bmatrix} = \begin{bmatrix} X_0 + X_d t & Y_0 + Y_d t & Z_0 + Z_d t \end{bmatrix} \tag{4.14}$$

The local normal is defined as

$$r_{normal} \equiv n = \frac{\nabla G}{|\nabla G|} \tag{4.15}$$

where

$$\nabla G = \frac{2x}{a^2} i + \frac{2y}{b^2} j + \frac{2z}{c^2} k \tag{4.16}$$

and

$$|\nabla G| = 2\sqrt{\frac{x^2}{a^4} + \frac{y^2}{b^4} + \frac{z^2}{c^4}}. \tag{4.17}$$

$G$ is denoted as the surface of the ellipsoid volume which is defined by equation 5.5. If the ray originates inside the sphere and thus hits the inside, $r_{normal}$ should be negated so that it points back towards the ray. See Figure 4.6 for the geometry of transmission.

When using Snell's law at an interface, the origin of the transmitted ray is the point of intersection $r_{int}$ while the surface normal is $r_{normal}$. The transmission of a ray between media with different refractive indices uses Heckbert's method (Heckbert, 1989) which is a vector approach. The incident angle is calculated using the incident ray vector (**I**) and the local surface normal (**N**), where **I** and **N** are unit vectors,

$$\cos(\theta_1) = -\mathbf{I} \cdot \mathbf{N} . \tag{4.18}$$

The relative index of refraction ($\eta$) using Snell's law is

$$\eta = \sin(\theta_2) / \sin(\theta_1) = \eta_1 / \eta_2 \tag{4.19}$$

and the angle of the transmitted ray is derived from known quantities using

$$\cos(\theta_2) = \sqrt{(1 - \sin^2(\theta_2))} = \sqrt{(1 - \eta^2 \sin^2(\theta_1))} = \sqrt{(1 - \eta^2 (1 - \cos^2(\theta_1)))} . \tag{4.20}$$

The vector direction of the transmitted ray can then be obtained by

$$\mathbf{T} = \eta \mathbf{I} + (\eta \cos(\theta_1) - \cos(\theta_2))\mathbf{N} . \tag{4.21}$$

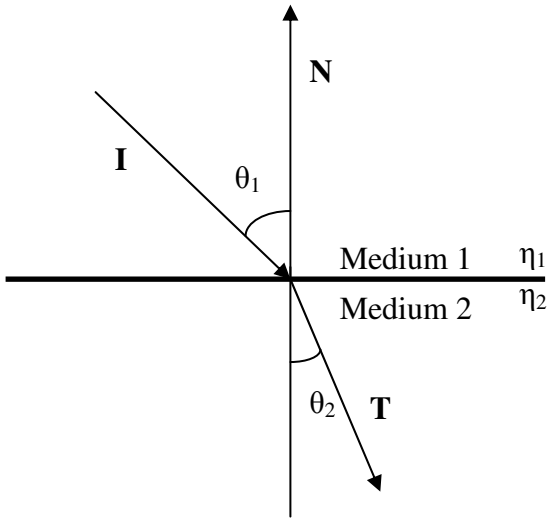


Figure 4.6: Geometry of transmission

### 4.2.4 Solution of the Radio Occultation Geometry

The ray tracing algorithm was written and executed in Matlab ™. The algorithm was used to find a ray from Earth which intersects the spacecraft when traced through the atmosphere. This is essentially a root finding problem in two dimensions where the solvable parameters are the angle above the Earth-Saturn line and the azimuth angle about this line. A grid of launch and azimuth angles was created and these rays were traced through Saturn's atmosphere, recording the directions and positions of the rays as they exited the atmosphere and traveled in straight lines again. For a given spacecraft position, the miss distance for each of the rays in the grid was evaluated, and the ray that intersects the spacecraft was that with the least miss distance. The Matlab ™ function "fminsearch" was then used to locate the ray that had a miss distance of less than 1 km. An example of a ray tracing solution is shown in Figure 4.7.

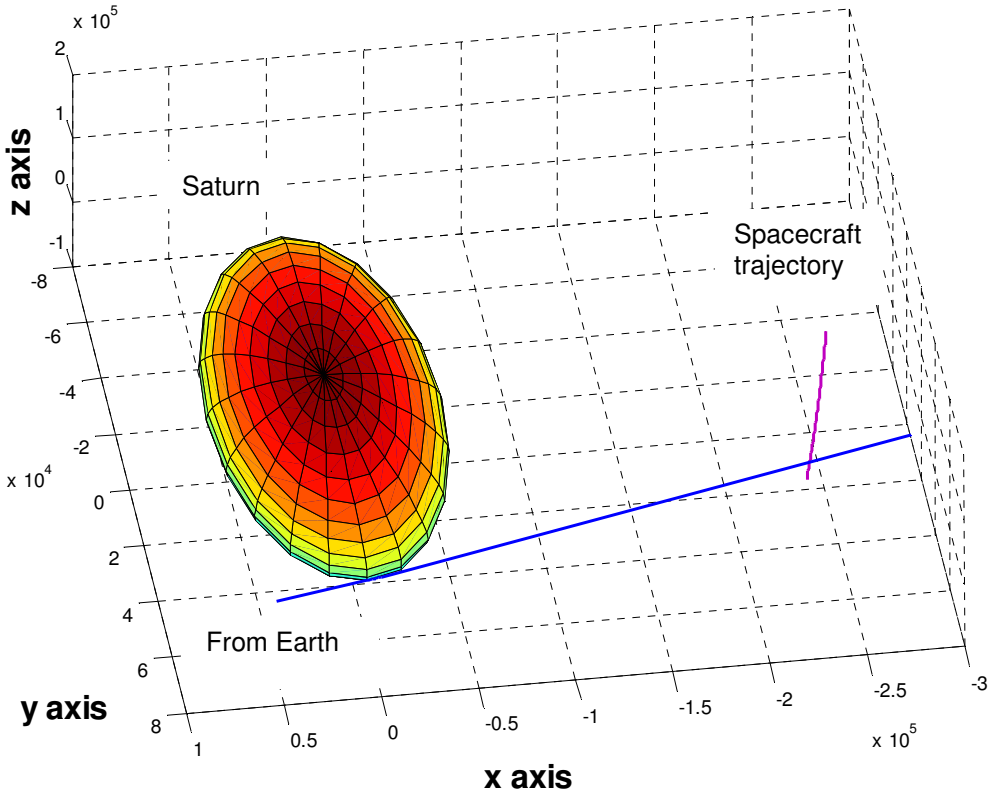


Figure 4.7: An example of a ray tracing solution

## 4.3 Occultation Geometries as seen from Earth

The radio occultation software was used to simulate four different occultation geometries at both ingress and egress as shown in Figures 4.8 though 4.11. The results of revolutions (orbits) 7 and 70 are presented in this chapter since they represent near equatorial and near polar orbits respectively. See Appendix B for the results of the other orbits.

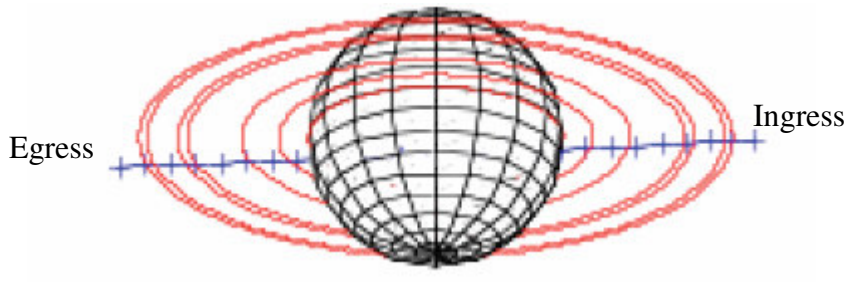


Figure 4.8: Revolution 7. May 3, 2005.

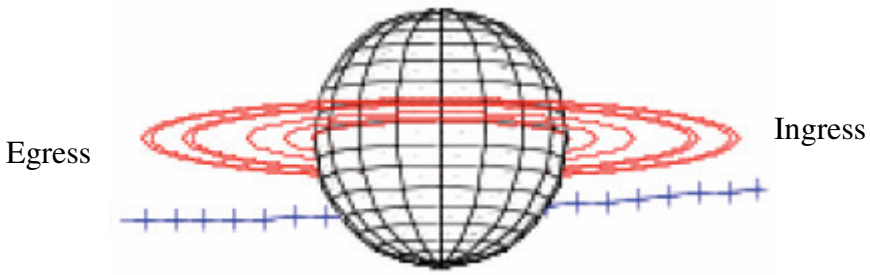


Figure 4.9: Revolution 51. October 24, 2007.

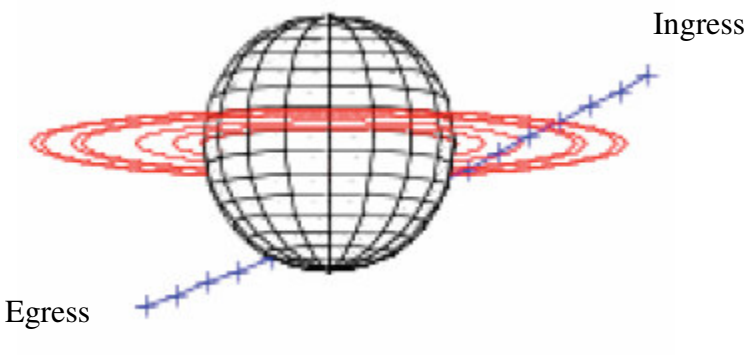


Figure 4.10: Revolution 54. December 19, 2007.

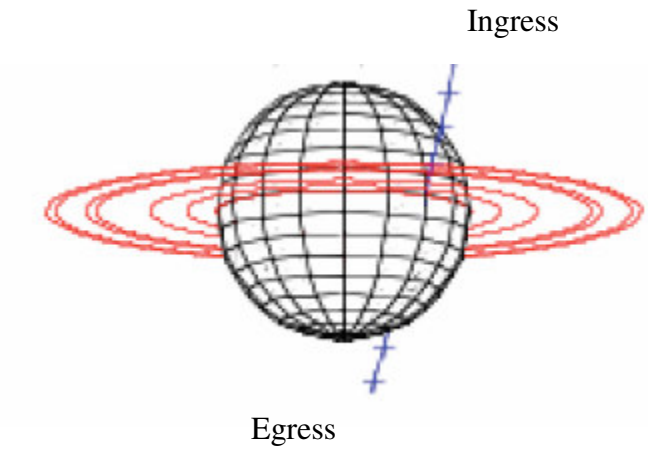


Figure 4.11: Revolution 70. June 1, 2008.

## 4.4 Doppler Shifts

The signals received at the DSN from various spacecraft experience shifts in frequency due to the Doppler effect since the Earth and spacecraft are moving with respect to each other, even in the absence of a planetary atmosphere. In the presence of a planetary atmosphere, the bending of the ray path produces an increase in the velocity component of the spacecraft relative to the earth with an accompanying change in frequency. This extra shift is called the excess Doppler shift. There is also a propagation delay due to the reduction of the signal velocity in the atmospheric medium with respect to the signal in a vacuum.

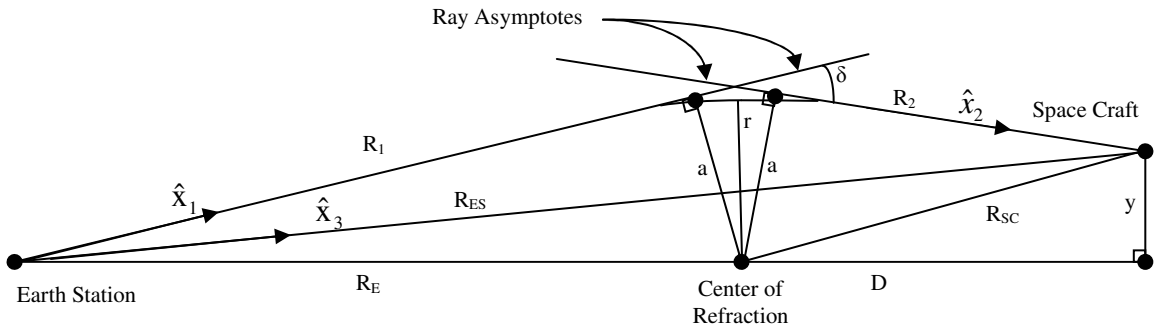


Figure 4.12: Occultation geometry

For a given ray, the frequency of the signal received at earth, $f_{er}$, is related to the frequency, $f_x$, of the reference signal transmitted from the spacecraft by

$$f_{er} = f_x \frac{c + v_r}{\sqrt{c^2 - v_r^2}} \tag{4.22}$$

where $v_r$ is the relative velocity and $c$ is the speed of light. The relative velocity is evaluated by projecting the velocity of the Earth and the spacecraft onto the ray asymptotes as follows:

$$v_r = \vec{v}_e \cdot \hat{x}_1 - \vec{v}_{sc} \cdot \hat{x}_2 . \tag{4.23}$$

The frequency expected in the absence of an atmosphere is calculated as in equation 4.23 except that the relative velocity is given by

$$v_r' = \vec{v}_e \cdot \hat{x}_3 - \vec{v}_{sc} \cdot \hat{x}_3 \tag{4.24}$$

and the excess Doppler shift due to bending in the atmosphere is

$$f_r = f_{er}' - f_{er} . \tag{4.25}$$

The vectors $\hat{x}_1$, $\hat{x}_2$ and $\hat{x}_3$ are shown in Figure 4.12. Equation 4.25 is the difference between the frequency expected had no bending occurred and the frequency of the received signal after it probes the atmosphere. The transmitter frequencies used in calculations are 32.02344 GHz (Ka-band), 8.4272 GHz (X-band) and 2.29833 GHz (S-band).

The predicted excess Doppler shifts are plotted for each of the three transmitter frequencies for Revolutions 7 and 70 at both ingress and egress. The results, shown in Figures 4.13 through 4.15, are calculated for the time period where the signal to noise ratio at the receiving station drops to 3 dB or less. See section 4.5 for attenuation profiles and predictions of signal cutoffs. The results for the other two orbits are in Appendix B.

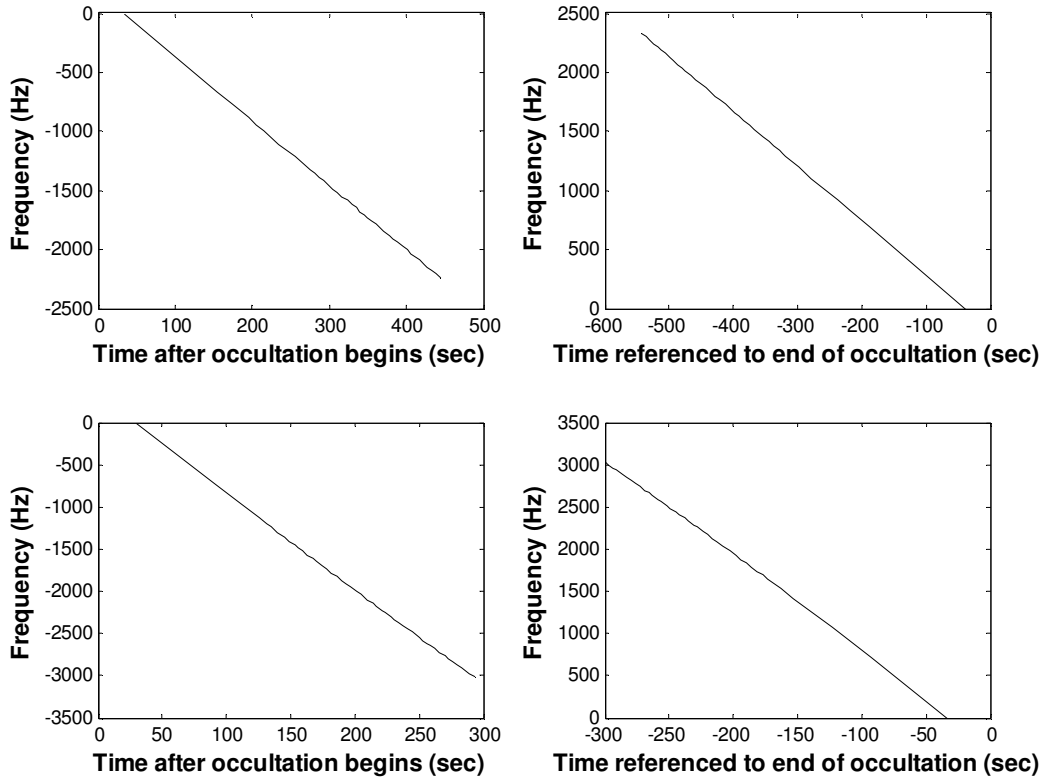


Figure 4.13: Predicted excess Doppler shifts of the S-band carrier signal from Cassini as measured at Earth. The top two graphs are for Revolution 7 with the left being ingress and the right egress. The bottom two graphs are for Revolution 70, the left ingress, the right egress.

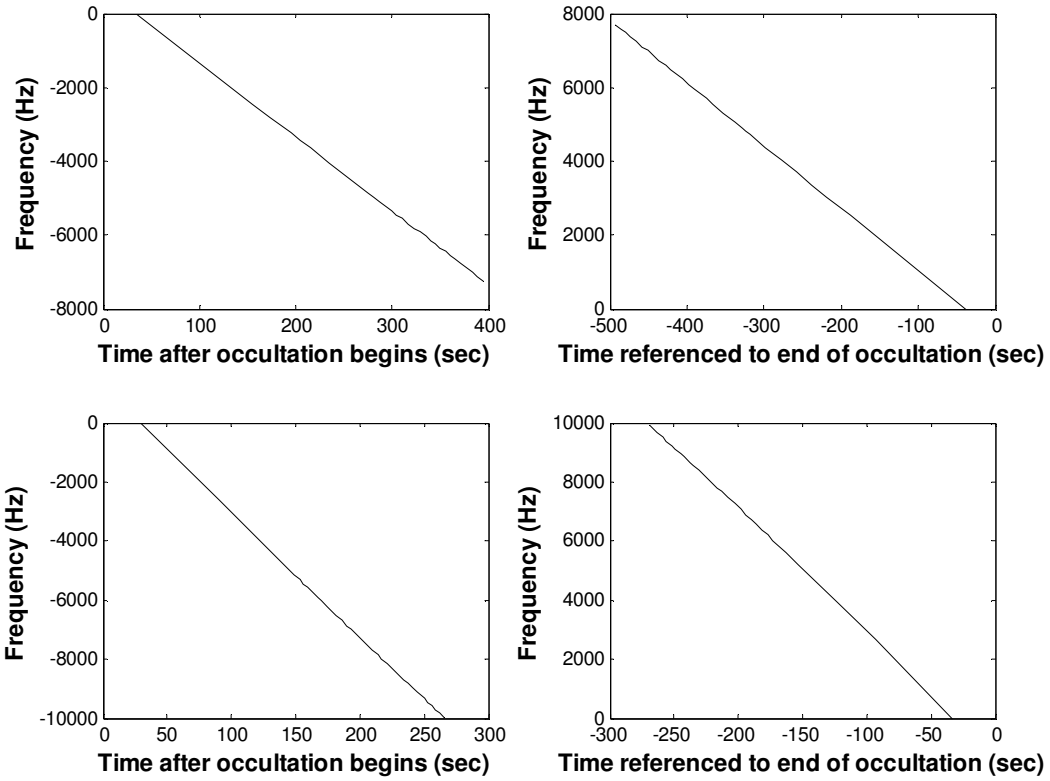


Figure 4.14: Predicted excess Doppler shifts of the X-band carrier signal from Cassini as measured at Earth. The top two graphs are for Revolution 7 with the left being ingress and the right egress. The bottom two graphs are for Revolution 70, the left ingress, the right egress.

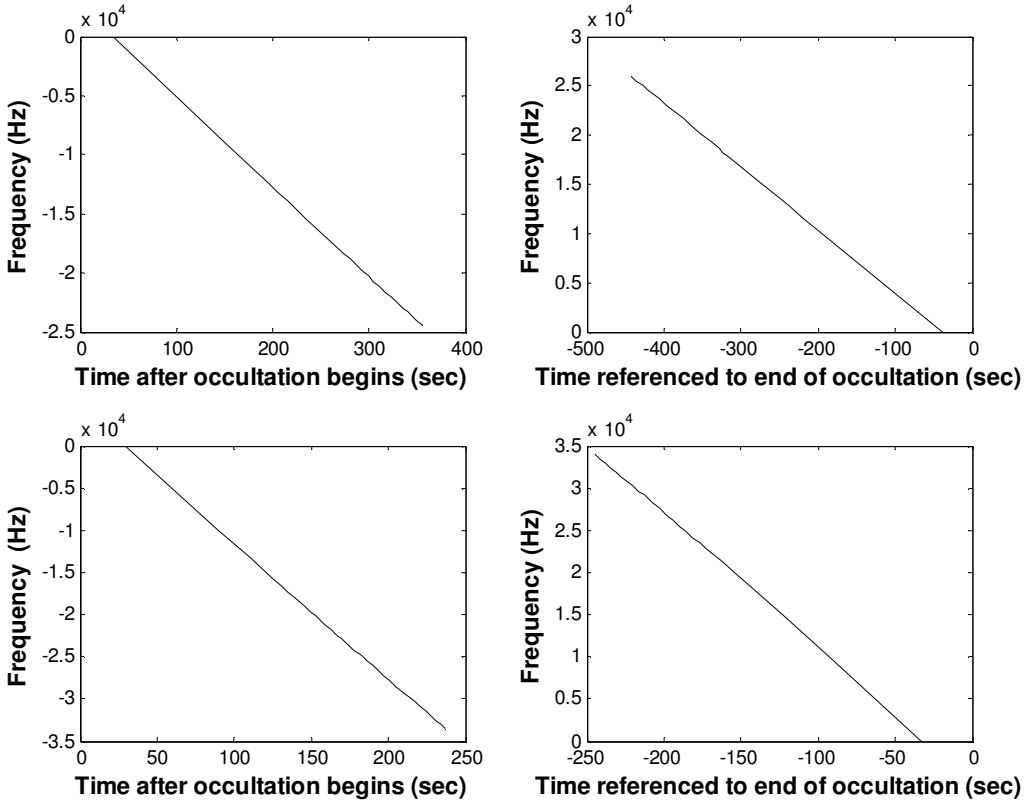


Figure 4.15: Predicted excess Doppler shifts of the Ka-band carrier signal from Cassini as measured at Earth. The top two graphs are for Revolution 7 with the left being ingress and the right egress. The bottom two graphs are for Revolution 70, the left ingress, the right egress.

## 4.5 Attenuation Profiles

### *Phosphine and Ammonia*

During a radio occultation experiment, the signal not only encounters ray bending and excess Doppler shift due to the atmosphere, but also the signal intensity decreases due to microwave absorbing constituents and refractive defocusing. Refractive defocusing will be discussed in the next section. The model atmosphere described in a previous section indicates that Saturn's atmosphere consists mainly of hydrogen and helium with much smaller amounts of ammonia, phosphine, methane, hydrogen sulfide and water vapor. Phosphine and ammonia are the only constituents considered in the model of microwave absorption in the atmosphere. The minute abundances of hydrogen sulfide and water vapor in the pressure regions probed contribute very little to the absorptivity (dB/km). Methane, like hydrogen and helium exhibits minimal microwave absorption.

In order to determine absorption due to phosphine, an absorptivity profile (dB/km) of the atmosphere is first created for each transmitter frequency. This is done using the formalism for phosphine opacity described in Hoffman *et. al* (2001) with inputs of temperature, pressure, mixing ratio of constituents and frequency. The work described in Chapter 2 shows that this phosphine formalism accurately predicts opacity at Ka-band and since the formalism is based on centimeter wave measurements, it can be used at all three transmitter frequencies. The section 4.4.4 on ray tracing describes how the ray paths through the atmosphere are calculated. As the ray is traced, the distance through each layer is recorded (see Figure 4.5 for limb sounding geometry). Using the absorptivity profile of a particular frequency, the absorption (dB) is then calculated by multiplying the distance by the absorptivity (dB/km) at each layer and summing to

determine the absorption due to phosphine at each point in time. See Figures 4.19 though 4.30 for profiles of absorption due to phosphine versus time. The ammonia profiles are computed in a similar fashion. The formalism used to determine ammonia absorptivity at Ka-band is described in Chapter 2 and that used at S and X bands is described by Berge and Gulkis (1976).

***Refractive Defocusing***

As a signal traverses the atmosphere, the beam is spread in the plane of the occultation and compressed in the orthogonal direction. This results in a signal intensity reduction which is calculated as per Eshleman *et. al* (1980)

$$p_n = 10\log_{10}\left[\frac{y}{a}\left(1 - R_2\frac{d\delta}{da}\right)\right] \tag{4.26}$$

where $y$, $a$, $R_2$, $\delta$ are shown in Figure 4.11 and $p_n$ is in dB. The above equation uses the assumption of spherical symmetry of the planet. As mentioned earlier, using the center of the planet as the center of refraction on an oblate atmosphere can result in erroneous results. However, since the part of the atmosphere that interacts with radio waves during occultation is a small section of the planet, this section can be treated as approximately spherical where the center of symmetry (refraction) is different from the center of the planet. Once a new center is calculated at each point in time, equation 4.26 can be used to calculate refractive defocusing where the equation parameters are with respect to the new center. (See Figure 4.12) The new center of refraction is calculated using the ray asymptotes found in ray tracing and error determining parameters expressed in Ahmad and Tyler (1999).

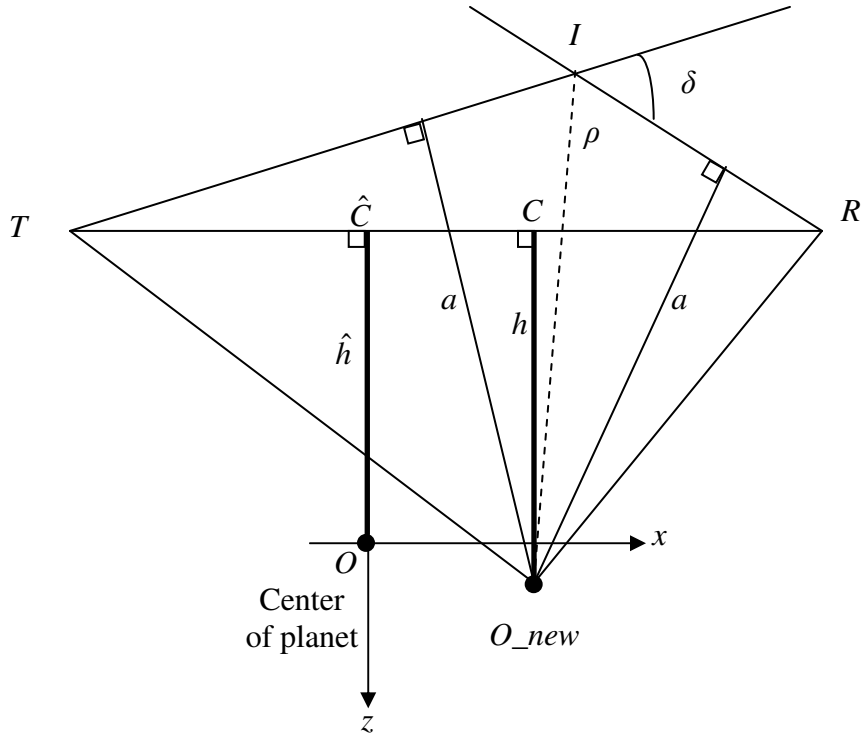


Figure 4.16: Occultation geometry in the true plane of propagation *O_newTR*. The *y* component is not shown in figure. Line TR is contained in this plane as well as the plane OTR, the assumed plane of propagation.

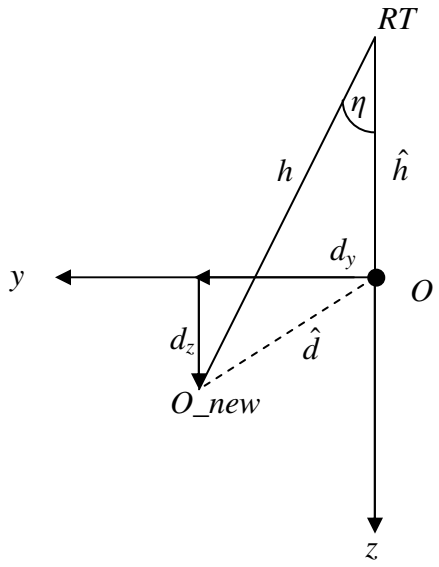


Figure 4.17: Occultation geometry of the above figure viewed from the receiver along the TR line. The planes *OTR* and *O_newTR* intersect at an angle, $\eta$, along the line TR.

Figures 4.16 and 4.17 show the occultation geometry with respect to the new center of refraction, *O_new*. The coordinate system in these figures is defined for each individual ray. In this coordinate system, the *y* component of the vector distance, $\hat{d}$ is always in the positive *y* direction and $\hat{d}$ is defined as (Ahmad and Tyler, 1999)

$$\hat{d} = d_x\hat{x} + d_y\hat{y} + d_z\hat{z} \tag{4.27}$$

$$\Delta l = -d_x \tag{4.28}$$

$$\eta \approx \frac{d_y}{\hat{h}} \tag{4.29}$$

$$\Delta h \approx -d_z - \frac{d_y^2}{2\hat{h}} \tag{4.30}$$

$$\Delta h = \hat{h} - h \tag{4.31}$$

$$\Delta l = \left|T\hat{C}\right| - \left|TC\right| = \left|RC\right| - \left|R\hat{C}\right|. \tag{4.32}$$

Since *O_new* is unknown, then *C* is unknown thus the *x* and *z* components of $\hat{d}$ cannot be calculated directly. However the angle, $\eta$, between the planes *OTR* and *O_newTR* can be determined and thus can $d_y$. In figure 4.16, TIR is known from ray tracing. The point, *I* is transformed from the coordinate system in the ray tracer to the coordinate system defined here, and using $d_y$, the distance, $\rho$ (distance from *O_new* to *I*), is obtained from

$$O\_new = I + \rho\hat{\rho} \tag{4.33}$$

where $\hat{\rho}$ is the unit vector in the direction of *IO_new*. The distance $\rho$ is then used to recover the vector *O_new* with respect to the planet center, *O*, in the coordinate system defined in the ray tracing algorithm. The results of the refractive defocusing are plotted in Figures 4.19 though 4.30. Figure 4.18 shows the results of the refractive defocusing

calculated by the above method as opposed to assuming the planet center is the center of refraction. In this plot the difference is as much as 1.5 dB and for other orbits the difference is about 2 dB or less.

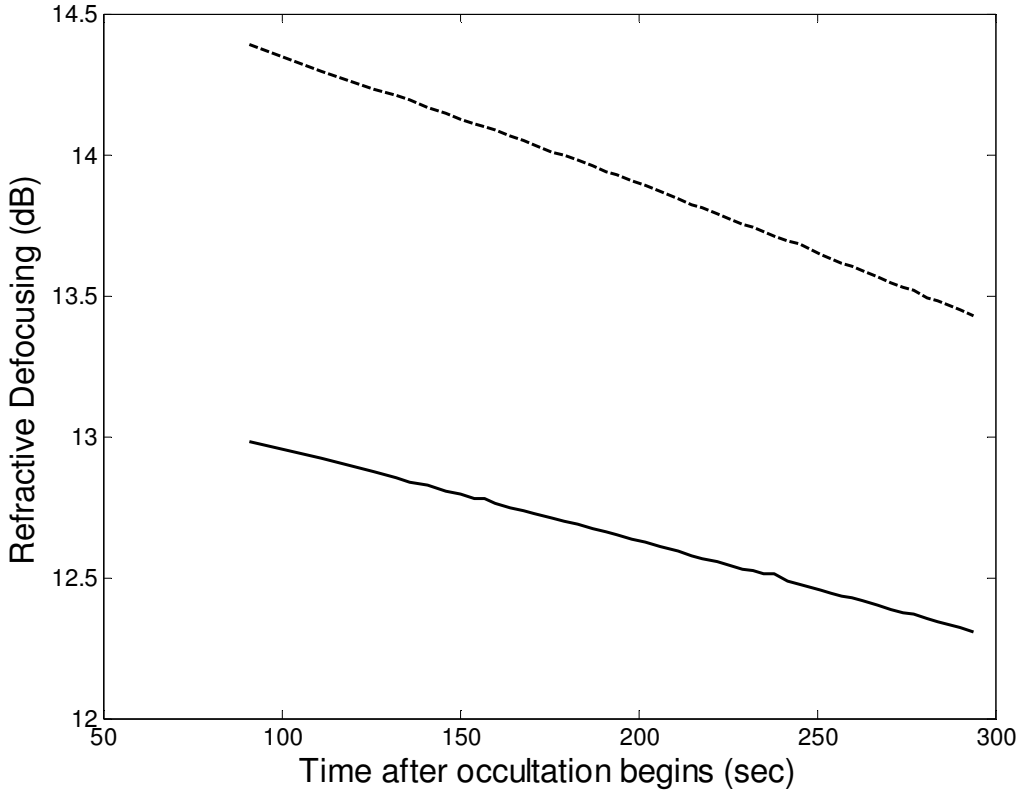


Figure 4.18: The plot shows the refractive defocusing calculated using the method described above (solid line) and that assuming the center of refraction is the planet center (dashed line). This example is from Revolution 70, ingress.

## 4.6 Results

Attenuation results are shown in Figures 4.19 through 4.30. Displayed are the individual profiles for phosphine, ammonia, refractive defocusing and the sum of these three. The aggregate is the total absorption experienced and the pressure on the graphs indicates the layer where the signal to noise ratio (SNR) at the receiving station is less than or equal to 3 dB which will be referred to as the loss of signal point (LOS). The free space signal to noise ratios at the receiving DSN antennas depend on Earth and Saturn ephemerides as well as the weather at the time of a given experiment. The typical values are 39 dB-Hz for S-band, 51 dB-Hz for X-band and 41 dB-Hz for Ka-band where a one second integration time is used. As the signal to noise ratio drops to 3 dB or less the ability of the DSN to detect the signal degrades. At this point the signal is considered to be lost and no discernible data can be retrieved. Tables 4.1 to 4.4 lists the results for orbits 7 and 70 of the loss of signal point ($\leq$ 3 dB) as well as the 3 dB and 6 dB points at the three experimental frequencies. See Appendix B for the results of orbits 51 and 54.

Table 4.1: Revolution 7 ingress. Loss of signal point, 3 dB and 6 dB points.

| | **S** | **X** | **Ka** |
|---|---|---|---|
| SNR ≤ 3 dB | 1.40 bars | 1.06 bars | 0.82 bar |
| SNR > 3 dB | 1.36 bars | 1.02 bars | 0.79 bar |
| SNR > 6 dB | 1.31 bars | 1.02 bars | 0.75 bar |

Table 4.2: Revolution 7 egress. Loss of signal point, 3 dB and 6 dB points.

| | **S** | **X** | **Ka** |
|---|---|---|---|
| SNR ≤ 3 dB | 1.36 bars | 1.06 bars | 0.82 bar |
| SNR > 3 dB | 1.31 bars | 1.02 bars | 0.79 bar |
| SNR > 6 dB | 1.31 bars | 1.02 bars | 0.75 bar |

Table 4.3: Revolution 70 ingress. Loss of signal point, 3 dB and 6 dB points.

| | **S** | **X** | **Ka** |
|---|---|---|---|
| SNR ≤ 3 dB | 1.40 bars | 1.09 bars | 0.82 bar |
| SNR > 3 dB | 1.36 bars | 1.06 bars | 0.79 bar |
| SNR > 6 dB | 1.31 bars | 1.02 bars | 0.79 bar |

Table 4.4: Revolution 70 egress. Loss of signal point, 3 dB and 6 dB points.

| | **S** | **X** | **Ka** |
|---|---|---|---|
| SNR ≤ 3 dB | 1.40 bars | 1.06 bars | 0.82 bar |
| SNR > 3 dB | 1.36 bars | 1.02 bars | 0.79 bar |
| SNR > 6 dB | 1.31 bars | 1.02 bars | 0.75 bar |

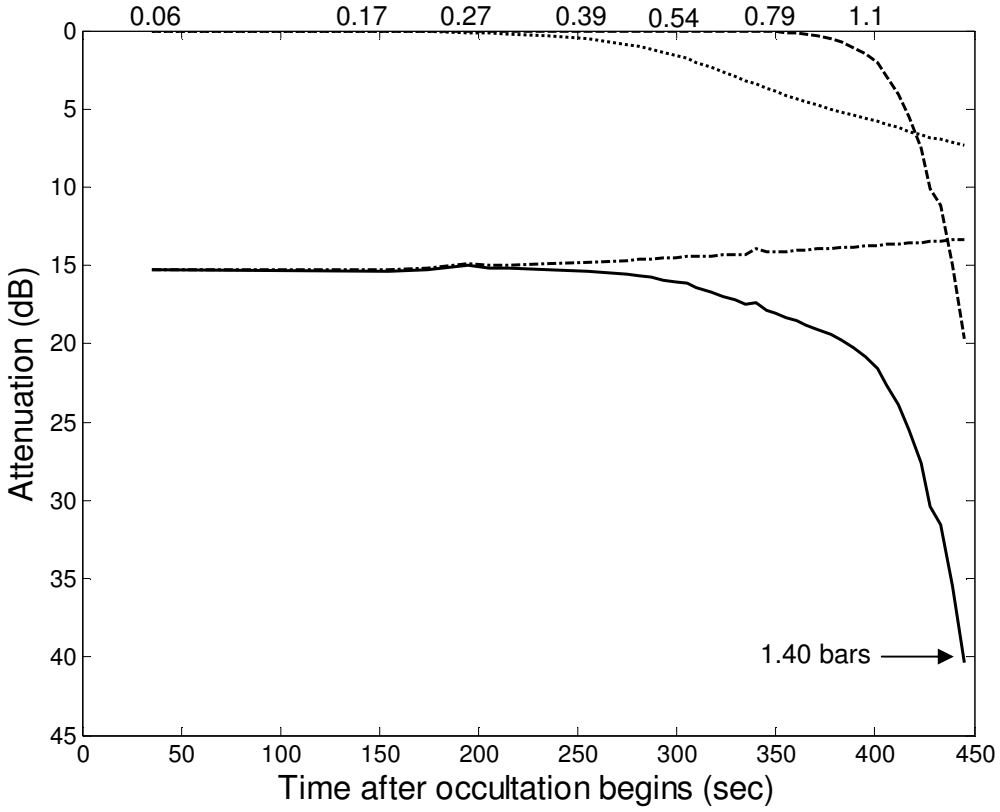


Figure 4.19: Revolution 7, ingress at S-band. S-band free space SNR is 39 dB and LOS occurs at a pressure of 1.40 bars. The dashed line is the absorption due to ammonia, the dotted line is the absorption due to phosphine, the dotted dashed line is refractive defocusing and the solid line is the aggregate. The pressure in bars is indicated at various points in time at the top of the graph but is not to scale.

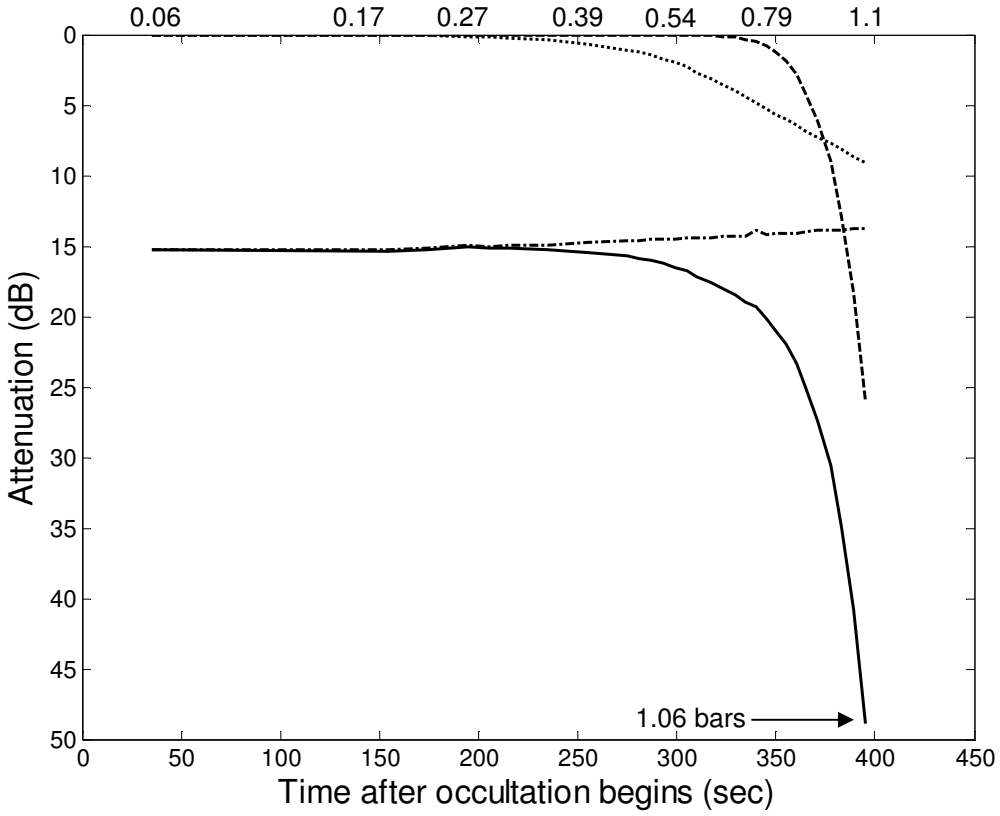


Figure 4.20: Revolution 7, ingress at X-band. X-band free space SNR is 51 dB and LOS occurs at a pressure of 1.06 bars. The dashed line is the absorption due to ammonia, the dotted line is the absorption due to phosphine, the dotted dashed line is refractive defocusing and the solid line is the aggregate. The pressure is indicated at various points in time at the top of the graph but is not to scale.

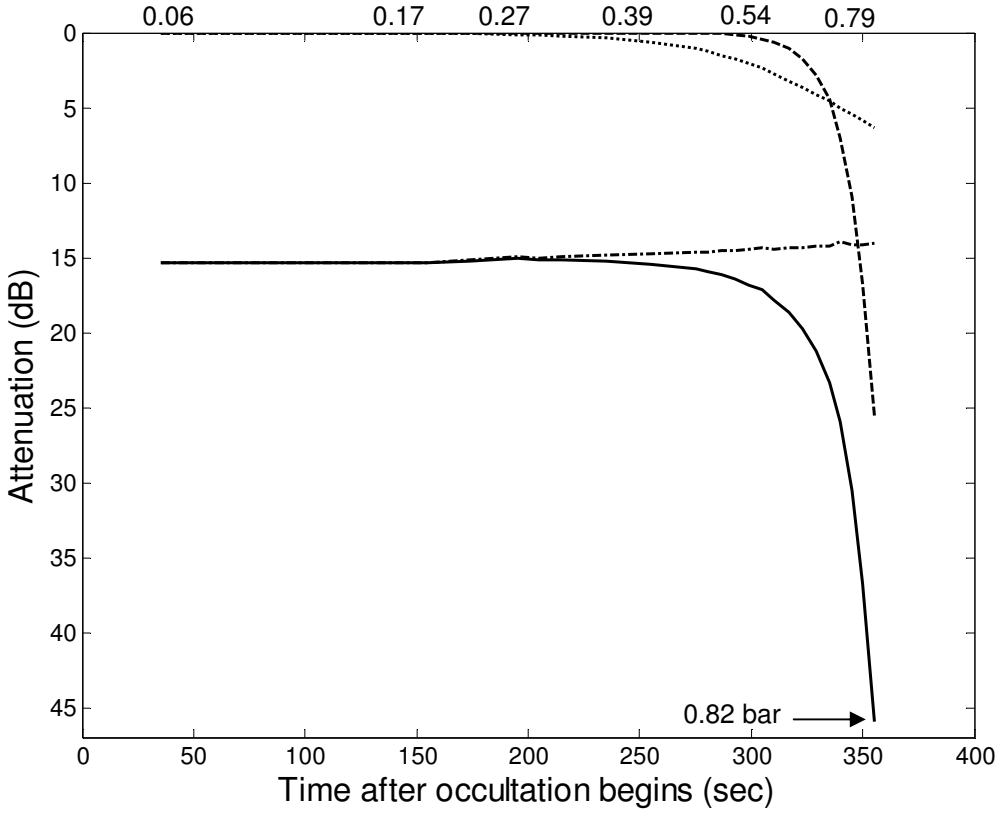


Figure 4.21: Revolution 7, ingress at Ka-band. Ka-band free space SNR is 41 dB and LOS occurs at a pressure of 0.82 bar. The dashed line is the absorption due to ammonia, the dotted line is the absorption due to phosphine, the dotted dashed line is refractive defocusing and the solid line is the aggregate. The pressure is indicated at various points in time at the top of the graph but is not to scale.

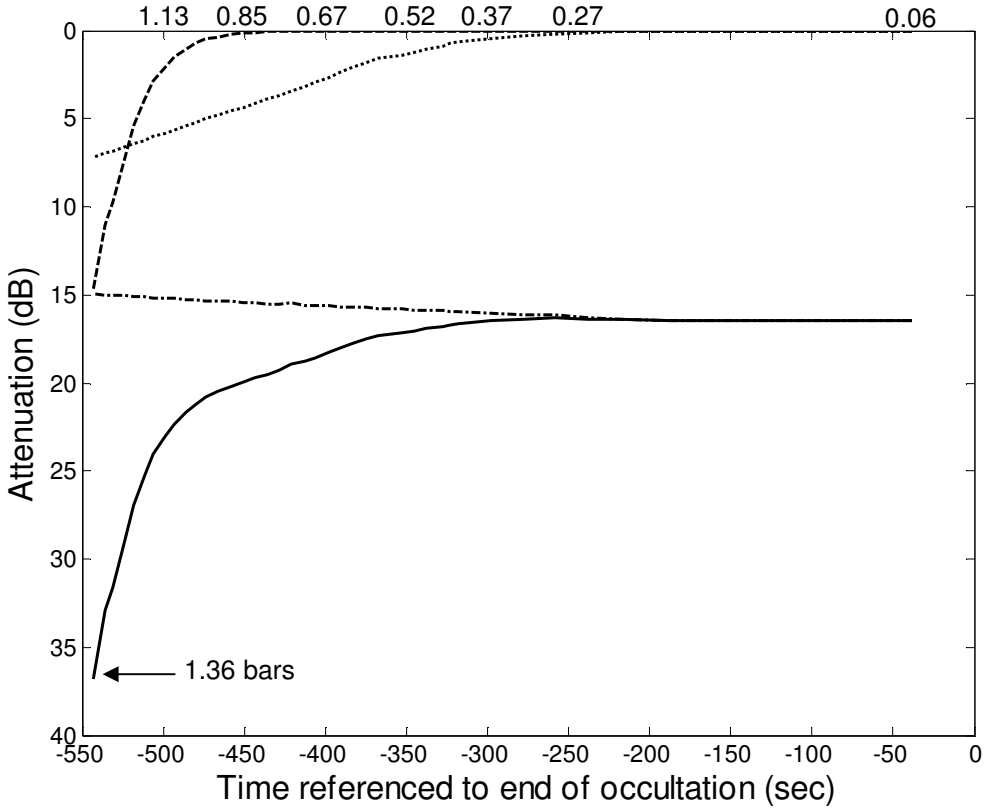


Figure 4.22: Revolution 7, egress at S-band. S-band free space SNR is 39 dB and LOS occurs at a pressure of 1.36 bars. The dashed line is the absorption due to ammonia, the dotted line is the absorption due to phosphine, the dotted dashed line is refractive defocusing and the solid line is the aggregate. The pressure is indicated at various points in time at the top of the graph but is not to scale.

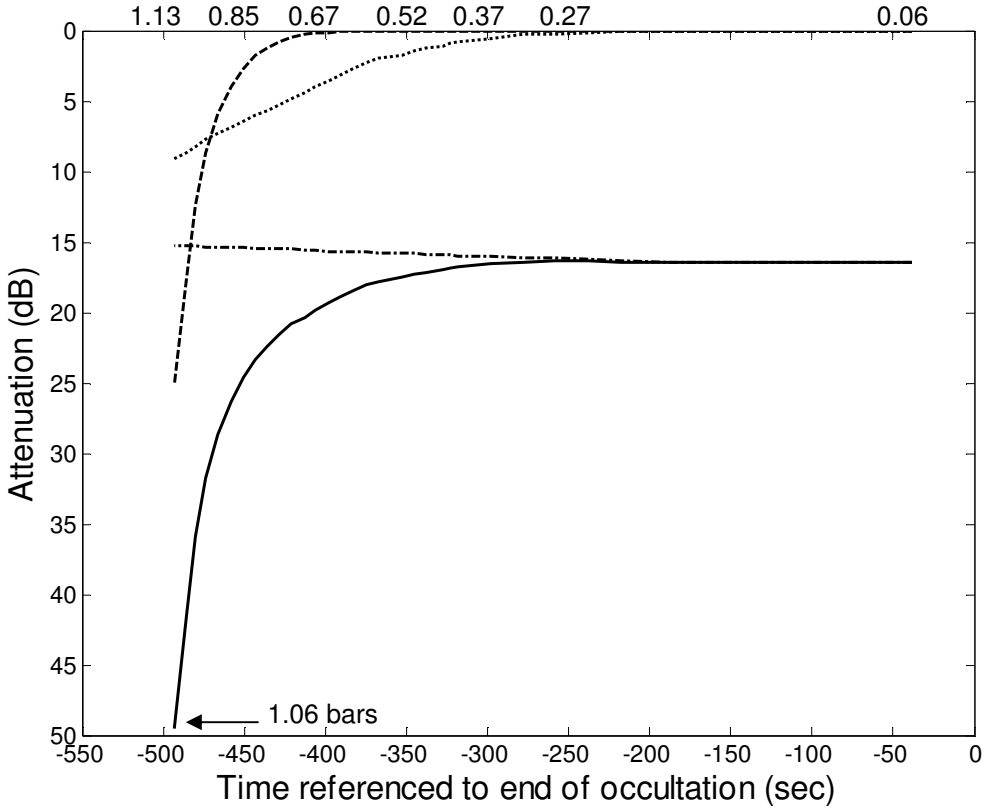


Figure 4.23: Revolution 7, egress at X-band. X-band free space SNR is 51 dB and LOS occurs at a pressure of 1.06 bars. The dashed line is the absorption due to ammonia, the dotted line is the absorption due to phosphine, the dotted dashed line is refractive defocusing and the solid line is the aggregate. The pressure is indicated at various points in time at the top of the graph but is not to scale.

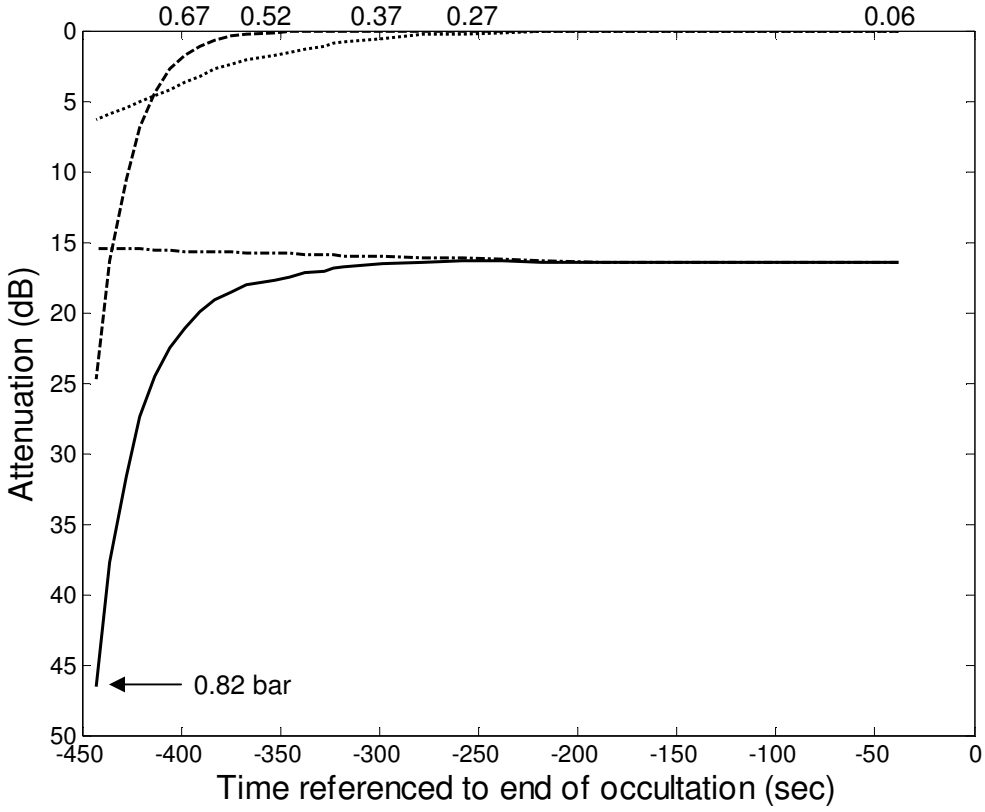


Figure 4.24: Revolution 7, egress at Ka-band. Ka-band free space SNR is 41 dB and LOS occurs at a pressure of 0.82 bar. The dashed line is the absorption due to ammonia, the dotted line is the absorption due to phosphine, the dotted dashed line is refractive defocusing and the solid line is the aggregate. The pressure is indicated at various points in time at the top of the graph but is not to scale.

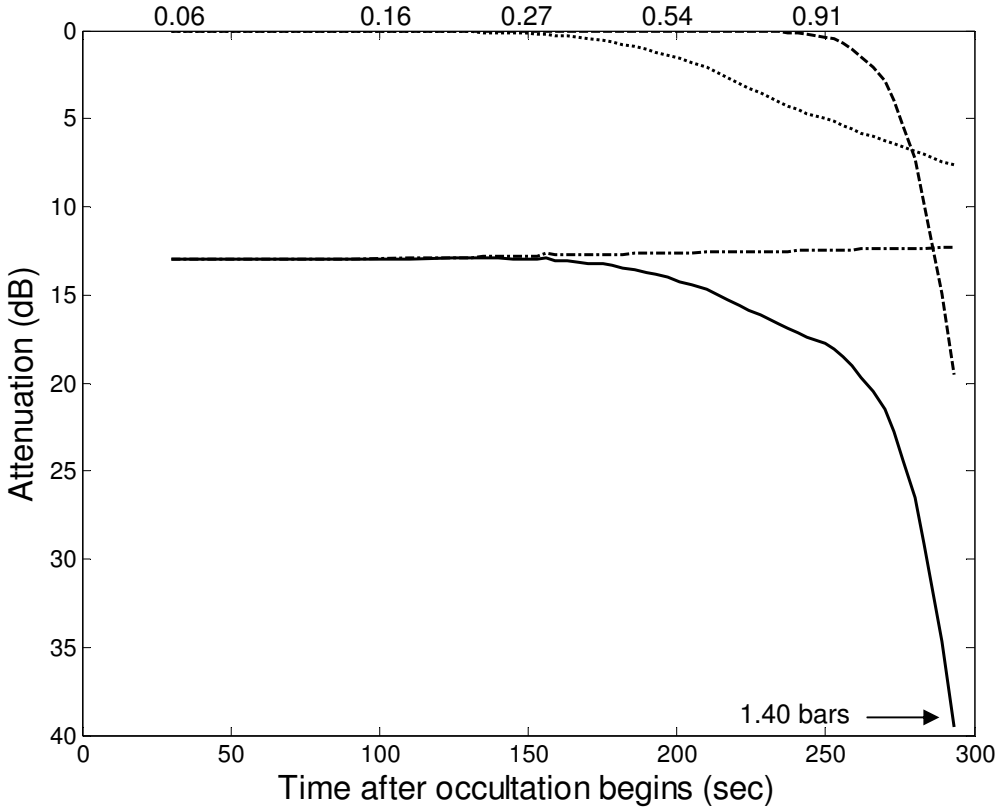


Figure 4.25: Revolution 70, ingress at S-band. S-band free space SNR is 39 dB and LOS occurs at a pressure of 1.40 bars. The dashed line is the absorption due to ammonia, the dotted line is the absorption due to phosphine, the dotted dashed line is refractive defocusing and the solid line is the aggregate. The pressure is indicated at various points in time at the top of the graph but is not to scale.

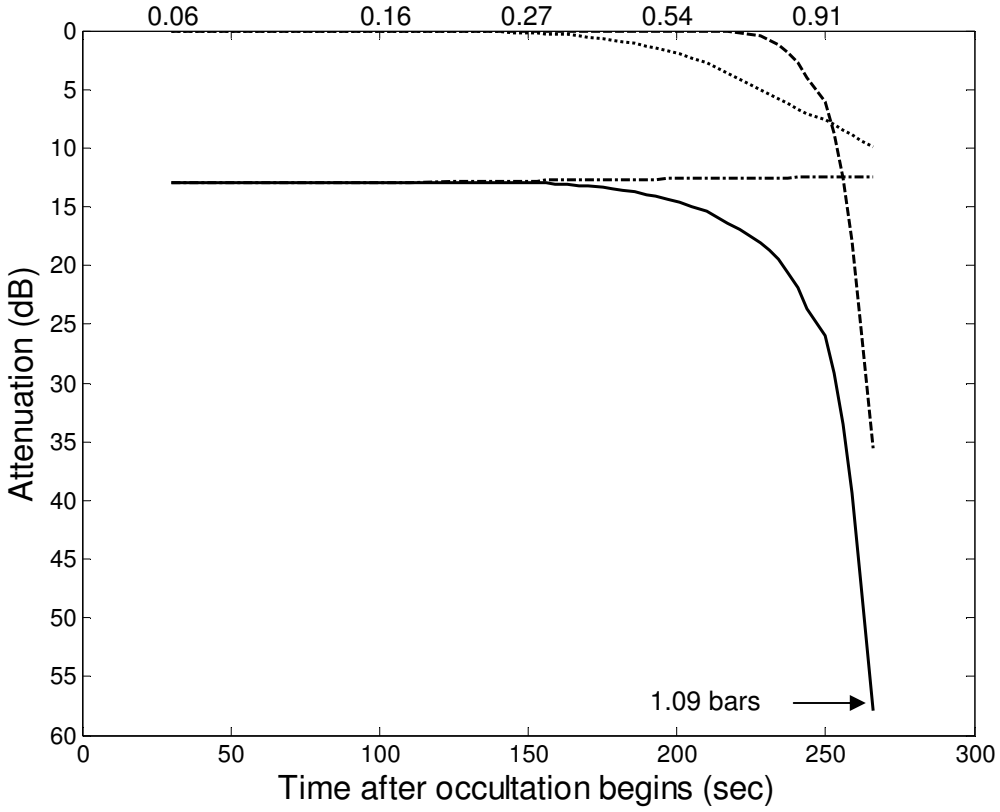


Figure 4.26: Revolution 70, ingress at X-band. X-band free space SNR is 51 dB and LOS occurs at a pressure of 1.09 bars. The dashed line is the absorption due to ammonia, the dotted line is the absorption due to phosphine, the dotted dashed line is refractive defocusing and the solid line is the aggregate. The pressure is indicated at various points in time at the top of the graph but is not to scale.

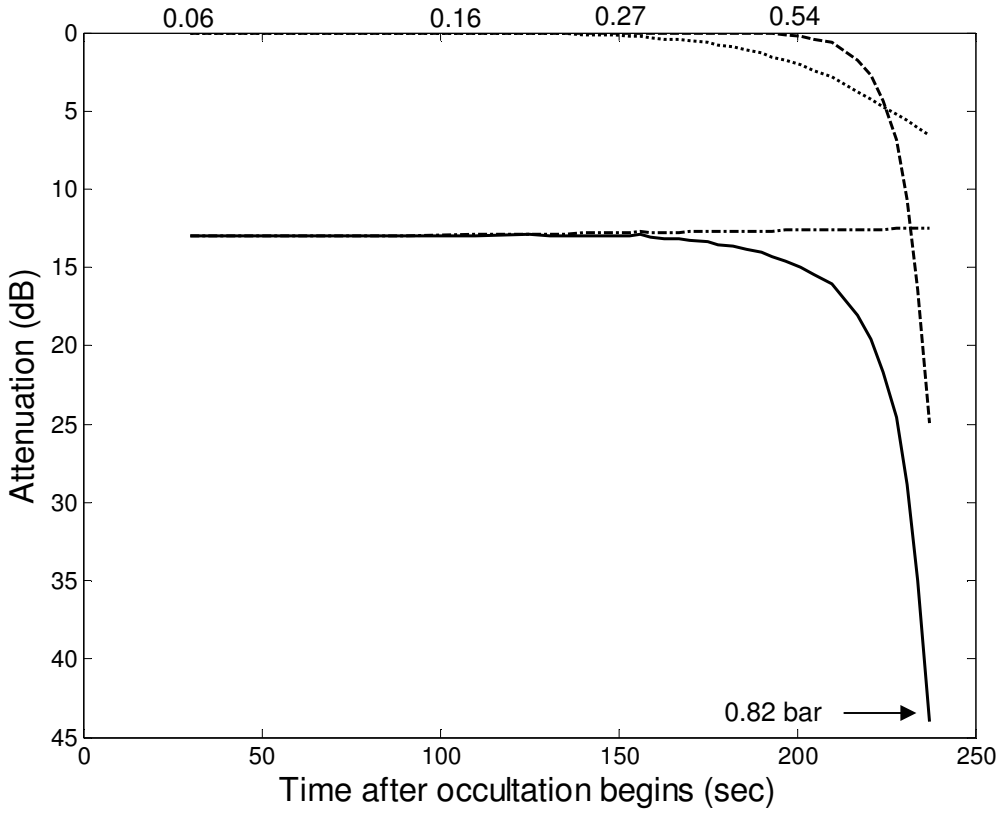


Figure 4.27: Revolution 70, ingress at Ka-band. Ka-band free space SNR is 41 dB and LOS occurs at a pressure of 0.82 bars. The dashed line is the absorption due to ammonia, the dotted line is the absorption due to phosphine, the dotted dashed line is refractive defocusing and the solid line is the aggregate. The pressure is indicated at various points in time at the top of the graph but is not to scale.

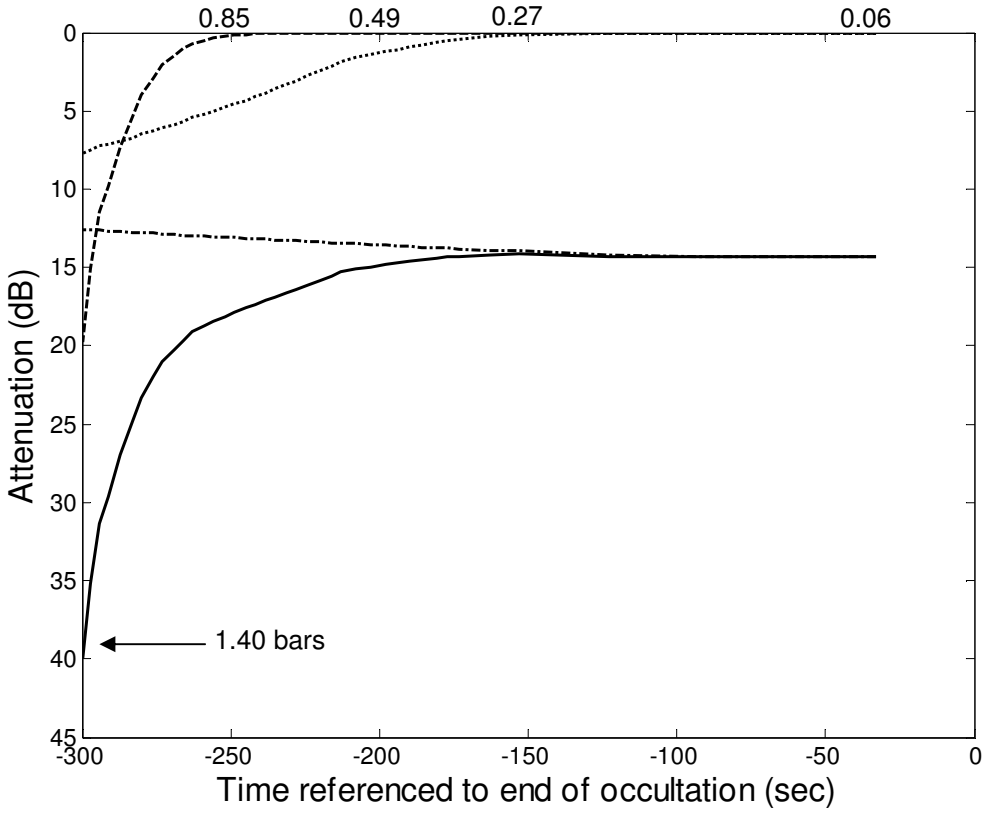


Figure 4.28: Revolution 70, egress at S-band. S-band free space SNR is 39 dB and LOS occurs at a pressure of 1.40 bars. The dashed line is the absorption due to ammonia, the dotted line is the absorption due to phosphine, the dotted dashed line is refractive defocusing and the solid line is the aggregate. The pressure is indicated at various points in time at the top of the graph but is not to scale.

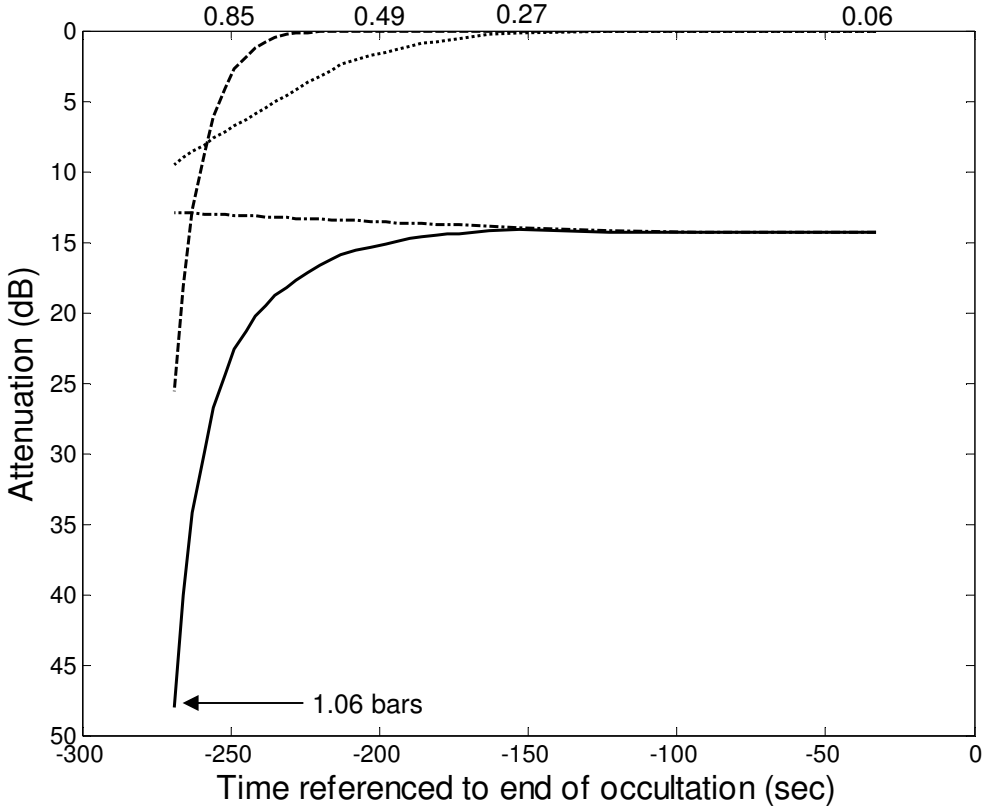


Figure 4.29: Revolution 70, egress at X-band. X-band free space SNR is 51 dB and LOS occurs at a pressure of 1.06 bars. The dashed line is the absorption due to ammonia, the dotted line is the absorption due to phosphine, the dotted dashed line is refractive defocusing and the solid line is the aggregate. The pressure is indicated at various points in time at the top of the graph but is not to scale.

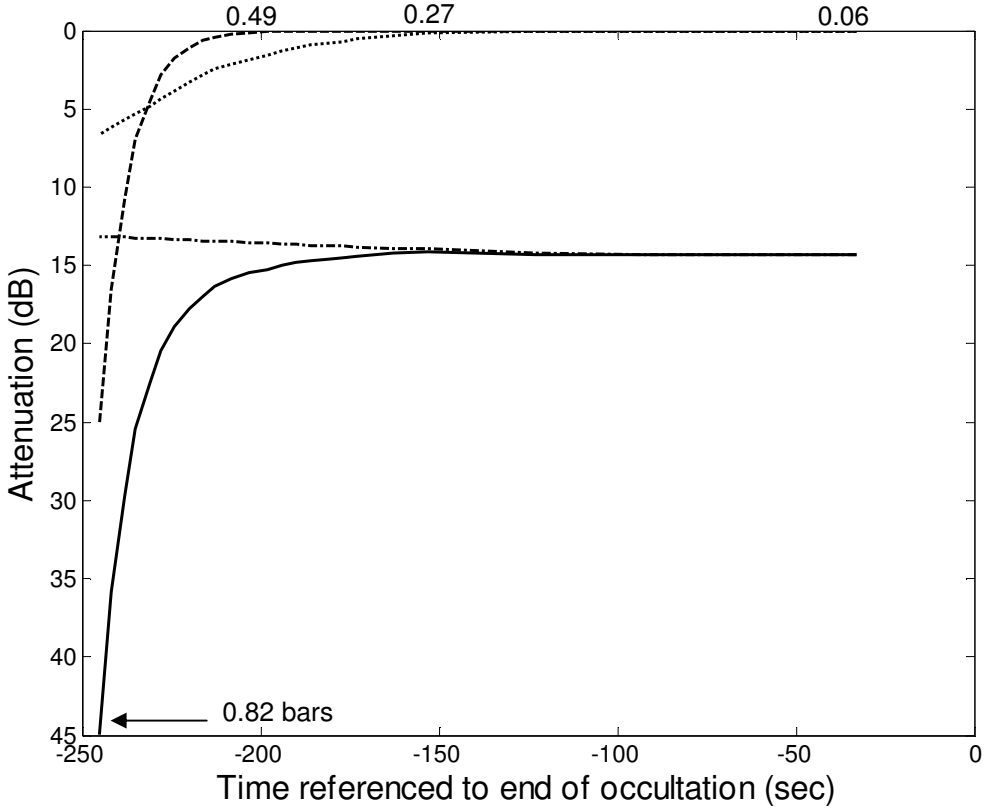


Figure 4.30: Revolution 70, egress at Ka-band. Ka-band free space SNR is 41 dB and LOS occurs at a pressure of 0.82 bars. The dashed line is the absorption due to ammonia, the dotted line is the absorption due to phosphine, the dotted dashed line is refractive defocusing and the solid line is the aggregate. The pressure is indicated at various points in time at the top of the graph but is not to scale.

## 4.7 Profiling Phosphine and Ammonia at Saturn

As discussed in section 4.1, equations 4.7 and 4.8 can be used to retrieve vertical profiles of absorptivity of the microwave absorbing constituents. Using Ka-band, measurable absorption of phosphine will be detected unambiguously at about 0.41 bar until about 0.62 bar where absorption by ammonia will become noticeable. The Ka-band signal can be used to profile ammonia and phosphine until about 0.79 bar where the signal will not be detectable. The use of dual frequency experiments can discriminate between phosphine and ammonia at a given level since the frequency dependence of the absorptivity of each constituent is different. The use of a third frequency can help verify the suitability of the model for ammonia absorption employed in the retrieval. The X-band signal can be used to determine phosphine abundance from about 0.41 bar to 0.75 bar where ammonia will be detected and the corresponding pressure levels for S-band are 0.43 bar and 0.98 bar. The deepest level probed will be by S-band at about 1.36 bars but spectral discrimination is lost at about 1.06 bars where X-band will no longer detected and Ka-band is lost at an even lower pressure (higher altitude) of 0.79 bar.

# CHAPTER 5

# SUMMARY AND CONCLUSIONS

The work described in this dissertation has a fundamental impact on millimeter-wave remote sensing of the atmospheres of the outer planets.

## 5.1 Absorption of Phosphine and Ammonia at Ka-band

The results of our laboratory measurements for the opacity of phosphine in a hydrogen/helium atmosphere agree well with the formalism by Hoffman *et al.* (2001), which uses a Van Vleck-Weisskopf lineshape. However, no existing formalism for the opacity of ammonia in a hydrogen/helium atmosphere, accurately describes the absorption measured in the laboratory at Ka-band (7.5 mm to 9.2 mm) to the precision of our measurement system. A new formalism has been developed using a modified Ben-Reuven lineshape. While theory predicts that there should be a smooth transition from the Ben-Reuven lineshape to the Van Vleck-Weisskopf lineshape at low pressures, the data clearly shows that the Van Vleck-Weisskopf lineshape is not appropriate for ammonia under these conditions and that the Ben-Reuven lineshape is preferable over the pressure and temperature range to be encountered by the Cassini Ka-band radio occultation experiments.

## 5.2 Absorption of Phosphine and Ammonia at W-band

The results of our laboratory measurements for the opacity of phosphine in a hydrogen/helium atmosphere agree well with the formalism by Hoffman *et al.* (2001), which uses a Van Vleck-Weisskopf lineshape. However, no existing formalism for the

opacity of ammonia in a hydrogen/helium atmosphere, accurately describes the measured absorption at 94 GHz (3.2 mm) at pressures greater than 1 bar. A new formalism has been developed using a Ben-Reuven lineshape for the inversion lines and a Kinetic lineshape for the rotational lines. It should be noted that the model presented in this paper which is most suitable for use at W-band (2.7 – 4 mm), is different from the model presented by Mohammed and Steffes (2003) for use at Ka-band (7.5 – 9.2 mm). Other models such as those from Berge and Gulkis (1976), or Spilker (1990) are better for use at centimeter wavelengths.

The larger linewidth parameters used in the new model for the first rotational line of ammonia will be further verified by conducting additional measurements of ammonia over an extended range of millimeter and submillimeter wavelengths, so as to verify the usefulness of the new model at wavelengths less than 3 mm. These measurements, will play a significant role in creating a unified model which could accurately predict the opacity of ammonia in a hydrogen/helium atmosphere over a wide range of pressures, temperatures, mixing ratios and wavelengths (frequencies) ranging from 1.5 mm (200 GHz) to 0.3 m (1 GHz). Unfortunately, a unified model for ammonia opacity is currently unavailable, and the different wavelength ranges have to be treated independently. However, an extensive program of additional laboratory measurements will likely resolve this shortcoming. The new data will aid in creating opacity formalisms for use over a broader spectrum.

## 5.3 Application of Laboratory Measurements to Radio Occultation

A radio occultation simulator was developed to predict temporal absorption and excess Doppler profiles due to Saturn's atmosphere for the three-frequency radio occultation experiments, to be conducted using the Cassini orbiter. The simulator used a ray tracing technique which accounted for the oblateness of the planet. The results show that the Ka-band signal will be the first to detect ammonia at 0.62 bar and the first to be lost at 0.79 bar followed by the loss of X-band at 1.02 bars and S-band at 1.36 bars. Ka-band and X-band will first detect phosphine at 0.41 bar and both phosphine and ammonia can be profiled to about 1.02 bars. The attenuation profiles were derived using the model for phosphine absorption described in Hoffman *et. al* (2001) at all frequencies, in addition to the newest model for ammonia absorption at Ka-band described in Chapter 2 and the Berge and Gulkis (Berge and Gulkis, 1976) model for ammonia absorption at S and X-bands.

It was demonstrated that the use of the center of the planet as the center of refraction to determine refractive defocusing can result in an error of about 1 to 2 dB. Since Saturn is modeled as an oblate spheroid, the center of refraction is offset from the center of the planet. Using the ray asymptotes found from ray tracing as well as parameters defined in Ahmad and Tyler (1999), the new center for the planet, which changes at each point in time, was calculated and the refractive defocusing was computed in reference to the new center.

## 5.4 Direction for Future Studies

### 5.4.1 Laboratory Studies

Currently there are several models which describe the opacity of ammonia in a hydrogen/ helium atmosphere under conditions characteristic of the outer planets, with each model being suitable for a particular frequency interval. The work in this thesis illustrates the need for additional laboratory measurements of ammonia in the 100-300 GHz (1-3 mm) range to verify the usefulness of the model described in Chapter 3 for this frequency (wavelength) range. Also the opacity predicted by each model differs at 27 GHz (1.1 cm), a frequency which has been used to model Jupiter's deep atmosphere (see e.g. de Pater *et. al* 2005 and Janssen *et. al* 2005). An extensive program of additional laboratory measurements will aid in creating a formalism to predict opacity of ammonia in a hydrogen/helium atmosphere for use over a broader spectrum.

### 5.4.2 Refractive Defocusing of the Oblate Planets

The refractive defocusing calculated in section 4.5 uses a method for finding the new center of refraction using the parameters described in Ahmad and Tyler (1999) for an atmosphere with large scale departure from spherical symmetry. Kliore and Woiceshyn (1976) use another method to calculate the center of refraction to retrieve data from radio occultation experiments conducted at Jupiter (also an oblate planet) by Pioneer 10 and 11. Their method makes use of the shape of the planet to compute the new center of refraction. It would be useful to determine the resulting difference in refractive defocusing using these methods.

## 5.5 Uniqueness and Contributions

The objectives of this thesis have been to measure the millimeter-wavelength opacity of phosphine and ammonia under simulated conditions for the outer planets, to determine suitable formalisms to describe ammonia and phosphine absorption and to apply these results so as to predict the sensitivity of the Cassini radio occultation experiments to these constituents. Laboratory measurements of phosphine in a hydrogen/helium atmosphere were never conducted at Ka-band (32-40 GHz) or at W-band (94 GHz). Also measurements of ammonia, in a hydrogen/helium atmosphere at these frequencies, were never obtained to the precision of that shown in Chapters 2 and 3. Included in the error analysis for the first time were effects of the uncertainties in temperature and pressure due to the laboratory measurement devices which were then mapped back to an equivalent error in opacity and included in the error bars.

The radio occultation simulator described in Chapter 4 is the first such model for an oblate planet. It also incorporates calculations for refractive defocusing considering the issue of oblateness.

## 5.6 Publications and Presentations

**Refereed Journal Publications:**

P.N. Mohammed and P.G. Steffes, 2004. Laboratory measurements of the W-band (3.2 mm) properties of phosphine ($PH_3$) and ammonia ($NH_3$) under simulated conditions for the outer planets. *Journal of Geophysical Research*, **109, E07S13**, 1-9.

P.N. Mohammed and P.G. Steffes, 2003. Laboratory measurements of the Ka-band (7.5mm to 9.2mm) opacity of phosphine ($PH_3$) and ammonia ($NH_3$) under simulated conditions for the Cassini-Saturn encounter. *Icarus*, **166**, 425-435.

**Presentations with Published Proceedings:**

P.N. Mohammed and P. G. Steffes, 2004. Simulations of the Cassini Radio Occultation Experiments for the Atmosphere of Saturn Based on Recent Laboratory Measurements. *Bulletin of the American Astronomical Society*, vol. **36**, no. 4, 2004, p.1107. Presented at the 36th Annual Meeting of the Division for Planetary Sciences of the American Astronomical Society, Louisville, KY, November 9, 2004.

P.N. Mohammed and P.G. Steffes, 2003. Laboratory Measurements of the W-band (3.2 mm) Properties of Phosphine ($PH_3$) and Ammonia ($NH_3$) Under Simulated Conditions for the Outer Planets. *Bulletin of the American Astronomical Society*, vol. **35**, no. 3, 2003, p.713. Presented at the 35th Annual Meeting of the Division for Planetary Sciences of the American Astronomical Society, Monterey, CA, September 2, 2003.

P.N. Mohammed and P.G. Steffes, 2002. Laboratory Measurements of the Ka-band (7.5mm to 9.2 mm) Opacity of Phosphine ($PH_3$) and Ammonia ($NH_3$) Under Simulated Conditions for the Cassini-Saturn Encounter. *Bulletin of the American*

*Astronomical Society*, vol. **34**, no. 3, 2002, p.910. Presented at the 34th Annual Meeting of the Division for Planetary Sciences of the American Astronomical Society, Birmingham, AL, October 11, 2002.

P.G. Steffes and P.N. Mohammed, 2002. Study of Cassini Radio Occultation Sensitivity to Atmospheric Constituents Based on New Laboratory Measurements. *Bulletin of the American Astronomical Society*, vol **34**, no. 3, 2002, p.910. Presented at the 34th Annual Meeting of the Division for Planetary Sciences of the American Astronomical Society, Birmingham, AL, October 11, 2002.

P.N. Mohammed and P.G. Steffes, 2001. Preliminary Laboratory Measurements of the Millimeter Wavelength Properties of Phosphine ($PH_3$) under Simulated Outer Planet Conditions. *Bulletin of the American Astronomical Society*, vol. **33**, no. 3, 2001, p. 1141. Presented at the 33rd Annual Meeting of the Division for Planetary Sciences of the American Astronomical Society, New Orleans, LA, December 1, 2001.

**Presentations:**

P.N. Mohammed and P. G. Steffes, 2003. Laboratory measurements of the Ka-band (7.5 to 9.2 mm) opacity of $PH_3$ and $NH_3$ under simulated conditions for the Cassini-Saturn encounter. *Cassini Radio Science Team Meeting*, Jet Propulsion Laboratory, Pasadena, CA, February 1, 2003.

## APPENDIX A

## TEMPERATURE-PRESSURE PROFILE OF SATURN

Table A.1: Temperature-Pressure Profile of Saturn

| Pressure (bar) | Temperature (Kelvin) | Equatorial Radius (km) | Polar Radius (km) |
|---|---|---|---|
| 70.000000 | 492.1510 | 59789 | 53924.30 |
| 69.292100 | 490.6800 | 59791 | 53926.10 |
| 68.589200 | 489.2080 | 59793 | 53927.90 |
| 67.891500 | 487.7360 | 59795 | 53929.71 |
| 67.198900 | 486.2640 | 59797 | 53931.51 |
| 66.511500 | 484.7930 | 59799 | 53933.32 |
| 65.829000 | 483.3220 | 59801 | 53935.12 |
| 65.151700 | 481.8510 | 59803 | 53936.92 |
| 64.479400 | 480.3800 | 59805 | 53938.73 |
| 63.812100 | 478.9090 | 59807 | 53940.53 |
| 63.149700 | 477.4390 | 59809 | 53942.34 |
| 62.492400 | 475.9690 | 59811 | 53944.14 |
| 61.839900 | 474.4980 | 59813 | 53945.94 |
| 61.192400 | 473.0290 | 59815 | 53947.75 |
| 60.549800 | 471.5590 | 59817 | 53949.55 |
| 59.912000 | 470.0890 | 59819 | 53951.35 |
| 59.279100 | 468.6200 | 59821 | 53953.16 |
| 58.651000 | 467.1510 | 59823 | 53954.96 |
| 58.027700 | 465.6820 | 59825 | 53956.77 |
| 57.409200 | 464.2130 | 59827 | 53958.57 |
| 56.795400 | 462.7450 | 59829 | 53960.37 |
| 56.186400 | 461.2760 | 59831 | 53962.18 |
| 55.582100 | 459.8080 | 59833 | 53963.98 |
| 54.982400 | 458.3400 | 59835 | 53965.78 |
| 54.387400 | 456.8720 | 59837 | 53967.59 |
| 53.797100 | 455.4050 | 59839 | 53969.39 |
| 53.211400 | 453.9370 | 59841 | 53971.20 |
| 52.630300 | 452.4700 | 59843 | 53973.00 |
| 52.053700 | 451.0030 | 59845 | 53974.80 |
| 51.481700 | 449.5360 | 59847 | 53976.61 |
| 50.914200 | 448.0690 | 59849 | 53978.41 |
| 50.351300 | 446.6020 | 59851 | 53980.22 |
| 49.792800 | 445.1360 | 59853 | 53982.02 |
| 49.238700 | 443.6700 | 59855 | 53983.82 |
| 48.689200 | 442.2040 | 59857 | 53985.63 |
| 48.144000 | 440.7380 | 59859 | 53987.43 |

Table A.1 continued

| | | | |
|---|---|---|---|
| 47.603200 | 439.2720 | 59861 | 53989.23 |
| 47.066800 | 437.8070 | 59863 | 53991.04 |
| 46.534800 | 436.3410 | 59865 | 53992.84 |
| 46.007000 | 434.8760 | 59867 | 53994.65 |
| 45.483600 | 433.4110 | 59869 | 53996.45 |
| 44.964500 | 431.9460 | 59871 | 53998.25 |
| 44.449600 | 430.4810 | 59873 | 54000.06 |
| 43.939000 | 429.0170 | 59875 | 54001.86 |
| 43.432600 | 427.5520 | 59877 | 54003.67 |
| 42.930400 | 426.0880 | 59879 | 54005.47 |
| 42.432300 | 424.6240 | 59881 | 54007.27 |
| 41.938500 | 423.1600 | 59883 | 54009.08 |
| 41.448700 | 421.6970 | 59885 | 54010.88 |
| 40.963100 | 420.2330 | 59887 | 54012.68 |
| 40.481600 | 418.7700 | 59889 | 54014.49 |
| 40.004100 | 417.3070 | 59891 | 54016.29 |
| 39.530700 | 415.8440 | 59893 | 54018.10 |
| 39.061300 | 414.3810 | 59895 | 54019.90 |
| 38.595900 | 412.9180 | 59897 | 54021.70 |
| 38.134500 | 411.4560 | 59899 | 54023.51 |
| 37.677100 | 409.9930 | 59901 | 54025.31 |
| 37.223600 | 408.5310 | 59903 | 54027.11 |
| 36.774000 | 407.0690 | 59905 | 54028.92 |
| 36.328300 | 405.6070 | 59907 | 54030.72 |
| 35.886600 | 404.1450 | 59909 | 54032.53 |
| 35.448600 | 402.6840 | 59911 | 54034.33 |
| 35.014500 | 401.2220 | 59913 | 54036.13 |
| 34.584300 | 399.7610 | 59915 | 54037.94 |
| 34.157800 | 398.3000 | 59917 | 54039.74 |
| 33.735100 | 396.8390 | 59919 | 54041.55 |
| 33.316100 | 395.3780 | 59921 | 54043.35 |
| 32.900900 | 393.9170 | 59923 | 54045.15 |
| 32.489400 | 392.4570 | 59925 | 54046.96 |
| 32.081600 | 390.9960 | 59927 | 54048.76 |
| 31.677500 | 389.5360 | 59929 | 54050.56 |
| 31.277100 | 388.0760 | 59931 | 54052.37 |
| 30.880200 | 386.6160 | 59933 | 54054.17 |
| 30.487000 | 385.1560 | 59935 | 54055.98 |
| 30.097400 | 383.6960 | 59937 | 54057.78 |
| 29.711300 | 382.2370 | 59939 | 54059.58 |
| 29.328800 | 380.7780 | 59941 | 54061.39 |
| 28.949800 | 379.3180 | 59943 | 54063.19 |
| 28.574400 | 377.8590 | 59945 | 54064.99 |
| 28.202400 | 376.4000 | 59947 | 54066.80 |
| 27.833900 | 374.9410 | 59949 | 54068.60 |
| 27.468800 | 373.4830 | 59951 | 54070.41 |

Table A.1 continued

| | | | |
|---|---|---|---|
| 27.107200 | 372.0240 | 59953 | 54072.21 |
| 26.749000 | 370.5660 | 59955 | 54074.01 |
| 26.394200 | 369.1080 | 59957 | 54075.82 |
| 26.042800 | 367.6490 | 59959 | 54077.62 |
| 25.694700 | 366.1910 | 59961 | 54079.43 |
| 25.350000 | 364.7340 | 59963 | 54081.23 |
| 25.008500 | 363.2760 | 59965 | 54083.03 |
| 24.670400 | 361.8180 | 59967 | 54084.84 |
| 24.335500 | 360.3610 | 59969 | 54086.64 |
| 24.003900 | 358.9030 | 59971 | 54088.44 |
| 23.675600 | 357.4460 | 59973 | 54090.25 |
| 23.350400 | 355.9890 | 59975 | 54092.05 |
| 23.028500 | 354.5320 | 59977 | 54093.86 |
| 22.709700 | 353.0750 | 59979 | 54095.66 |
| 22.394100 | 351.6190 | 59981 | 54097.46 |
| 22.081600 | 350.1620 | 59983 | 54099.27 |
| 21.772300 | 348.7060 | 59985 | 54101.07 |
| 21.466000 | 347.2490 | 59987 | 54102.88 |
| 21.162900 | 345.7930 | 59989 | 54104.68 |
| 20.862800 | 344.3370 | 59991 | 54106.48 |
| 20.565700 | 342.8810 | 59993 | 54108.29 |
| 20.271700 | 341.4250 | 59995 | 54110.09 |
| 19.980700 | 339.9690 | 59997 | 54111.89 |
| 19.692600 | 338.5130 | 59999 | 54113.7 |
| 19.407600 | 337.0580 | 60001 | 54115.5 |
| 19.125500 | 335.6030 | 60003 | 54117.31 |
| 18.846300 | 334.1470 | 60005 | 54119.11 |
| 18.570100 | 332.6920 | 60007 | 54120.91 |
| 18.296700 | 331.2370 | 60009 | 54122.72 |
| 18.026200 | 329.7820 | 60011 | 54124.52 |
| 17.758600 | 328.3270 | 60013 | 54126.32 |
| 17.493800 | 326.8720 | 60015 | 54128.13 |
| 17.231800 | 325.4180 | 60017 | 54129.93 |
| 16.972700 | 323.9630 | 60019 | 54131.74 |
| 16.716300 | 322.5080 | 60021 | 54133.54 |
| 16.462700 | 321.0540 | 60023 | 54135.34 |
| 16.211900 | 319.6000 | 60025 | 54137.15 |
| 15.963800 | 318.1460 | 60027 | 54138.95 |
| 15.718300 | 316.6910 | 60029 | 54140.76 |
| 15.475600 | 315.2370 | 60031 | 54142.56 |
| 15.235600 | 313.7840 | 60033 | 54144.36 |
| 14.998200 | 312.3240 | 60035 | 54146.17 |
| 14.763500 | 310.8650 | 60037 | 54147.97 |
| 14.531400 | 309.4060 | 60039 | 54149.77 |
| 14.301900 | 307.9470 | 60041 | 54151.58 |
| 14.074900 | 306.4880 | 60043 | 54153.38 |

Table A.1 continued

| | | | |
|---|---|---|---|
| 13.850600 | 305.0290 | 60045 | 54155.19 |
| 13.628800 | 303.5700 | 60047 | 54156.99 |
| 13.409500 | 302.1100 | 60049 | 54158.79 |
| 13.192700 | 300.6500 | 60051 | 54160.60 |
| 12.978500 | 299.1900 | 60053 | 54162.40 |
| 12.766700 | 297.7300 | 60055 | 54164.21 |
| 12.557300 | 296.2690 | 60057 | 54166.01 |
| 12.350400 | 294.8080 | 60059 | 54167.81 |
| 12.146000 | 293.3470 | 60061 | 54169.62 |
| 11.943900 | 291.8850 | 60063 | 54171.42 |
| 11.744300 | 290.4220 | 60065 | 54173.22 |
| 11.547000 | 288.9590 | 60067 | 54175.03 |
| 11.352100 | 287.4960 | 60069 | 54176.83 |
| 11.159500 | 286.0320 | 60071 | 54178.64 |
| 10.969200 | 284.5670 | 60073 | 54180.44 |
| 10.781300 | 283.1020 | 60075 | 54182.24 |
| 10.595600 | 281.6360 | 60077 | 54184.05 |
| 10.412200 | 280.1690 | 60079 | 54185.85 |
| 10.231100 | 278.7010 | 60081 | 54187.65 |
| 10.052100 | 277.2330 | 60083 | 54189.46 |
| 9.875460 | 275.7650 | 60085 | 54191.26 |
| 9.700970 | 274.2950 | 60087 | 54193.07 |
| 9.528680 | 272.8250 | 60089 | 54194.87 |
| 9.358550 | 271.3530 | 60091 | 54196.67 |
| 9.190570 | 269.8810 | 60093 | 54198.48 |
| 9.024730 | 268.4080 | 60095 | 54200.28 |
| 8.861000 | 266.9350 | 60097 | 54202.09 |
| 8.699390 | 265.4600 | 60099 | 54203.89 |
| 8.539850 | 263.9840 | 60101 | 54205.69 |
| 8.382390 | 262.5080 | 60103 | 54207.50 |
| 8.226980 | 261.0300 | 60105 | 54209.30 |
| 8.073610 | 259.5520 | 60107 | 54211.10 |
| 7.922250 | 258.0720 | 60109 | 54212.91 |
| 7.772900 | 256.5920 | 60111 | 54214.71 |
| 7.625540 | 255.1110 | 60113 | 54216.52 |
| 7.480160 | 253.6280 | 60115 | 54218.32 |
| 7.336720 | 252.1440 | 60117 | 54220.12 |
| 7.195230 | 250.6600 | 60119 | 54221.93 |
| 7.055660 | 249.1740 | 60121 | 54223.73 |
| 6.918000 | 247.6870 | 60123 | 54225.53 |
| 6.782230 | 246.1990 | 60125 | 54227.34 |
| 6.648330 | 244.7100 | 60127 | 54229.14 |
| 6.516300 | 243.2190 | 60129 | 54230.95 |
| 6.386110 | 241.7280 | 60131 | 54232.75 |
| 6.257750 | 240.2350 | 60133 | 54234.55 |
| 6.131200 | 238.7410 | 60135 | 54236.36 |

Table A.1 continued

| | | | |
|---|---|---|---|
| 6.006450 | 237.2450 | 60137 | 54238.16 |
| 5.883490 | 235.7480 | 60139 | 54239.97 |
| 5.762290 | 234.2500 | 60141 | 54241.77 |
| 5.642840 | 232.7510 | 60143 | 54243.57 |
| 5.525130 | 231.2500 | 60145 | 54245.38 |
| 5.409140 | 229.7480 | 60147 | 54247.18 |
| 5.294850 | 228.3400 | 60149 | 54248.98 |
| 5.182320 | 226.9270 | 60151 | 54250.79 |
| 5.071570 | 225.5020 | 60153 | 54252.59 |
| 4.962560 | 224.0660 | 60155 | 54254.40 |
| 4.855260 | 222.6180 | 60157 | 54256.20 |
| 4.749640 | 221.1590 | 60159 | 54258.00 |
| 4.645670 | 219.6900 | 60161 | 54259.81 |
| 4.543340 | 218.2120 | 60163 | 54261.61 |
| 4.442600 | 216.7260 | 60165 | 54263.42 |
| 4.343440 | 215.2320 | 60167 | 54265.22 |
| 4.245840 | 213.7320 | 60169 | 54267.02 |
| 4.149780 | 212.2270 | 60171 | 54268.83 |
| 4.055240 | 210.7180 | 60173 | 54270.63 |
| 3.962210 | 209.2040 | 60175 | 54272.43 |
| 3.870670 | 207.6870 | 60177 | 54274.24 |
| 3.780600 | 206.1660 | 60179 | 54276.04 |
| 3.691980 | 204.6430 | 60181 | 54277.85 |
| 3.604820 | 203.1180 | 60183 | 54279.65 |
| 3.519080 | 201.5900 | 60185 | 54281.45 |
| 3.434750 | 200.0590 | 60187 | 54283.26 |
| 3.351820 | 198.5260 | 60189 | 54285.06 |
| 3.270280 | 196.9910 | 60191 | 54286.86 |
| 3.190120 | 195.4540 | 60193 | 54288.67 |
| 3.111310 | 193.9140 | 60195 | 54290.47 |
| 3.033840 | 192.3710 | 60197 | 54292.28 |
| 2.957710 | 190.8260 | 60199 | 54294.08 |
| 2.882900 | 189.2790 | 60201 | 54295.88 |
| 2.809380 | 187.7300 | 60203 | 54297.69 |
| 2.737160 | 186.1770 | 60205 | 54299.49 |
| 2.666220 | 184.6220 | 60207 | 54301.30 |
| 2.596540 | 183.0650 | 60209 | 54303.10 |
| 2.528110 | 181.5050 | 60211 | 54304.90 |
| 2.460920 | 179.9420 | 60213 | 54306.71 |
| 2.394950 | 178.3760 | 60215 | 54308.51 |
| 2.330200 | 176.8070 | 60217 | 54310.31 |
| 2.266640 | 175.2350 | 60219 | 54312.12 |
| 2.204270 | 173.6610 | 60221 | 54313.92 |
| 2.143070 | 172.0830 | 60223 | 54315.73 |
| 2.083030 | 170.5020 | 60225 | 54317.53 |
| 2.024130 | 168.9170 | 60227 | 54319.33 |

Table A.1 continued

| | | | |
|---|---|---|---|
| 1.966370 | 167.3300 | 60229 | 54321.14 |
| 1.909740 | 165.7390 | 60231 | 54322.94 |
| 1.854210 | 164.1440 | 60233 | 54324.75 |
| 1.799770 | 162.5460 | 60235 | 54326.55 |
| 1.746420 | 160.9440 | 60237 | 54328.35 |
| 1.694140 | 159.3390 | 60239 | 54330.16 |
| 1.642920 | 157.7290 | 60241 | 54331.96 |
| 1.592750 | 156.2020 | 60243 | 54333.76 |
| 1.543650 | 154.6610 | 60245 | 54335.57 |
| 1.495620 | 153.1040 | 60247 | 54337.37 |
| 1.448620 | 151.5330 | 60249 | 54339.18 |
| 1.402650 | 149.9500 | 60251 | 54340.98 |
| 1.357680 | 148.3540 | 60253 | 54342.78 |
| 1.313690 | 146.7480 | 60255 | 54344.59 |
| 1.298480 | 146.1890 | 60257 | 54346.39 |
| 1.255800 | 144.8830 | 60259 | 54348.19 |
| 1.214160 | 143.3320 | 60261 | 54350.00 |
| 1.173470 | 141.8160 | 60263 | 54351.80 |
| 1.133720 | 140.3360 | 60265 | 54353.61 |
| 1.094930 | 138.7680 | 60267 | 54355.41 |
| 1.057040 | 137.1840 | 60269 | 54357.21 |
| 1.020050 | 135.6380 | 60271 | 54359.02 |
| 0.983947 | 134.0770 | 60273 | 54360.82 |
| 0.948721 | 132.4890 | 60275 | 54362.63 |
| 0.914352 | 130.9410 | 60277 | 54364.43 |
| 0.880839 | 129.3740 | 60279 | 54366.23 |
| 0.848167 | 127.7220 | 60281 | 54368.04 |
| 0.816302 | 126.1110 | 60283 | 54369.84 |
| 0.785246 | 124.5060 | 60285 | 54371.64 |
| 0.754988 | 122.8590 | 60287 | 54373.45 |
| 0.725509 | 121.2550 | 60289 | 54375.25 |
| 0.696808 | 119.6490 | 60291 | 54377.06 |
| 0.668874 | 118.0160 | 60293 | 54378.86 |
| 0.641692 | 116.4270 | 60295 | 54380.66 |
| 0.615260 | 114.8390 | 60297 | 54382.47 |
| 0.589568 | 113.2670 | 60299 | 54384.27 |
| 0.564609 | 111.7390 | 60301 | 54386.07 |
| 0.540382 | 110.1280 | 60303 | 54387.88 |
| 0.516856 | 108.5500 | 60305 | 54389.68 |
| 0.494030 | 107.0270 | 60307 | 54391.49 |
| 0.471902 | 105.5660 | 60309 | 54393.29 |
| 0.450475 | 104.1510 | 60311 | 54395.09 |
| 0.429743 | 102.7840 | 60313 | 54396.90 |
| 0.409705 | 101.4640 | 60315 | 54398.70 |
| 0.390353 | 100.1980 | 60317 | 54400.51 |
| 0.371684 | 98.9911 | 60319 | 54402.31 |

Table A.1 continued

| | | | |
|---|---|---|---|
| 0.353692 | 97.8333 | 60321 | 54404.11 |
| 0.336369 | 96.8006 | 60323 | 54405.92 |
| 0.319720 | 95.8080 | 60325 | 54407.72 |
| 0.303732 | 94.9458 | 60327 | 54409.52 |
| 0.288407 | 94.1437 | 60329 | 54411.33 |
| 0.273731 | 93.4296 | 60331 | 54413.13 |
| 0.259697 | 92.7886 | 60333 | 54414.94 |
| 0.246292 | 92.1669 | 60335 | 54416.74 |
| 0.233493 | 91.5579 | 60337 | 54418.54 |
| 0.221280 | 90.9616 | 60339 | 54420.35 |
| 0.209630 | 90.3394 | 60341 | 54422.15 |
| 0.198518 | 89.7254 | 60343 | 54423.96 |
| 0.187924 | 88.9443 | 60345 | 54425.76 |
| 0.177808 | 88.1984 | 60347 | 54427.56 |
| 0.168155 | 87.4997 | 60349 | 54429.37 |
| 0.158955 | 86.8337 | 60351 | 54431.17 |
| 0.150192 | 86.2705 | 60353 | 54432.97 |
| 0.141858 | 85.7388 | 60355 | 54434.78 |
| 0.133938 | 85.3192 | 60357 | 54436.58 |
| 0.126424 | 84.9278 | 60359 | 54438.39 |
| 0.119300 | 84.5149 | 60361 | 54440.19 |
| 0.112544 | 84.1201 | 60363 | 54441.99 |
| 0.106142 | 83.7524 | 60365 | 54443.80 |
| 0.100077 | 83.4044 | 60367 | 54445.60 |
| 0.094336 | 83.0874 | 60369 | 54447.40 |
| 0.088904 | 82.7907 | 60371 | 54449.21 |
| 0.083766 | 82.5788 | 60373 | 54451.01 |
| 0.078913 | 82.3905 | 60375 | 54452.82 |
| 0.074331 | 82.3063 | 60377 | 54454.62 |
| 0.070012 | 82.2270 | 60379 | 54456.42 |
| 0.065939 | 82.1522 | 60381 | 54458.23 |
| 0.063100 | 82.1000 | 60383 | 54460.03 |

## APPENDIX B

### B.1 ATTENUATION PROFILES FOR ORBITS 51 AND 54

The tables B.1 to B.4 are the results for orbits 51 and 54. Shown are the loss of signal point ($\leq$ 3 dB) as well as the 3 dB and 6 dB cutoffs at the three experimental frequencies. Figures B.1 to B.12 are the plots of attenuation for these orbits and the excess Doppler shifts are shown in Figures B.13 to B.15.

Table B.1: Revolution 51 ingress

| | **S** | **X** | **Ka** |
|---|---|---|---|
| SNR $\leq$ 3 dB | 1.40 bars | 1.09 bars | 0.82 bar |
| SNR > 3 dB | 1.36 bars | 1.06 bars | 0.79 bar |
| SNR > 6 dB | 1.36 bars | 1.02 bars | 0.79 bar |

Table B.2: Revolution 51 egress

| | **S** | **X** | **Ka** |
|---|---|---|---|
| SNR $\leq$ 3 dB | 1.40 bars | 1.09 bars | 0.82 bar |
| SNR > 3 dB | 1.36 bars | 1.06 bars | 0.79 bar |
| SNR > 6 dB | 1.36 bars | 1.06 bars | 0.79 bar |

Table B.3: Revolution 54 ingress

| | **S** | **X** | **Ka** |
|---|---|---|---|
| SNR $\leq$ 3 dB | 1.40 bars | 1.09 bars | 0.82 bar |
| SNR > 3 dB | 1.36 bars | 1.06 bars | 0.79 bar |
| SNR > 6 dB | 1.36 bars | 1.02 bars | 0.79 bar |

Table B.4: Revolution 54 egress

| | **S** | **X** | **Ka** |
|---|---|---|---|
| SNR $\leq$ 3 dB | 1.40 bars | 1.09 bars | 0.82 bar |
| SNR > 3 dB | 1.36 bars | 1.06 bars | 0.79 bar |
| SNR > 6 dB | 1.31 bars | 1.02 bars | 0.79 bar |

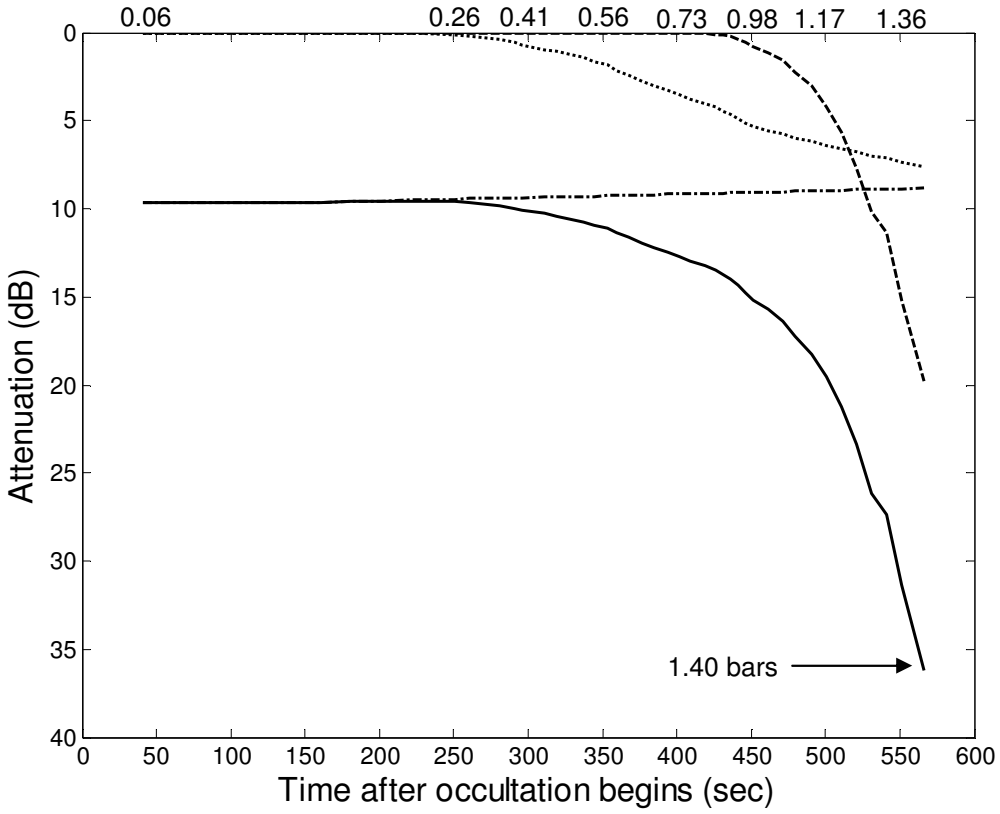


Figure B.1: Revolution 51, ingress at S-band. S-band free space SNR is 39 dB and loss of signal occurs at a pressure of 1.40 bars. The dashed line is the absorption due to ammonia, the dotted line is the absorption due to phosphine, the dotted dashed line is refractive defocusing and the solid line is the aggregate. The pressure is indicated at various points in time at the top of the graph but is not to scale.

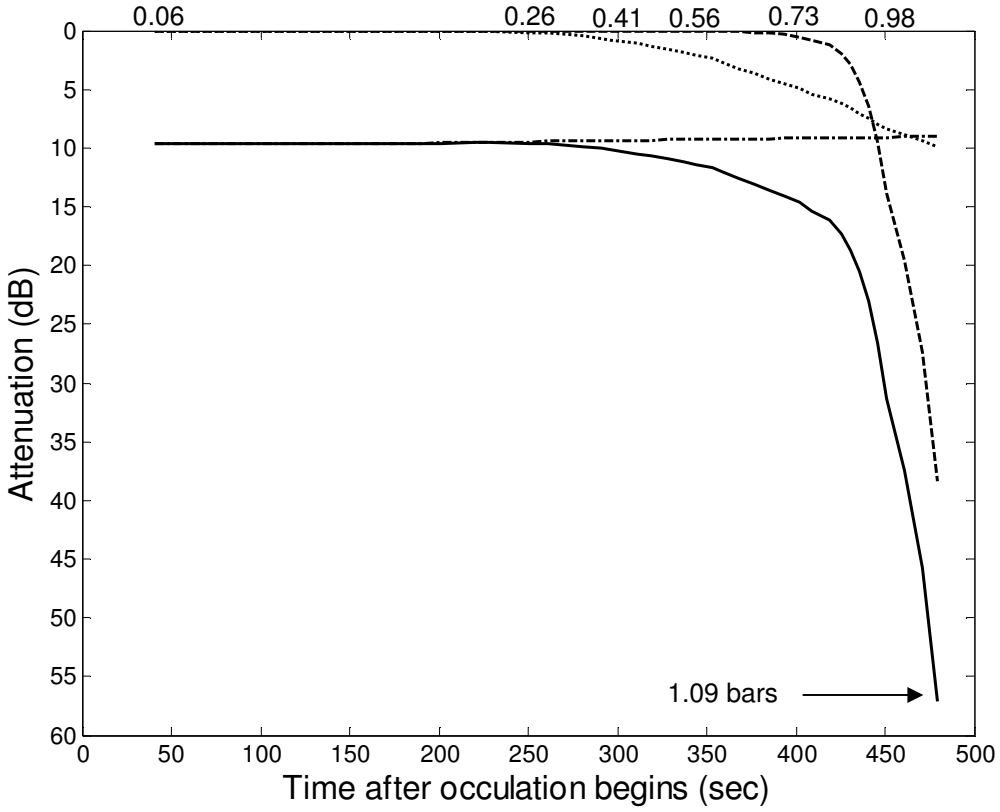


Figure B.2: Revolution 51, ingress at X-band. X-band free space SNR is 51 dB and loss of signal occurs at a pressure of 1.09 bars. The dashed line is the absorption due to ammonia, the dotted line is the absorption due to phosphine, the dotted dashed line is refractive defocusing and the solid line is the aggregate. The pressure is indicated at various points in time at the top of the graph but is not to scale.

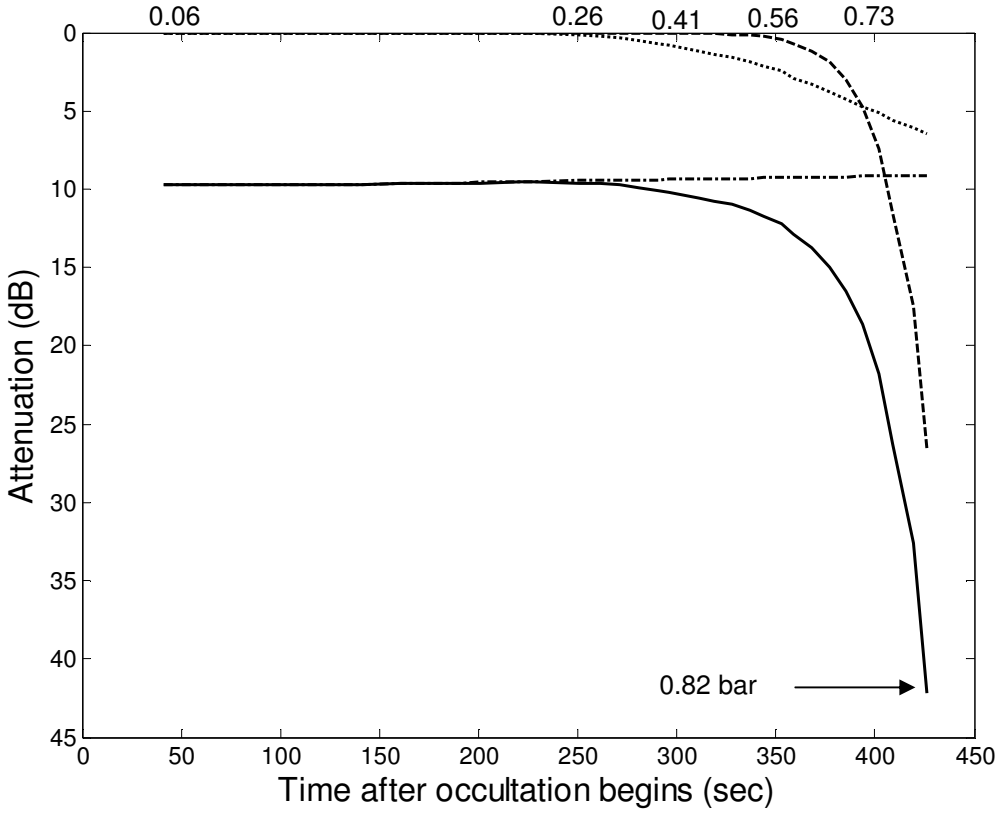


Figure B.3: Revolution 51, ingress at Ka-band. Ka-band free space SNR is 41 dB and loss of signal occurs at a pressure of 0.82 bar. The dashed line is the absorption due to ammonia, the dotted line is the absorption due to phosphine, the dotted dashed line is refractive defocusing and the solid line is the aggregate. The pressure is indicated at various points in time at the top of the graph but is not to scale.

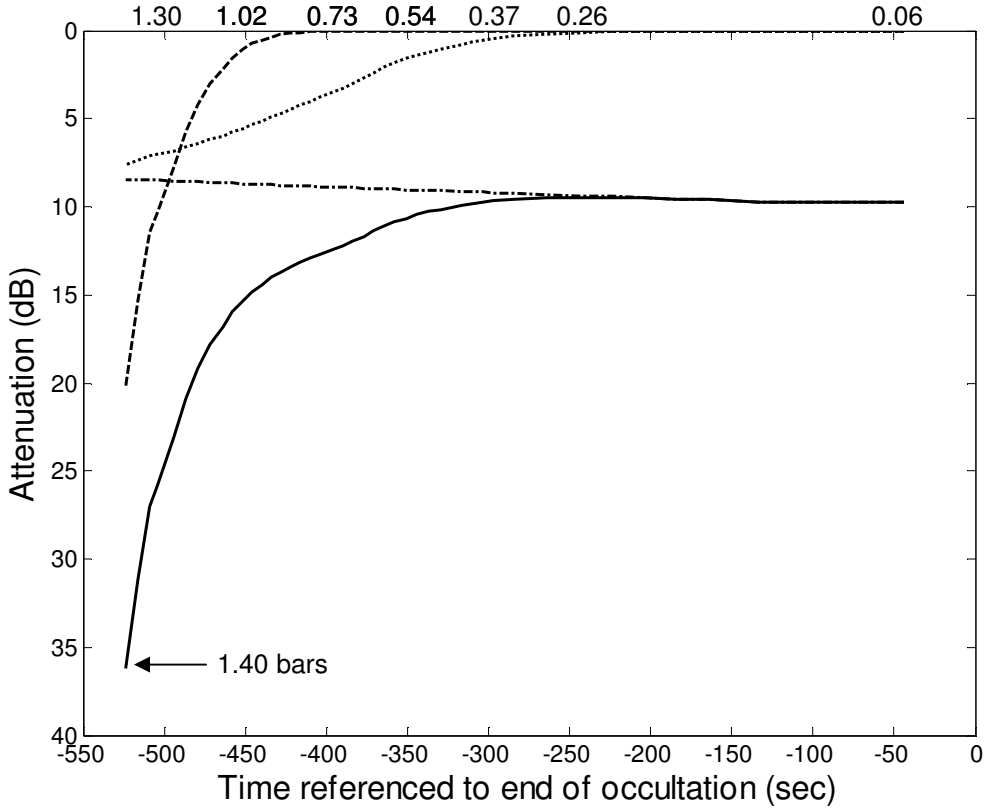


Figure B.4: Revolution 51, egress at S-band. S-band free space SNR is 39 dB and loss of signal occurs at a pressure of 1.40 bars. The dashed line is the absorption due to ammonia, the dotted line is the absorption due to phosphine, the dotted dashed line is refractive defocusing and the solid line is the aggregate. The pressure is indicated at various points in time at the top of the graph but is not to scale.

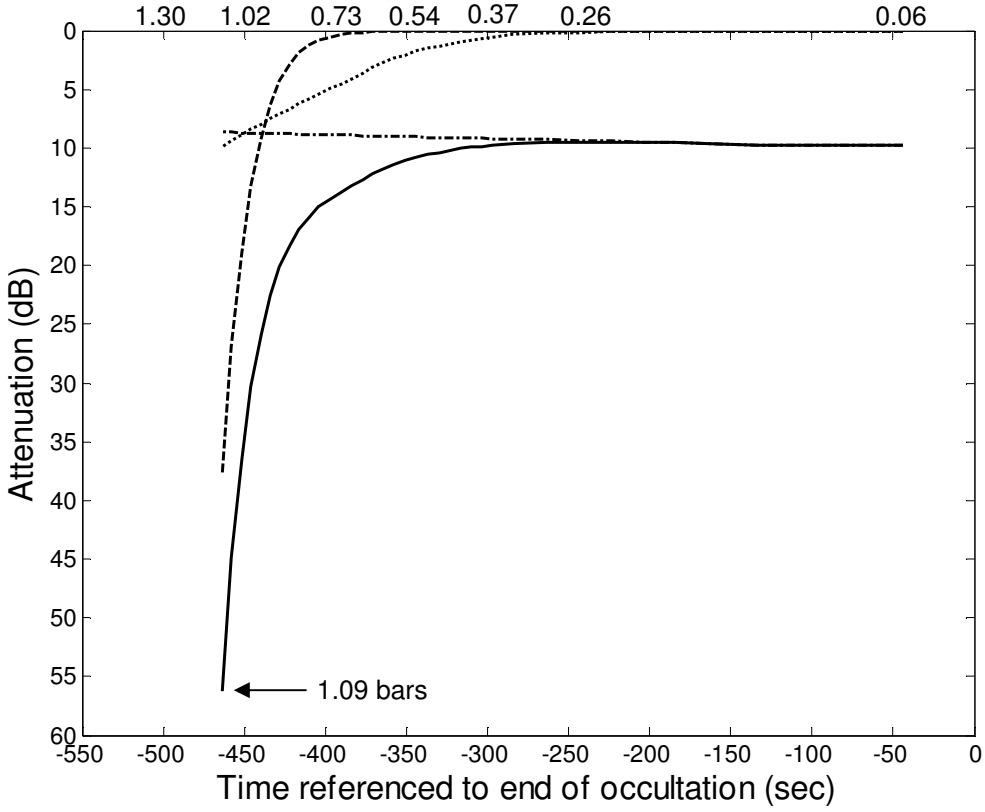


Figure B.5: Revolution 51, egress at X-band. X-band free space SNR is 51 dB and loss of signal occurs at a pressure of 1.09 bars. The dashed line is the absorption due to ammonia, the dotted line is the absorption due to phosphine, the dotted dashed line is refractive defocusing and the solid line is the aggregate. The pressure is indicated at various points in time at the top of the graph but is not to scale.

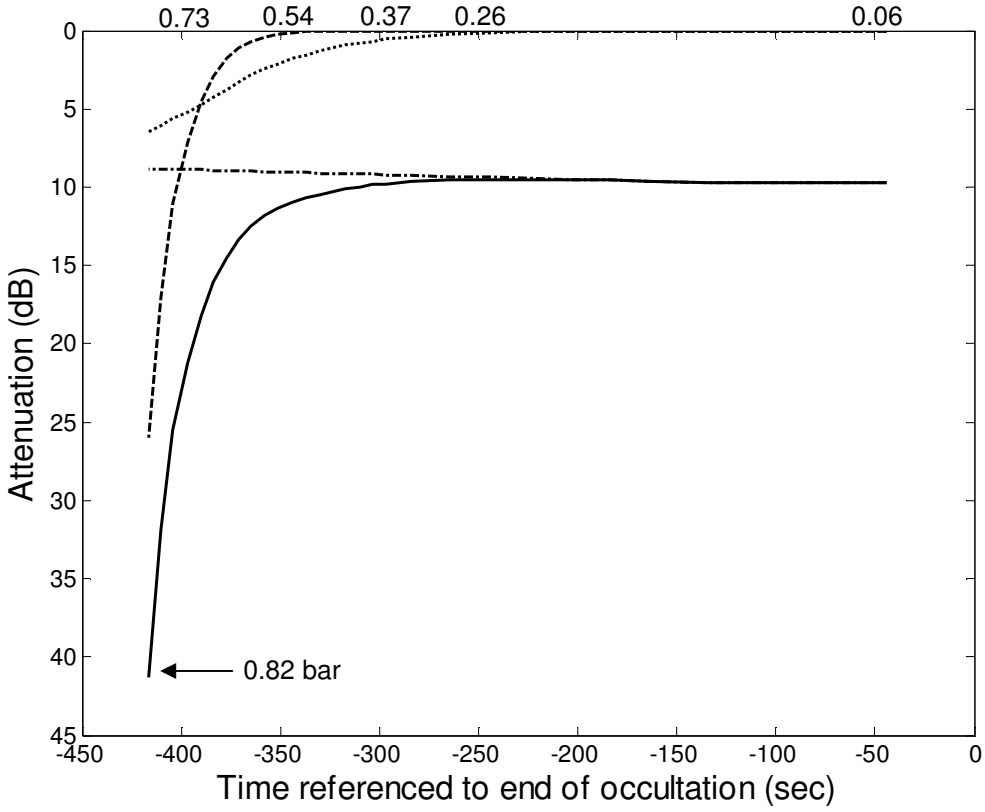


Figure B.6: Revolution 51, egress at Ka-band. Ka-band free space SNR is 41 dB and loss of signal occurs at a pressure of 0.82 bar. The dashed line is the absorption due to ammonia, the dotted line is the absorption due to phosphine, the dotted dashed line is refractive defocusing and the solid line is the aggregate. The pressure is indicated at various points in time at the top of the graph but is not to scale.

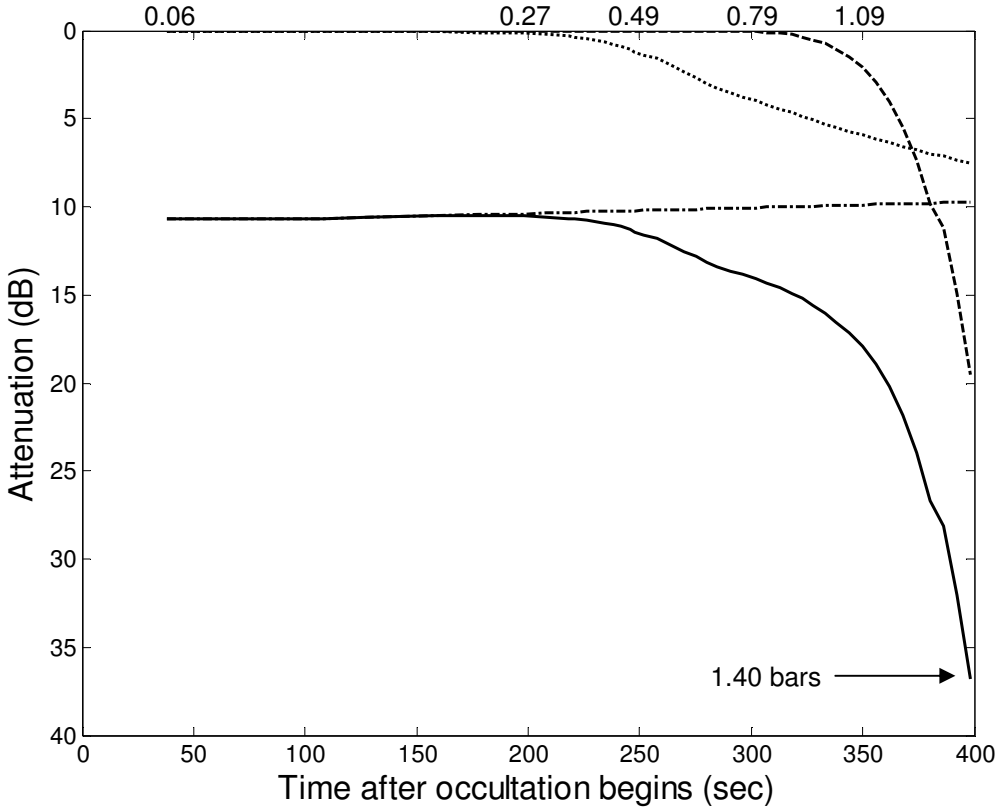


Figure B.7: Revolution 54, ingress at S-band. S-band free space SNR is 39 dB and loss of signal occurs at a pressure of 1.40 bars. The dashed line is the absorption due to ammonia, the dotted line is the absorption due to phosphine, the dotted dashed line is refractive defocusing and the solid line is the aggregate. The pressure is indicated at various points in time at the top of the graph but is not to scale.

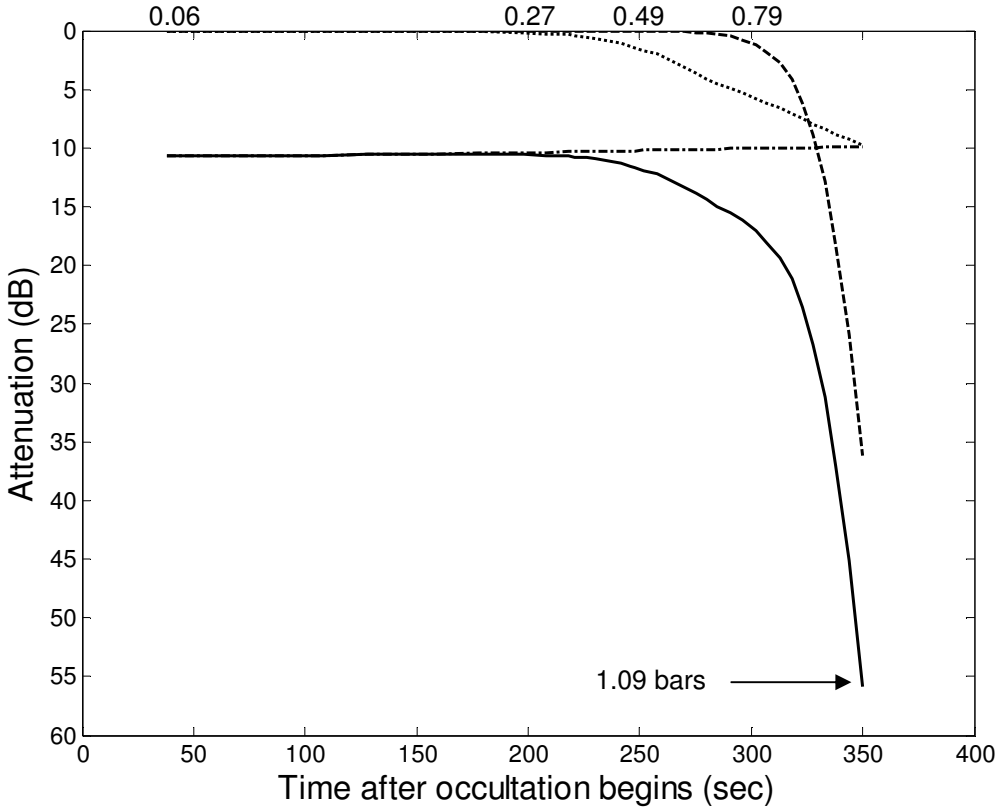


Figure B.8: Revolution 54, ingress at X-band. X-band free space SNR is 51 dB and loss of signal occurs at a pressure of 1.09 bars. The dashed line is the absorption due to ammonia, the dotted line is the absorption due to phosphine, the dotted dashed line is refractive defocusing and the solid line is the aggregate. The pressure is indicated at various points in time at the top of the graph but is not to scale.

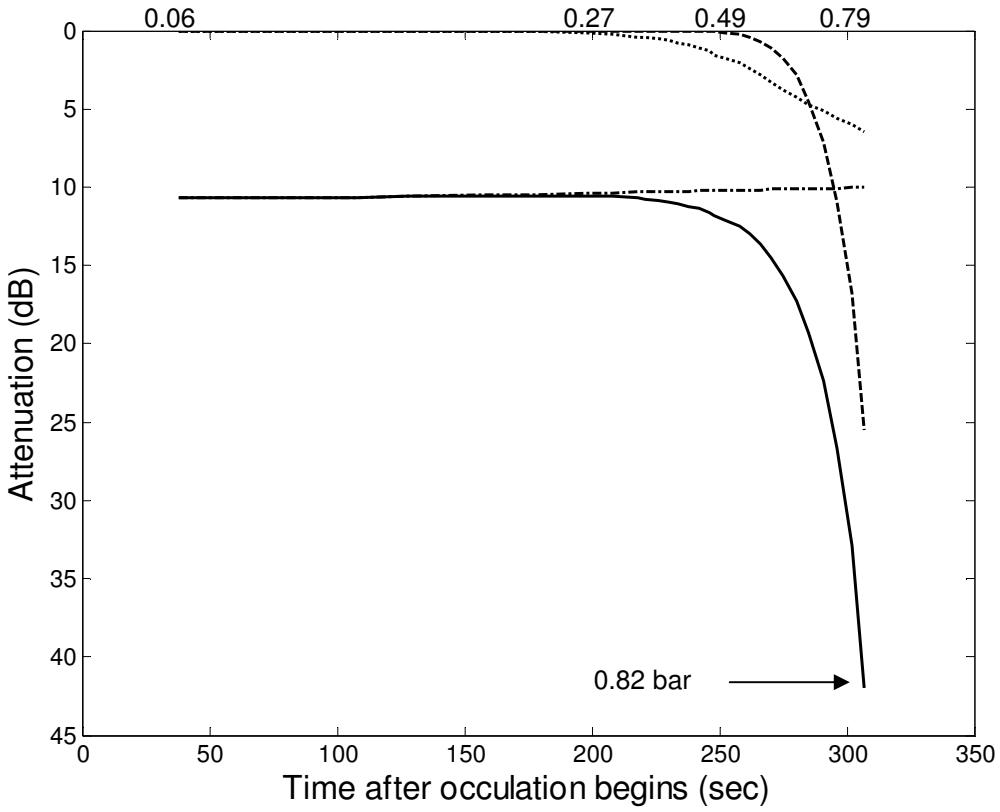


Figure B.9: Revolution 54, ingress at Ka-band. Ka-band free space SNR is 41 dB and loss of signal occurs at a pressure of 0.82 bar. The dashed line is the absorption due to ammonia, the dotted line is the absorption due to phosphine, the dotted dashed line is refractive defocusing and the solid line is the aggregate. The pressure is indicated at various points in time at the top of the graph but is not to scale.

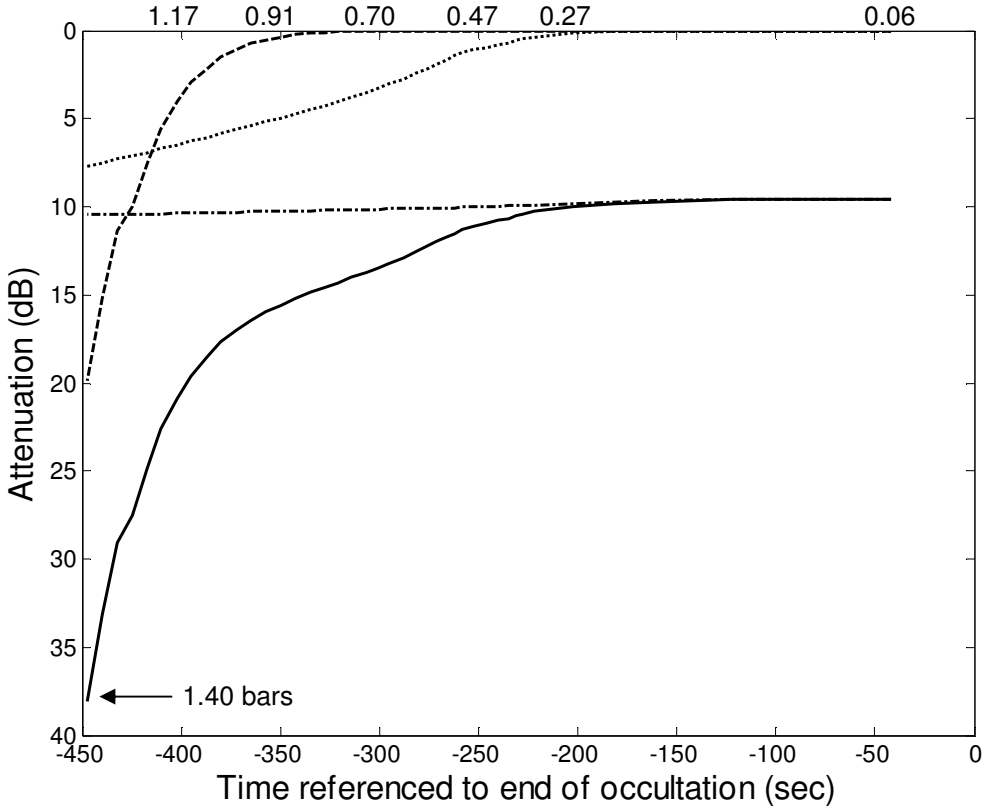


Figure B.10: Revolution 54, egress at S-band. S-band free space SNR is 39 dB and loss of signal occurs at a pressure of 1.40 bars. The dashed line is the absorption due to ammonia, the dotted line is the absorption due to phosphine, the dotted dashed line is refractive defocusing and the solid line is the aggregate. The pressure is indicated at various points in time at the top of the graph but is not to scale.

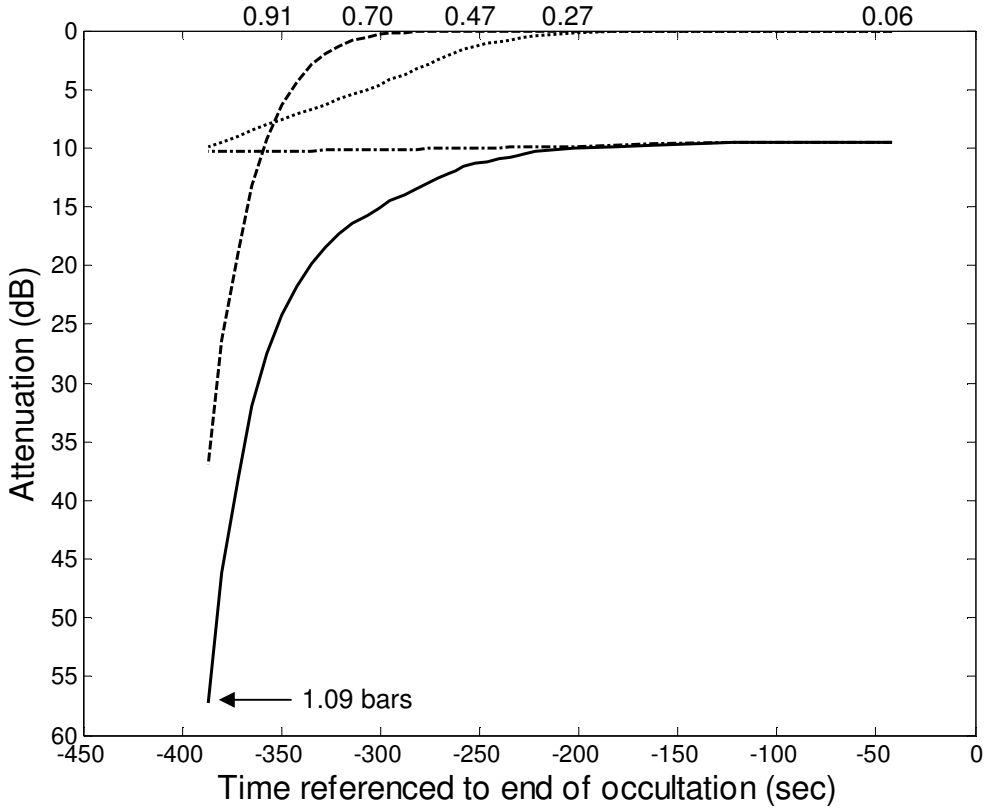


Figure B.11: Revolution 54, egress at X-band. X-band free space SNR is 51 dB and loss of signal occurs at a pressure of 1.09 bars. The dashed line is the absorption due to ammonia, the dotted line is the absorption due to phosphine, the dotted dashed line is refractive defocusing and the solid line is the aggregate. The pressure is indicated at various points in time at the top of the graph but is not to scale.

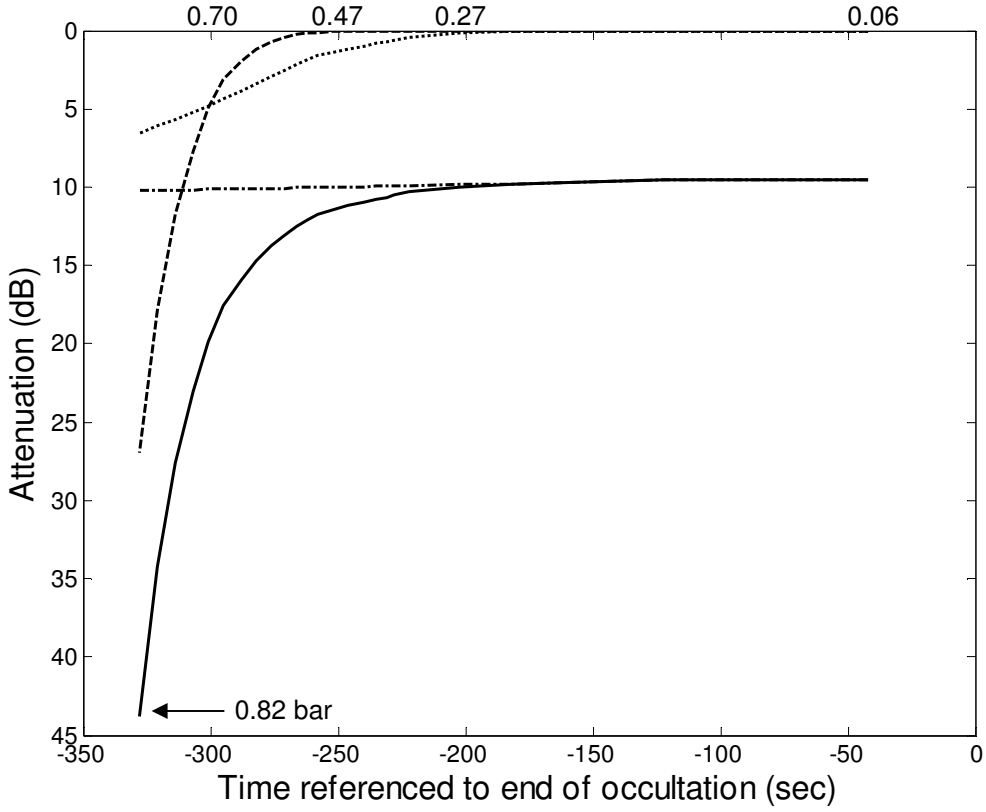


Figure B.12: Revolution 54, egress at Ka-band. Ka-band free space SNR is 41 dB and loss of signal occurs at a pressure of 0.82 bar. The dashed line is the absorption due to ammonia, the dotted line is the absorption due to phosphine, the dotted dashed line is refractive defocusing and the solid line is the aggregate. The pressure is indicated at various points in time at the top of the graph but is not to scale.

## B.2 EXCESS DOPPLER SHIFTS FOR ORBITS 51 AND 54

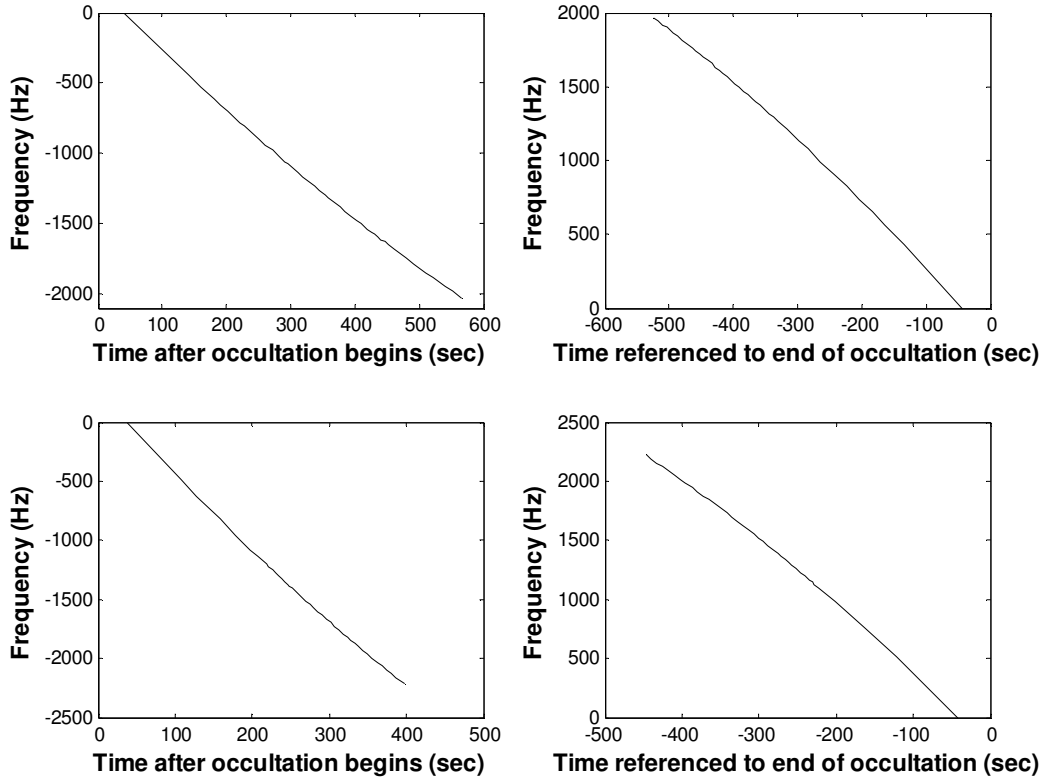


Figure B.13: Predicted excess Doppler shifts of the S-band carrier signal from Cassini as measured at Earth. The top two graphs are for Revolution 51 with the left being ingress and the right egress. The bottom two graphs are for Revolution 54, the left ingress, the right egress.

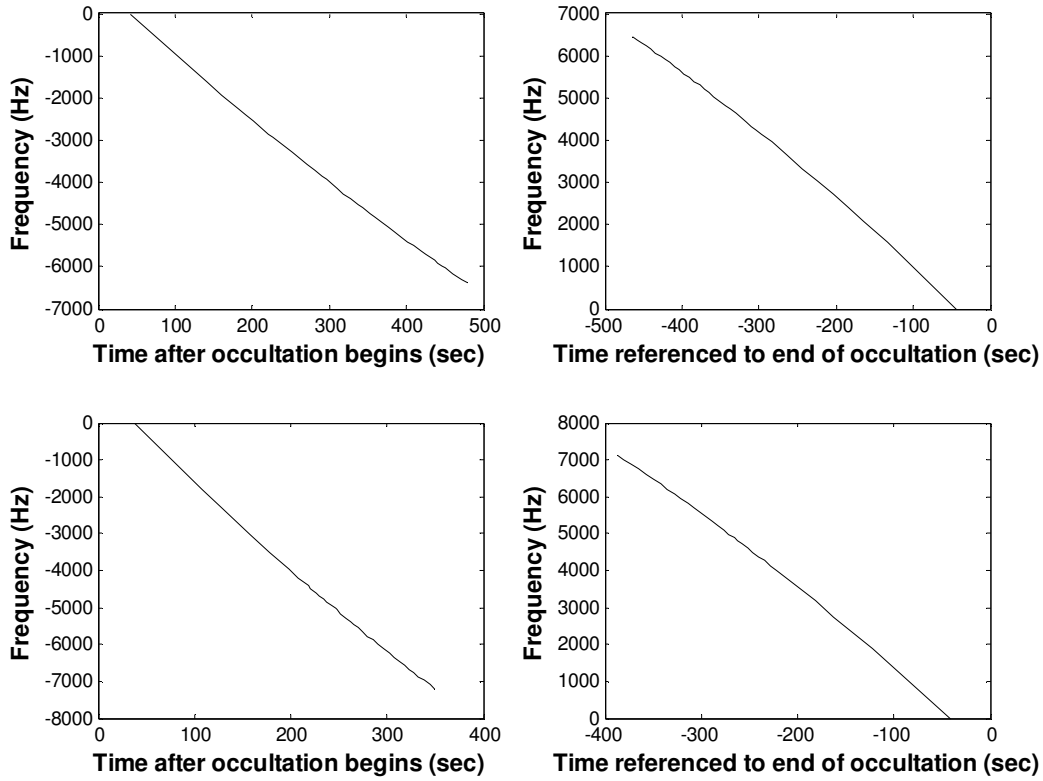


Figure B.14: Predicted excess Doppler shifts of the X-band carrier signal from Cassini as measured at Earth. The top two graphs are for Revolution 51 with the left being ingress and the right egress. The bottom two graphs are for Revolution 54, the left ingress, the right egress.

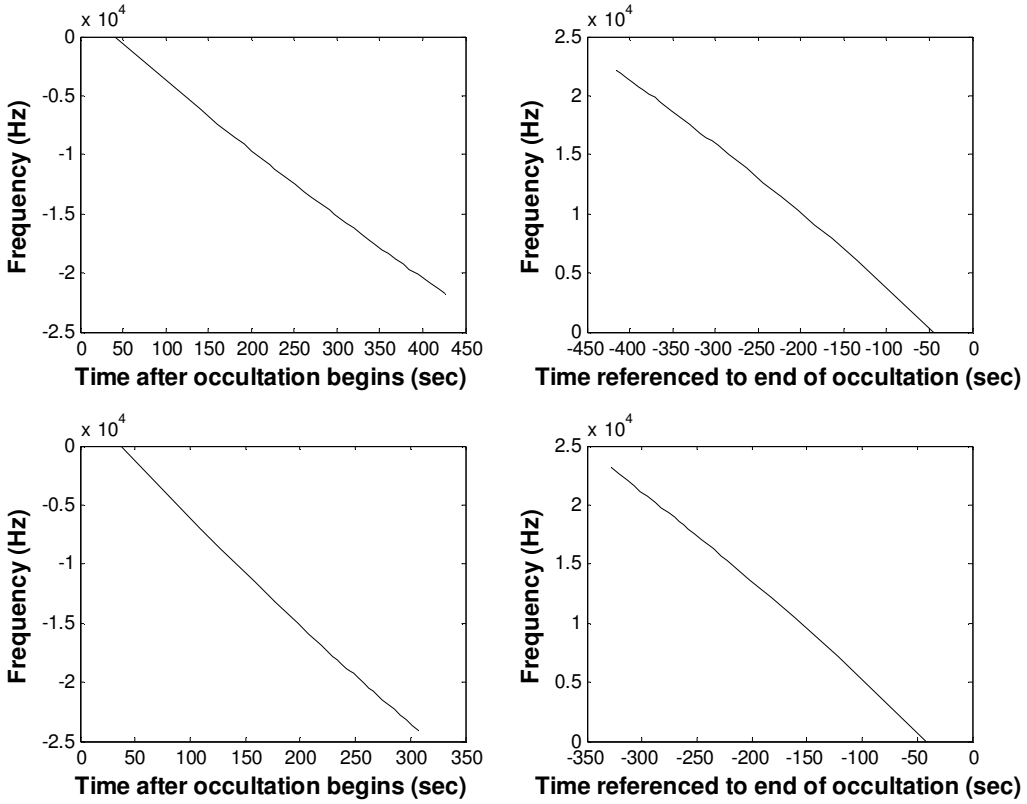


Figure B.15: Predicted excess Doppler shifts of the Ka-band carrier signal from Cassini as measured at Earth. The top two graphs are for Revolution 51 with the left being ingress and the right egress. The bottom two graphs are for Revolution 54, the left ingress, the right egress.

## REFERENCES


Ahmad B. and G. L. Tyler (1999). Systematic Errors in Atmospheric Profiles Obtained from Abelian Inversion of Radio Occultation Data: Effects of Large-Scale Horizontal Gradients. J. Geophys. Res., 104, NO. D4, 3971-3992.

Anders, E. and N. Grevesse (1989). Abundances of the Elements: Meteoritic and Solar. Geochim. Cosmochim. Acta, 54, 197-214.

Atreya, S. K., M. H. Wong, T.C. Owen, P. R. Mahaffy, H. B. Niemann, I. de Pater, P. Drossart, Th Encrenaz (1999). A Comparison of the Atmospheres of Jupiter and Saturn: Deep Atmospheric Composition, Cloud Structure, Vertical Mixing and Origin. Planetary and Space Science, 47, 1243-1262.

Ben-Reuven, A. (1966). Impact Broadening of Microwave Spectra. Phys. Rev., 145, 7-22.

Berge, G. L., and S. Gulkis (1976). Earth-Based Radio Observations of Jupiter: Millimeter to Meter Wavelengths. University of Arizona Press, Tucson.

Briggs, F. H. and P. D. Sackett (1989). Radio Observations of Saturn as a Probe of its Atmosphere and Cloud Structure. Icarus 80, 77-103.

Brown, L.R., and D. B. Peterson (1994). An Empirical Expression for Linewidths of Ammonia from Far-Infrared Measurements. J. Mol. Spectrosc., 168, 596-606.

Courtin, R., D. Gautier, A. Martein, B. Bezard and R. Hanel (1984). The Composition of Saturn's Atmosphere at Northen Temperate Latitudes from Voyager IRIS Spectra: $NH_3$, $PH_3$, $C_2H_2$, $C_2H_6$, $CH_3D$, $CH_4$, and the Saturnian D/H Ratio. Astron. J., 287, 899-916.

Culshaw, W. (1960). High Resolution Millimeter Wave Fabry-Perot Interferometer. IRE Trans. on Microwave Theory and Techniques, vol. MTT-8, no. 2, 182-189.

Culshaw, W. (1962). Futher Considerations on Fabry-Perot Type Resonators. IRE Trans. on Microwave Theory and Techniques, vol. MTT-10, no. 5, 331-339.

Debye, P. (1929). Polar Molecules. The Chemical Catalog Company, Inc., New York.

DeBoer, D. R. and P. G. Steffes (1994). Laboratory Measurements of the Microwave Properties of $H_2S$ under Simulated Jovian Conditions with an Application to Neptune. Icarus, 109, 352-366.

DeBoer, D. R. and P. G. Steffes (1996). The Georgia Tech high sensitivity microwave measurement system. Astrophysics and Space Science, 236, 111-124.

de Pater I., D. DeBoer, M. Marley, R. Freedman, R. Young (2005). Retrieval of Water in Jupiter's Deep Atmosphere Using Microwave Spectra of its Brightness Temperature. Icarus, 173, 425–438.

de Pater, I and S. T. Massie (1985). Models of the millimeter-centimeter spectra of the giant planets. Icarus, 62, 143-171.

de Pater, I. and D. L. Mitchell (1993). Radio observations of the planets: the importance of laboratory measurements. Journal of Geophysical Research, 98, 5471-5490.

Eshleman, V. R., D. O. Muhleman, P. D. Nicholson and P. G. Steffes (1980). Comment on Absorbing Regions in the Atmosphere of Venus as Measured by Radio Occultations. Icarus, 44, 793-803.

Essen, L. (1953). The Refractive Indices of Water Vapour, Air, Oxygen, Nitrogen, Hydrogen, Deuterium and Helium. Proc. Phys. Soc. (London), B66, 189-193.

Fahd, A. K., and P. G. Steffes (1992). Laboratory Measurements of the Microwave and Millimeter-Wave Opacity of Gaseous Sulfur Dioxide ($SO_2$) Under Simulated Conditions for the Venus Atmosphere. Icarus, 97, 200-210.

Fjeldbo, G. (1973). Radio Occultation Experiments Planned for Pioneer and Mariner Missions to the Outer Planets. Planet. Space Sci., 21, 1533-1547.

Fjeldbo, G. and V. R. Eshleman (1965). The Bistatic Radar-Occultation Method for the Study of Planetary Atmospheres. J. Geo. Res., 70, 3217-3225.

Fjeldbo, G., A. J. Kliore and V. R. Eshleman (1971). The Neutral Atmosphere of Venus as Studied with the Mariner V Radio Occultation Experiments. Astron. J. 76, 123-140.

Griffin, M. J., P. A. R. Ade, G. S. Orton, E. I. Robson, W. K. Gear, I. G. Nolt, and J. V. Radostitz (1986). Submillimeter and Millimeter Observations of Jupiter. Icarus, 65, 244-256.

Griffin, M. J., and G. S. Orton (1993). The near-millimeter brightness temperature spectra of Uranus and Neptune. Icarus, 105, 537-547.

Gross, E. P., Shape of collision broadened spectral lines (1955). Phys. Rev., 97, 395-403.

Haines, E. (1989). An Introduction to Ray Tracing, chap. Essential Ray Tracing Algorithms. Academic Press, 35-39.

Hartman N. F., D. P. Campbell, J. L. Walsh and U. Akki (1995). Integrated Optic Gaseous $NH_3$ Sensor for Agricultural Applications. SPIE Proceedings, 2345, 314-323.

Heckbert, P. S. (1989). An Introduction to Ray Tracing, chap. Writing a Ray Tracer. Academic Press, 290-293.

Hewlett-Packard (1997). HP 8660 E-Series Spectrum Analyzer Calibration Guide. Hewlett Packard Company.

Hoffman, J. P., P. G. Steffes, D. R. DeBoer (2001). Laboratory Measurements of the Microwave Opacity of Phosphine: Opacity Formalism and Application to the Atmospheres of the Outer Planets. Icarus, 152, 172-184.

Hoffman, J. P. (2001). Microwave Opacity of Phosphine: Application to Remote Sensing of the Atmospheres of the Outer Planets. Ph.D. Thesis, The Georgia Institute of Technology.

Irwin, P. G. J, N. A. Teanby, S. B. Calcutt, F. W. Taylor, P. L. R. Read (2004). Vertical Profiles of Ammonia and Phosphine on Saturn Derived from Cassini/CIRS Far-Infrared Observations. B. A. A. S., 36, 1133.

Janssen, M.A., M.D. Hofstadter, S. Gulkis, A.P. Ingersoll, M. Allison, S.J. Bolton, S.M. Levin, L.W. Kamp (2005). Microwave Remote Sensing of Jupiter's Atmosphere from an Orbiting Spacecraft. Icarus, 173, 447–453.

Jenkins, J. M., P. G. Steffes, D. P. Hinson, J. D. Twicken and G. L. Tyler (1994). Radio Occultation Studies of the Venus Atmosphere with the Magellan Spacecraft, 2. Results from the October 1991 Experiments. Icarus, 110, 79-94.

Joiner, J., P. G. Steffes and J. M. Jenkins (1989). Laboratory Measurements of the 7.5-9.38 mm Absorption of Gaseous Ammonia ($NH_3$) Under Simulated Jovian Conditions. Icarus, 81, 386-395.

Joiner, J. and P. G. Steffes (1991). Modeling of Jupiter's Millimeter Wave Emission Utilizing Laboratory Measurements of Ammonia Opacity. J. Geo. Res., 96, 17463-17470.

Joiner, J. (1991). Millimeter-wave Spectra of the Jovian Planets. Ph.D. Thesis, Georgia Institute of Technology.

Kliore, A. J. and Woiceshyn, P. M. (1976). Structure of the Atmosphere of Jupiter from Pioneer 10 and 11 Radio Occultation Measurements, in Jupiter: Studies of the Interior Atmosphere, Magnetosphere and Satellites, ed. T. Gehrels, pp. 216-237. University of Arizona Press.

Kolodner, M. A. and P. G. Steffes (1998). The Microwave Absorption and Abundance of Sulfuric Acid Vapor in the Venus Atmosphere Based on New Laboratory Measurements. Icarus, 132, 151-169.

Kroto, H. W. (1992). Molecular Rotation Spectra. Dover Publications, New York.

Lindal, G. F., Sweetnam, D. N., Eshleman, V. R. (1985). The Atmosphere of Saturn: An Analysis of the Voyager Radio Occultation Measurements. The Astronomical Journal, 90, 1136-1146.

Matthaei, G. L., L. Young and E. Jones (1980). Microwave Filters, Impedance Matching Networks and Coupling Structures. McGraw-Hill.

Mohammed P. N., and P. G. Steffes (2003). Laboratory Measurements of the Ka-band (7.5 to 9.2 mm) Opacity of Phosphine ($PH_3$) and Ammonia ($NH_3$) Under Simulated Conditions for the Cassini-Saturn Encounter. Icarus, 158, 425-435.

Muhleman, D. O., and G. L. Berge (1991). Observations of Mars, Uranus, Neptune, Io, Europa, Ganymede and Callisto at a Wavelength of 2.66 mm. Icarus, 92, 263-272.

Noll, K. S. and H. P. Larson (1990). The Spectrum of Saturn from 1990 to 2230 $cm^{-1}$: Abundances of $AsH_3$, $CH_3D$, CO, $GeH_4$, $NH_3$ and $PH_3$. Icarus, 89, 168-189.

Orton, G. S., M. J. Griffin, P. A. R. Ade, I. G. Nolt, J. V. Radostitz, E. I. Robson, and W. K. Gear (1986). Submillimeter and Millimeter Observations of Uranus and Neptune. Icarus, 67, 289-304.

Orton, G. S., E. Serabyn, Y.T. Lee (2000). Vertical Distribution of $PH_3$ in Saturn from Observations of its 1-0 and 3-2 Rotational Lines. Icarus, 146, 48-59.

Orton, G. S., E. Serabyn, Y.T. Lee (2001). Corrigendum. Icarus, 149, 489-490.

Papoulis, A. (1991). Probability, Random Variables and Stochastic Processes, 3rd ed. McGraw-Hill, New York.

Pickett, H. M., R. L. Poynter, and E. A. Cohen (1981). Pressure Broadening of Phosphine by Hydrogen and Helium. J. Quant. Spectrosc. Radiat. Transfer, 26, 197-198.

Pickett, H. M., R. L. Poynter, E. A. Cohen, M. L. Delitsky, J. C. Pearson, and H. S. P. Muller (1998). Submillimeter, Millimeter, and Microwave Spectral Line Catalog. J. Quant. Spectrosc. & Rad. Transfer, 60**,** 883-890.

Pine, A. S., V. N. Markov, G. Buffa, and O. Tarrini (1993). $N_2$, $O_2$, $H_2$, Ar and He Broadening in the ν1 Band of $NH_3$, J. Quant. Spectrosc. & Rad. Transfer, 50, 337-348.

Poynter, R. L. and R. K. Kakar (1975). The Microwave Frequencies, Line Parameters and Spectral Constants for $NH_3$. Astrophys. J. Suppl., 29, 87-96.

Pozar, D. M. (1998). Microwave Engineering. John Wiley and Sons Inc.

Prinn, R. G. and J. S. Lewis (1975). Phosphine on Jupiter and Implications for the Great Red Spot. Science, 190, 274-276.

Ramo, S., J. R. Whinnery and T. V. Duzer (1994). Fields and Waves in Communications Electronics. Wiley and Sons, New York.

Spilker, T. R. (1990). Laboratory Measurements of the Microwave Absorptivity and Refractivity Spectra of Gas Mixtures Applicable to Giant Planet Atmospheres. PhD Thesis, Stanford University.

Steffes, P. G., J. M. Jenkins, E. H. Seale and G. L. Tyler (1994). Radio Occultation Studies of the Venus Atmosphere with the Magellan Spacecraft, 1. Experimental Description and Performance. Icarus, 110, 71-78.

Steffes, P. G. and P. N. Mohammed (2002). Study of the Cassini Radio Occultation Sensitivity to Atmospheric Constituents Based on New Laboratory Measurements. Bull. Amer. Astron. Soc., 34, 910.

Townes, C. H., and A. L. Schawlow (1955). Microwave Spectroscopy. Dover Publications Inc.

Trafton, L. M. (1966). The Pressure Induced Monochromatic Translational Absorption Coefficients for Homopolar and Nonpolar Gases and Gas Mixtures with Particular Application to $H_2$. Astrophys. J., 146, 558-571.

Trafton, L. M. (1973). On the He-$H_2$ Thermal Opacity in Planetary Atmospheres. Astrophys. J., 179, 971-976.

Tyler, G. L. and H. T. Howard (1969). Refractivity of Carbon Dioxide Under Simulated Martian Conditions. Radio Science, 4, 899-904.

Valkenburg, E. P. and V. E. Derr (1966). A high-Q fabry-perot Interferometer for Water Vapor Absorption Measurements in the 100 Gc/s to 300 Gc/s Frequency Range. Proceedings of the IEEE, 54, 493-498.

Van der Tak, F., I. De Pater, A Silva and R. Millan (1999). Time Variability in the Radio Brightness Distribution of Saturn. Icarus, 142, 125-147.

Van Vleck, J. H., and V. F. Weisskopf (1945). On the Shape of Collision-Broadened Lines. Revs. Modern Phys., 17, 227-236.

Varanasi, P., Z. Li, and V. Nemtchinov (1994). Laboratory Data on the IR Lines of $^{12}CH_4$, $^{13}CH_4$, $^{12}CH_3D$, $^{12}CH_2$, $^{12}C^{13}CH_2$ Observable in the Jovian Atmosphere, B. A. A. S., 26, 1108.

Watson, H. E. and K. L. Ramaswamy (1936). The Rrefractive Index Dispersion and Polarization of Gases. Proceedings of the Royal Society of London. Series A, Mathematical and Physical Sciences, 156, no. 887, 144-157.

Weisstein, E. W. and E. Serabyn (1994). Detection of the 267 GHz $J$ = 1-0 Rotational Transition of $PH_3$ in Saturn with a New Fourier Transform Spectrometer. Icarus, 109, 367-381.

Wrixon, G. T, W. J. Welch and D. D. Thornton (1971). The Spectrum of Jupiter at Millimeter Wavelengths. Astrophys. J., 169, 171-183.

## VITA

Priscilla Naseem Mohammed was born on March 2, 1977 in San Fernando, Trinidad and Tobago. After attending high school at St. Joseph's Convent San Fernando and Presentation College San Fernando, then working at the Caroni (1975 Limited) Sugar Cane Laboratory as a chemical analyst, she left sweet T&T in 1996 to attend university at the Florida Institute of Technology. There, she was inducted into Tau Beta Pi and also interned at Siemens-Stromberg Carlson and Lucent Technologies. She graduated with high honor in December of 1999 with a Degree in Electrical Engineering, and then obtained a Master's Degree in Electrical Engineering in 2001 followed by a doctorate in 2005 both from the Georgia Institute of Technology.

As a Ph.D. student, Priscilla Mohammed performed microwave measurements of gaseous phosphine and ammonia under simulated conditions for the outer planets and used these measurements to develop a radio occultation simulator to predict absorption and excess Doppler due to Saturn's atmosphere. Much of this work was in support of the Cassini mission to Saturn. Based on the laboratory results published in Icarus (Mohammed and Steffes, 2003) the Cassini Project Science Group made the decision to extend the Ka-band (32 GHz) operation throughout the mission tour.